UNIVERSITY OF CALIFORNIA,
IRVINE

# Influence of Stress-Strain Fields on the Behavior of Deformation Twins in Mg

DISSERTATION

submitted in partial satisfaction of the requirements
for the degree of

DOCTOR OF PHILOSOPHY

in Materials Science and Engineering

by

Kehang Yu

Dissertation Committee:
Distinguished Professor Enrique J. Lavernia, Chair
Professor Julie M. Schoenung
Assistant Professor Penghui Cao

2022

## TABLE OF CONTENTS

## LIST OF FIGURES

Page

## LIST OF TABLES

Page

## ACKNOWLEDGEMENTS

I would like to firstly express my deepest gratitude to my committee chair and my academic advisor, Distinguished Professor Enrique J. Lavernia, for offering me this amazing opportunity to unveil the mystery of deformation twinning in Mg and always being supportive of my research ideas. Though we met with some obstacles, I know he is always by my side to help and guide. It is my honor and luck to have him supervise my Ph.D. study.

I would like to thank my committee members, Professor Julie M. Schoenung and Professor Penghui Cao. They have kindly offered valuable input and insights on my Ph.D. study and dissertation. Professor Julie M. Schoenung also has served as my academic advisor for two years during the time with unexpected hardship. I really appreciate it that I was not walking alone.

I would also like to acknowledge the expertise and helpful suggestions from the NSF DMREF project team. I would like to name all of them: Distinguished Professor Enrique J. Lavernia, Professor Julie M. Schoenung, Professor Timothy J. Rupert from UC Irvine, Professor Irene J. Beyerlein from UC Santa Barbara and Professor Subhash Mahajan from UC Davis as well as student collaborators Dr. Xin Wang, Dr. Yang Hu, Dr. Zhifeng Huang, Dr. Pulkit Garg, Dr. Jiaxiang Wang and Dr. Krishna Yaddanapudi. I enjoyed so many interesting discussions on Mg research we have had, through which I learned not only the scientific knowledge, but also how to do the research as a scientist.

And I will not forget, a sincere thank you to the Enrique J. Lavernia Research Group and the Julie M. Schoenung Research Group. I received endless technical and mental support from my

colleagues that helped me along the way towards my Ph.D. dissertation defense. I wish I could stay in the fabulous team a little longer.

Last but not least, I would like to say one more thank you to my family in China. Though we do not talk too much, I know they are always there for me wherever I go, and I can always feel the love and care they want to express.

I thank Elsevier B.V. for permission to include Chapter Three of my dissertation, which was originally published in *Scripta Materialia*. The co-author listed in this publication, including Dr. Xin Wang, Dr. Yang Hu, Prof. Subhash Mahajan, Prof. Irene J. Beyerlein, Prof. Enrique J. Lavernia, Prof. Timothy J. Rupert, and Prof. Julie M. Schoenung, directed and supervised research which forms the basis for Chapter Three.

Images in the introduction were reproduced from *Metallurgical and Materials Transactions A*, *Journal of Applied Mechanics*, *Acta Materialia* and *Nature Communications* and are used under fair use.

I also acknowledge financial support provided by the National Science Foundation (NSF CMMI-1729829, NSF CMMI-1729887 and NSF CMMI-1723539).

# VITA

## Kehang Yu

2013-17 B.S. in Materials Science, Fudan University, Shanghai, China

2017-22 Ph.D. in Materials Science and Engineering,
University of California, Irvine

## FIELD OF STUDY

Microstructure, plasticity, and their impacts on mechanical properties of structural materials

## PUBLICATIONS

- **Yu, K.**, Wang, X., Mahajan, S., Beyerlein, I.J., Cao, P., Rupert, T.J., Schoenung, J.M. and Lavernia, E.J. Twin nucleation from disconnection-dense sites between stacking fault pairs in a random defect network. To be submitted.
- **Yu, K.**, Wang, X., Mahajan, S., Rupert, T.J., Beyerlein, I.J., Cao, P., Schoenung, J.M. and Lavernia, E.J. Influence of non-glide stresses on {10-12} twin boundary migration in Mg. To be submitted.
- **Yu, K.**, Wang, X., Wang, J., Mahajan, S., Rupert, T.J., Beyerlein, I.J., Schoenung, J.M. and Lavernia, E.J. An EBSD-based statistical analysis on twin evolution in Mg-Y alloys. To be submitted.
- Wang, X., Hu, Y., **Yu, K.**, Mahajan, S., Beyerlein, I.J., Lavernia, E.J., Rupert, T.J. and Schoenung, J.M., 2022. Room Temperature Deformation-induced Solute Segregation and its Impact on Twin Boundary Mobility in a Mg-Y Alloy. Scripta Materialia, 209, p.114375.
- Wang, X., Zheng, B., **Yu, K.**, Jiang, S., Lavernia, E.J. and Schoenung, J.M., 2021. The role of cell boundary orientation on mechanical behavior: A site-specific micro-pillar characterization study. Additive Manufacturing, 46, p.102154.
- Wang, X., Zheng, B., **Yu, K.**, Jiang, S., Zhou, Y., Lavernia, E. and Schoenung, J., 2021. Understanding the effect of cellular structures on mechanical behavior of additively manufactured 316L stainless steel. Microscopy and Microanalysis, 27(S1), pp.2678-2680.
- Wang, J., Wang, X., **Yu, K.**, Rupert, T.J., Mahajan, S., Lavernia, E.J., Schoenung, J.M. and Beyerlein, I.J., 2021. Manipulating deformation mechanisms with Y alloying of Mg. Materials Science and Engineering: A, 817, p.141373.
- Wang, X., Jiang, L., Cooper, C., **Yu, K.**, Zhang, D., Rupert, T.J., Mahajan, S., Beyerlein, I.J., Lavernia, E.J. and Schoenung, J.M., 2020. Toughening magnesium with gradient twin meshes. Acta Materialia, 195, pp.468-481.
- Yan, X., Liu, C., Gadre, C.A., Dai, S., Gu, L., **Yu, K.**, Aoki, T., Wu, R. and Pan, X., 2019. Unexpected strong thermally induced phonon energy shift for mapping local temperature. Nano Letters, 19(10), pp.7494-7502.

- **Yu, K.**, Yang, C., Wang, J., Yu, J. and Yang, Y., 2019. Study on the strength of diameter-reducing solder balls by shear and pull tests. Soldering & Surface Mount Technology.
- Yang, C., Wang, L., **Yu, K.**, Wang, J., Xiao, F. and Zhang, W., 2018. Assess low-k/ultralow-k materials integrity by shear test on bumps of a chip. Journal of Materials Science: Materials in Electronics, 29(19), pp.16416-16425.
- Yan, X., Gadre, C.A., Dai, S., **Yu, K.** and Pan, X., 2018. Investigating Thermal Behavior of Surface Phonon in SiC by in-situ Vibrational Spectroscopy. Microscopy and Microanalysis, 24(S1), pp.416-417.

## ABSTRACT OF THE DISSERTATION

Influence of Stress-Strain Fields on the Behavior of Deformation Twins in Mg

by

Kehang Yu

Doctor of Philosophy in Materials Science and Engineering

University of California, Irvine, 2022

Distinguished Professor Enrique J. Lavernia, Chair

Magnesium (Mg) is of interest as a lightweight structural material, given its potential for energy-efficient and eco-friendly applications. However, Mg and its alloys have a hexagonal close packed structure that is characterized by an inherent plastic anisotropy which leads to poor formability and low strength, thereby limiting their use in many important engineering applications. Deformation twinning, an important plastic deformation mode in Mg, critically influences the strength and ductility of Mg. Consequently, a fundamental understanding of twin behavior under different stress and strain conditions is critical to optimize the performance of Mg and its alloys and thereby broaden their applicability in engineering systems.

In this dissertation research, experimental studies, using electron backscatter diffraction (EBSD) and scanning transmission electron microscopy, were used in combination with atomistic simulations using molecular dynamics and the nudged elastic band method to provide insight into twin behavior and investigate how the stress and strain fields modulate deformation twinning in Mg. The results from this dissertation research established multiple correlations between grain-scale microstructural characteristics and twin behavior by collecting and analyzing twin evolution information from large EBSD datasets and established the preferred

conditions for twin nucleation, propagation, and growth. We observed room temperature, deformation-induced solute segregation in a Mg-Y alloy at faceted $\{10\bar{1}2\}$ twin boundaries. The segregated Y atoms exert a pinning effect and lead to anisotropy on the mobility of twin boundaries. We calculated the stress-strain field modulated energy barrier for coherent twin boundary migration and found that there is a power-law relationship between the rate of CTB migration and the ratio between the twin resolved shear stress and the critical resolved shear stress for CTB migration. We confirmed the presence of a pure-shuffle twin nucleation and early-stage growth mechanism at disconnection-dense sites between stacking faults in a random defect network under deformation. The twin variant selection was found to be correlated with the line direction of the disconnection at the nucleation site. These key findings deepen our understanding of the fundamental mechanisms that govern twin behavior and provide alloy design pathways to control the mechanical response of Mg alloys by engineering the microstructure of deformation twins.

# Chapter 1: Introduction

## 1.1. Background and motivation

Magnesium (Mg), one of the most abundant elements on earth's crust, has received much research attention in the past a few decades as a possible lightweight candidate material for structural applications. This growing interest is stimulated by, for example, the need for lightening of automobile vehicles and hence the improvement of fuel efficiency for transportation [1,2]. The use of Mg in these applications will greatly benefit our society and environment – quantitatively each 100-kilogram reduction in vehicle weight would reduce fuel consumption by 0.38 L/100 km and $CO_2$ emission by 8.7 g/km [1,3]. However, extensive application of Mg and its alloys has been hindered due to their limited strength and low ductility or formability, especially at room temperature [2,4]. Therefore, Mg processing including extrusion and forging must be done at a temperature range between 300 °C and 500 °C, which increases the cost of Mg processing. Moreover, the tension/compression yield asymmetry of extruded Mg alloys [5–7] as well as the strong anisotropy upon deformation of rolled Mg sheets [8–10] are barriers that prevent Mg from being utilized as a reliable structural material.

These poor mechanical properties have been attributed to Mg's hexagonal close packed (hcp) structure and the strong texture of polycrystal Mg and Mg alloys. The Von Mises criterion indicates that there have to be at least 5 independent active slip systems for a polycrystalline material to undergo a homogeneous plastic deformation without cracking [11]. However, the hcp structure of Mg greatly limits the number of available slip systems, especially under room temperature. Table 1.1 and Table 1.2 summarize the possible slip systems and modes of

deformation twinning in Mg, respectively, and Figure 1.1 illustrates the crystallographic details of these major plastic deformation modes. Figure 1.2 shows the critical resolved shear stress (CRSS) of a few representative plastic deformation modes as a function of temperature. Among the slip systems in Table 1.1, only 2 modes of basal <**a**> slip and 2 modes of prismatic <**a**> slip can be easily activated once the strain level exceeds the elastic limit and independent with respect to the rest. The fact that hot-rolled or extruded polycrystal Mg shows a strong basal texture further enhances the mechanical anisotropy and impedes the formation of non-<**a**> slip in Mg [1]. One additional plastic deformation mode still needs to be introduced to accommodate *c*-axis strain and comply with the Von Mises criterion [11]. Shown by the low CRSS value in Figure 1.2, the tension $\{10\bar{1}2\}$ deformation twin is the most frequently observed plastic deformation mode under ambient temperature which accommodates *c*-axis tension and satisfies the Von Mises criterion in deformed polycrystal Mg. Other non-basal dislocation slip, and modes of deformation twinning are possible to be present in deformed polycrystal Mg, but with far less frequency and higher required stress.

Table 1.1. Possible modes of dislocation slip in Mg. Adapted from [11].

| Burgers vector | Slip plane | Crystallographic elements | Number of independent |
|---|---|---|---|
| **a** | Basal | (0002) $<11\bar{2}0>$ | 2 |
| | Prismatic | $\{1\bar{1}00\}$ $<11\bar{2}0>$ | 2 |
| | Pyramidal | $\{10\bar{1}1\}$ $<11\bar{2}0>$ or $\{10\bar{1}2\}$ $<11\bar{2}0>$ | 4 |
| **c** | | {hki0} [0001] | |
| **c**+**a** | Pyramidal | $\{10\bar{1}1\}$ $<11\bar{2}\bar{3}>$ or $\{11\bar{2}2\}$ $<11\bar{2}\bar{3}>$ or $\{2\bar{1}\bar{1}1\}$ $<11\bar{2}\bar{3}>$ | 5 |

Table 1.2. Possible deformation twinning modes in Mg. Adapted from [11].

| $K_1$ (Twinning plane) | $K_2$ (Conjugated twinning plane) | $\eta_1$ (Twinning direction) | Twin shear |
|---|---|---|---|
| $\{10\bar{1}1\}$ | $\{10\bar{1}3\}$ | $<10\bar{1}\bar{2}>$ | 11.35% |
| $\{10\bar{1}2\}$ | $\{10\bar{1}2\}$ | $<10\bar{1}\bar{1}>$ | 6.49% |
| $\{11\bar{2}2\}$ | $\{11\bar{2}4\}$ | $1/3<11\bar{2}\bar{3}>$ | 17.45% |
| $\{11\bar{2}1\}$ | (0002) | $1/3<\bar{1}\bar{1}26>$ | 8.67% |

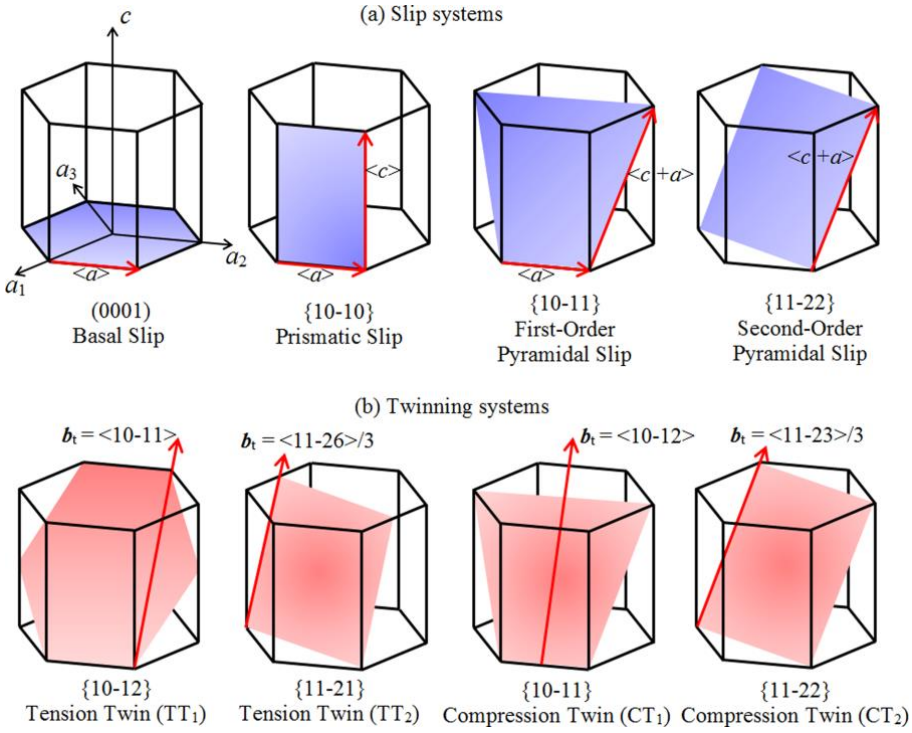


Figure 1.1. Major plastic deformation modes in Mg, including (a) slip systems with slip planes and Burgers vectors denoted and (b) twinning systems with twinning planes and twinning directions denoted. Reprinted from [12].

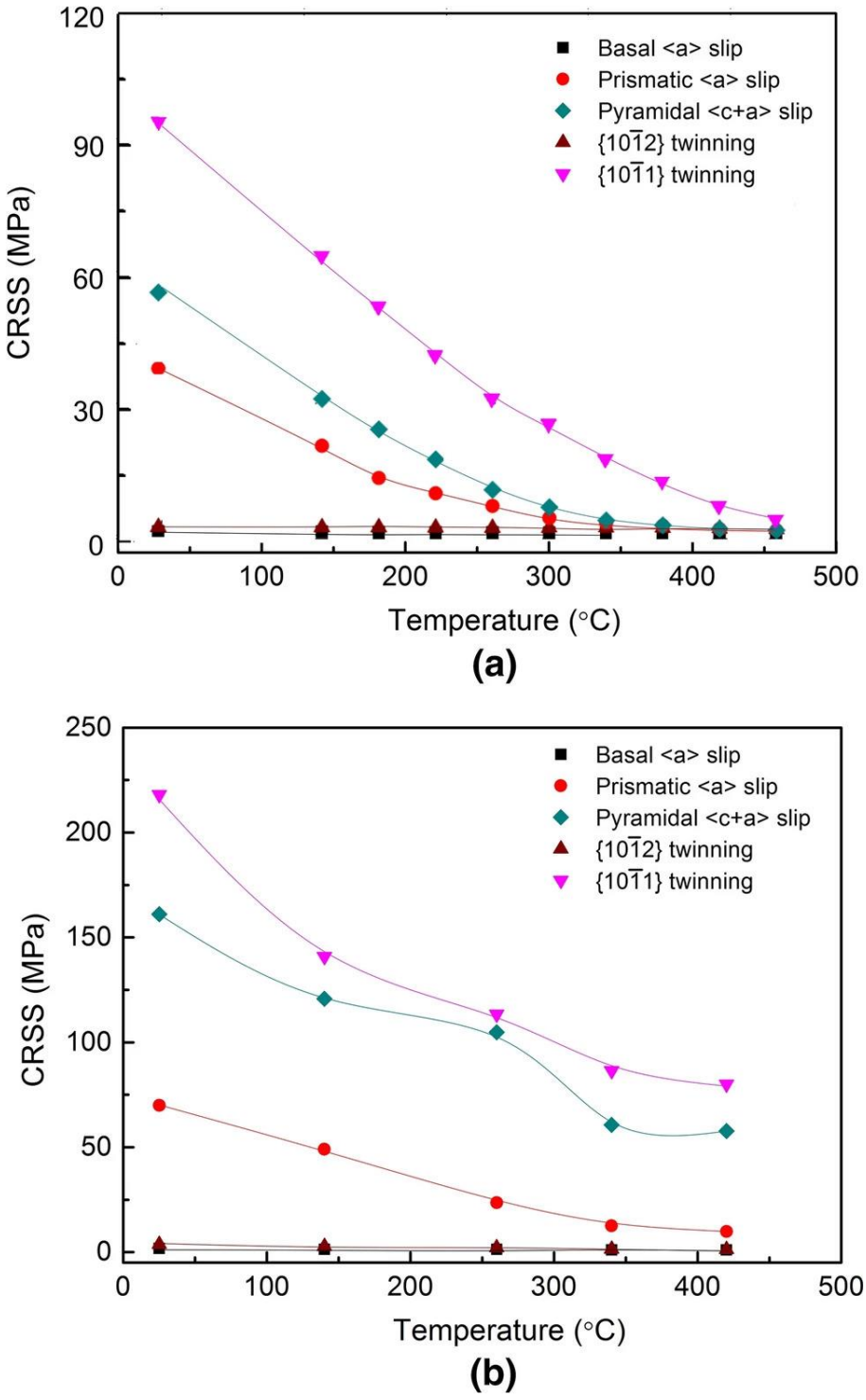


Figure 1.2. Critical resolved shear stress (CRSS) values for representative plastic deformation modes under different temperatures in (a) pure Mg single crystals and (b) Mg-1 wt. % Al single crystals. Reprinted from [1].

By modulating the relative activity of all the plastic deformation modes through alloying, heat treatment, work hardening, and other strategies, the strength and the ductility of Mg and Mg alloys can be engineered [4]. As an example, alloying Mg with one or more elements is found to be able to weaken the strong basal texture of as-rolled samples and enable the nucleation of other non-<**a**> slip to optimize the room temperature formability of Mg [1]. The mechanism behind easier activation of <**c**+**a**> dislocations is that the addition of some alloying elements can reduce the $I_1$ stacking fault energy, while $I_1$ stacking fault is a dominant mode of stacking faults in hcp structure and can serve as a heterogenous nucleation source for <**c**+**a**> dislocations [13,14] and therefore reduce their critical resolved shear stress (CRSS). In recent years, Mg-rare earth (RE) alloys and Mg-Li based alloys show significant improvements of mechanical properties [1,2].

From the discussion above it is evident that improving the mechanical properties of Mg for use in structural applications will require a fundamental understanding of the mechanisms that govern the behavior of all the possible plastic deformation modes, especially deformation twins. For instance, a precise understanding of the twin nucleation mechanism in hcp materials has eluded investigators for decades leading to the formulation of many hypotheses that await validation [15,16]. Precise knowledge of twin nucleation mechanisms will facilitate the engineering of twin structures in Mg thereby facilitating the optimization of strength and ductility, for example. The plastic deformation in Mg, especially under a stress far larger than the yield stress, results in complex interactions between all active plastic deformation modes. By visualizing and analyzing twin-twin or twin-slip interactions, paying particular attention to possible dislocation or disconnection transmission at twin boundaries, one can evaluate how effectively twin boundaries can serve as barriers and how twin boundaries may interact with dislocations to allow absorption and/or transmission to better modulate the plastic flow in Mg for

strength and ductility [17–19]. Mg alloying is often accompanied by the segregation of solute atoms or the precipitation of a possible new phase. Hence, studies of segregation and precipitation phenomena help our understanding of defect transition and provide the knowledge required for devising strengthening strategies for Mg since both of these phenomena affect boundary mobility and hence the plastic flow [20–22].

### 1.2. Deformation twinning in Mg and an overview of its behavior

It should be noted that the possible modes of deformation twinning in Mg are many, including the most commonly observed $\{10\bar{1}2\}\langle 10\bar{1}\bar{1}\rangle$ twin and $\{10\bar{1}1\}\langle 10\bar{1}\bar{2}\rangle$ twin [15]. The former one accommodates the tensile strain along the *c*-axis while the latter one accommodates the compressive strain along the *c*-axis. Experimental results show they are the easiest modes to be activated to provide an out-of-basal-plane strain during the deformation. The $\{10\bar{1}2\}\langle 10\bar{1}\bar{1}\rangle$ twin will be discussed hereafter since it is more frequently observed in the deformed polycrystal Mg.

The $\{10\bar{1}2\}$ deformation twins develop in stages after the deformation is applied, from nucleation in the form of an embryo, to propagation into a planar-shaped lamella viewing along the zone axis shared by the basal plane in matrix and that in twin (i.e., $\boldsymbol{K}_1 \times \boldsymbol{\eta}_1$) and finally to growth or sometimes called thickening. Twin nucleation marks the beginning of the evolution of a deformation twin. While the mechanism of twin nucleation in Mg has yet to be completely understood, most studies agree that in polycrystalline Mg, the deformation twin nucleates in a heterogenous manner, which means that the formation of the twin embryo is assisted by other defects such as grain boundaries, single- or multi-layered stacking faults instead of a pure stress

field [15]. Available evidence suggests that the critical resolved shear stress (CRSS) criteria is less accurate for predicting deformation twinning than it is for predicting dislocation slip – twin nucleation tends to occur within a broader resolved shear stress range rather than a well-defined singular value [23,24].

Inspection of the published literature reveals that there are primarily two categories of the theories on how defects assist the $\{10\bar{1}2\}$ twin nucleation – the shear-shuffle model and the pure shuffle model. The former one assumes the importance of a precursor structure to the $\{10\bar{1}2\}$ twin embryo, twinning disconnections (TDs) with a Burgers vector of $\frac{1}{15} < 10\bar{1}\bar{1} > \{10\bar{1}2\}$ and a step height of 2 atomic layers [25,26]. Pre-existing dislocations may dissociate or combine with other defects to generate multiple TDs. There are plenty of possible pathways for the nucleation of TDs. Under stress concentration, multiple TDs may form by, for example, the combination of a basal <**a**> slip and a pyramidal-I <**c**+**a**> slip [27]; the dissociation of edge <**c**> and mixed <**c**+**a**> dislocations [28]; the interaction between a basal dislocation and a $\{11\bar{2}1\}$ twin [29] or the "pole mechanism". In this "pole mechanism" a sessile pole dislocation acts as an anchor and allows for the dissociation of a partial dislocation and therefore the resultant TD rotates around the pole dislocation to form a twin embryo [15,30,31]. After the source of TDs is clarified, we note that there are also two theories on how TDs participate into the twin nucleation – (1) the normal-twinning mechanism suggests that a stable twin nucleus is formed by the simultaneous nucleation of a few twinning TDs; (2) the zonal-twinning mechanism suggests that the nucleus is formed by the simultaneous nucleation of not only a few TDs, but an additional partial dislocation [26]. It follows from these theories that there should exist a critical size for the twin embryo to be stable. Under the normal-twinning mechanism, this value is predicted to be 6 atomic layers; under the zonal-twinning mechanism, this value should be 17 atomic layers [26].

The pure-shuffle model, however, does not necessarily require the participation of TDs into the twin nucleation process. Instead, this model postulates that atomic shuffling, a non-affine (i.e., the displacements cannot be completed solely by a linear transformation) and diffusionless atomic displacement, akin to that involved in phase transformations, directly leads to twin nucleation. While defects are still needed to assist the atomic shuffling, this mechanism requires far fewer precursors to be present, if any. The shuffling-induced twin nuclei feature: (1) a basal-prismatic (BP) and prismatic-basal (PB) transition and subsequently BP and PB interfaces bounding the twin embryo, and (2) a deviation of the misorientation angle from the ideal 86.3° to approximately 90° which complies with the basal-to-prismatic and prismatic-to-basal transition [16,32–34]. Figures 1.3 and 1.4 shows two examples for the twin nucleation following the shear shuffle model and the pure-shuffle model, respectively. As a summary, the shear-shuffle and the pure-shuffle model represent two mutually competing pathways of twin nucleation, which often depend on the microstructures and stress conditions at a specific site.

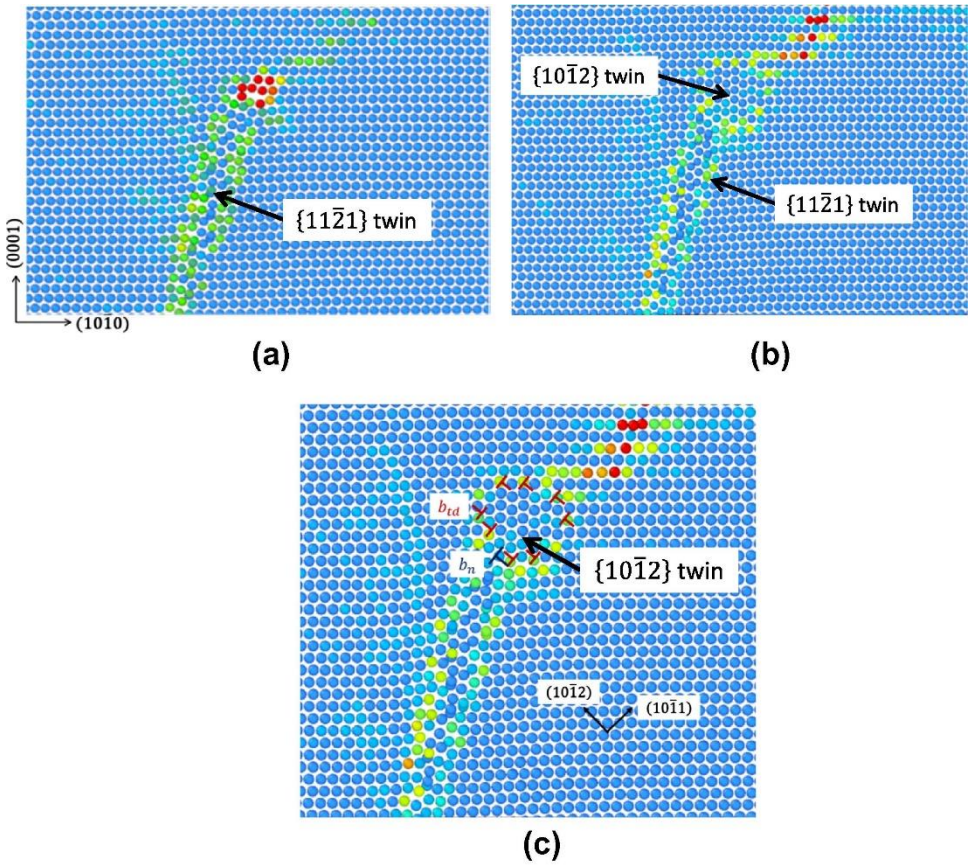


Figure 1.3. A shear-shuffle twin nucleation mechanism featuring the formation of TDs under the interaction of a basal dislocation and a {11-21} twin. The atoms are colored based on the excess potential energy with red representing a higher value. (a) shows the large excess energy at the junction of the basal dislocation and {11-21} twin. (b) shows a {10-12} twin embryo. (c) shows the same twin embryo but with bounding TDs and a partial dislocation. Reprinted from [29].

The $\{10\bar{1}2\}$ twin propagation and the twin growth both result in a size increase of the deformation twin in two dimensions, respectively. The twin propagation happens in the earlier stage of the twin evolution under deformation and results in the twin size increase along the twinning direction. It is mostly completed by the movement of the twin tip, which may consist of multiple TDs [15]. The twin growth represents the thickening of the twin after the fast twin propagation. During growth, the twin boundary must migrate as the twin grows along the normal direction to the twinning plane. Twin boundary migration is generally proposed to be assisted by

TDs. TDs are highly mobile and can glide through both the twin boundary, the basal-prismatic (BP) interface and the prismatic-basal (PB) interface [35] to enable the reorientation of crystal and therefore twin boundary migration.

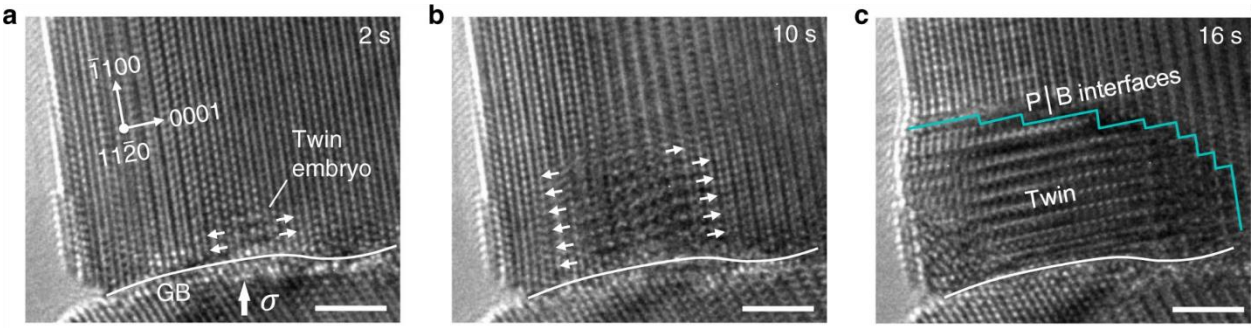


Figure 1.4. A pure-shuffle twin nucleation mechanism featuring the 90° B-P transformation observed by *in situ* high-resolution transmission electron microscopy (HRTEM). (a)-(c) shows sequential HRTEM images with time labelled. Scale bars represent the length of 2 nm. Reprinted from [33].

Since TDs are also structurally necessary for both twin propagation and twin growth, the sources of TDs during these two processes have been an important research topic [36,37]. The nucleation of TDs is mostly likely to be slip-assisted for $\{10\bar{1}2\}$ twins [36,38], which means TDs form as a result of the interaction between other slip and twin interface. Other studies on the kinetics of twin boundary migration have shown that a lower energy barrier allows an easier glide for TDs of $\{10\bar{1}2\}$ deformation twins compared to those of $\{10\bar{1}1\}$ twins [39]. Hence, by studying the energetic feasibility of TD glide, the stable configuration of TDs for each twinning mode can be identified [40].

Recent studies have paid particular attention to the three-dimensional (3D) structure of $\{10\bar{1}2\}$ deformation twins [41–44]. The well-known and most visualizable $\{10\bar{1}2\}$ coherent twin boundary and BP/PB interface are only part of the interface segments (or the interface facets) that bound the $\{10\bar{1}2\}$ twin, considering the $\{10\bar{1}2\}$ twin as a 3D object. The twin propagation

and the twin growth are, strictly speaking, caused by the migration of all these interface facets contributes. Due to the improvement in transmission electron microscopy (TEM) and simulation techniques, more interface facets of the $\{10\bar{1}2\}$ twin, such as the conjugate $\{10\bar{1}\bar{2}\}$ twin boundary, the semi-coherent twist $\{2\bar{1}\bar{1}0\}$ prismatic-prismatic boundary and the twist/tilt $\{\bar{1}101\}$ pyramidal-pyramidal boundary and other boundaries with higher indices [41,43,44]. Judged by the observed irregular shape viewing along the direction perpendicular to the twinning plane, the mobility of these high energy facets and the twin growth assisted by their motion is locally controlled and is attributable to the mobility difference of corresponding TDs to these facets, mostly that between the edge and the screw TDs [43]. It has also been found that the interaction between connecting facets will make a significant difference on their mobility and one facet may have various structures (i.e., states) upon applied stress that will vastly change its mobility [44].

Double twinning represents the phenomenon that there is one or more secondary twins within the primary twin [45,46]. The primary twin then will be matrix with respect to the secondary twin. Two commonly observed double twinning modes are $\{10\bar{1}1\}$-$\{10\bar{1}2\}$ and $\{10\bar{1}3\}$-$\{10\bar{1}2\}$, with the former in the pair being the primary twin. $\{10\bar{1}2\}$-$\{10\bar{1}2\}$ double twinning is also possible but less common. Modes of $\{10\bar{1}1\}$-$\{10\bar{1}2\}$ and $\{10\bar{1}3\}$-$\{10\bar{1}2\}$ double twinning are mechanically enabled because a tension secondary twin inside the domain of the compression primary twin also accommodates compression along the *c*-axis like the primary twin. Different from them, $\{10\bar{1}2\}$-$\{10\bar{1}2\}$ double twinning is the consequence of twin-twin interactions, for example, the case where one primary $\{10\bar{1}2\}$ twin impinges on the boundary of another primary $\{10\bar{1}2\}$ twin [1,47,48]. Based on these mechanisms, there is a preferred variant relationship between the primary and the secondary twin [46,48].

Finally, as a reverse process with respect to twinning, detwinning may happen when the applied load is released or reversed (e.g., under cyclic loading). Detwinning will shrink the size of the deformation twin and therefore relax *c*-axis strain possibly by the opposite migration of twin boundaries and finally TDs' transition into dislocations in matrix [49].

### 1.3. Electron backscatter diffraction (EBSD)

Electron backscatter diffraction (EBSD) in the scanning electron microscope (SEM) is a materials characterization method that can identify the phase and determine the orientation of crystalline materials and thereby enhances our understanding of materials' microstructure and properties [50]. Consequently, EBSD is adopted in this dissertation research to detect $\{10\bar{1}2\}$ twins and understand their evolution behavior during deformation in Mg alloys.

Phase identification and orientation determination is technically enabled by the detection of EBSD patterns, or Kikuchi diffraction patterns in essence. EBSD patterns are acquired by using a stationary electron beam to probe the surface of a highly tilted (usually by 70°) sample. The incident electrons that are inelastically scattered within the sample and only lose a small amount of their energy would serve as the source of diffraction electrons. Then some of these electrons satisfy the Bragg diffraction conditions and therefore are diffracted into two cones of intensified electron signal with a semi-angle of (90°-θ) by each lattice plane, while θ denotes the diffraction angle in Bragg's law. These two cones will appear to be a pair of bright straight lines, known as a Kikuchi band, when they are intercepted by the screen of the EBSD detector. All these Kikuchi bands resulting from the electron diffraction by each crystallographic plane altogether form the EBSD pattern which contains the information of the phase and the crystal orientation [50]. With

analysis of the EBSD pattern following the algorithm of band detection, for example, the Hough Transform [51], the computer is able to reveal the phase and orientation information automatically [50]. The EBSD mapping is then made possible by scanning the sample surface and showing the phase or the orientation of each pixel in a single map.

After the EBSD mapping of Mg or Mg alloys, the twin domain in an EBSD map can be labelled according to the misorientation between the twin domain and the neighboring matrix domain. The twinning relationship indicates that for the rotation from matrix to the $\{10\bar{1}2\}$ twin, the rotational angle must be around 86.3° and the rotational axis must be one of the six variants of the *a*- (i.e., $<11\bar{2}0>$) axis [52]. Furthermore, the EBSD data including the information such as the twin variant, the twin morphology, and the twin location with respect to the grain can also help understand the twin distribution and behavior.

### 1.4. Scanning transmission electron microscopy (STEM)

Scanning transmission electron microscopy (STEM) imaging is operated with a convergent beam, different from TEM imaging which uses parallel beam. After tuning the convergency of electron beam, the convergent beam, which is kept being parallel to the optic axis during imaging, will then be scanned across the sample pixel by pixel to construct the STEM image. There are a few imaging modes of STEM categorized by the angular position of the detector, including bright-field, angular dark-field and high-angle angular dark-field (HAADF). They each collect signals from transmitted electrons with different scattering angles [53,54].

In this dissertation, HAADF-STEM is applied to characterize the segregation at twin boundaries. The signals received by the HAADF detector have a maximized effect of Rutherford-scattering

while the diffraction-contrast effects are minimized because of the high-angle position the detector is placed at (> 50 mrad). Therefore, HAADF-STEM images are able to visualize the segregation of heavy elements due to the sharp Z-contrast of this imaging mode [53].

## 1.5. Atomistic simulation methods

### 1.5.1. Introduction to molecular dynamics (MD)

Molecular dynamics (MD) is a computational method widely used for the simulation of atomic movements in space under a given set of conditions. Usually, the trajectories of atoms are solved by treating each atom as a point mass and applying numerical integration of Newton's equation of motion to them with defined initial condition and boundary condition, while the interatomic force is calculated through an interatomic potential describing the interaction between atoms by the negative gradient of potential energy for a specific atom with respect to its current position. A feasible way to update the positions and the velocities of atoms timestep by timestep is to use the Verlet integration [55]. MD simulations are able to extract some meaningful microscopic or macroscopic information of the system from the motion data of the ensemble of all atoms, including diffusivity, phase diagrams and plastic deformation [55], which is one of the key research topics of this dissertation.

The strengths and the shortcomings of MD are evident from its assumptions as far as a working mechanism. The atomistic mechanism of a physical event, which is usually hard to visualize using an experimental method, can be easily simulated through MD within a reasonable amount of time. On the other hand, one of the concerns of MD calculations is the limitation of its time scale. By using discrete timesteps to calculate a continuous evolution of the system, the timestep

size must not be too long and therefore MD often works at the time scale of microseconds to nanoseconds. In other words, it is hard for MD to operate on a system or an event which evolves at an extremely low rate, such as diffusion [56,57]. Despite these drawbacks, MD methods are essential to provide important insight into the atomistic mechanism of deformation twinning in Mg [25,28,58] as long as the setup of the MD model is physically reasonable enough to avoid these drawbacks.

### 1.5.2. Nudged elastic band (NEB)

The minimum energy path (MEP) is defined as the path in phase space along which the energy gradient is parallel to the path itself among all the possible paths connecting the designated initial and final states [59]. At any point along the MEP, the perpendicular-to-the-MEP component of the force acting on the atoms remains zero [60]. The MEP contains the information regarding the atomic movement during the transition. The calculation of an MEP enables the understanding of the atomistic mechanism as well as the energy barrier during a certain transition or reaction and allows access to a time scale on the same order of experimentally-relevant time scale, which is hard to accomplish using conventional MD as mentioned above [56,61]. To find such a MEP, nudged elastic band (NEB) has been proved to be a feasible method by many studies [62–65].

NEB conducted in the thesis is performed using LAMMPS. The algorithm contains two stages of the NEB calculation. After defining the configuration of the first and the last replica, the algorithm will construct a few replicas (i.e., images) of the system representing the evolution process from the first to the last replica, and assign an initial guess to them, usually by executing a linear interpolation of atomic coordinates between the first and the last replica. In the first stage, the initial guess of replicas should converge towards MEP. This is realized by applying the force $\boldsymbol{F}_i$ in the following equation,

$$\boldsymbol{F}_i = \boldsymbol{F}_i^{spring}|_{\parallel} - \nabla E(\boldsymbol{R}_i)|_{\perp} \tag{1.1}$$

to each replica $i$, where $\boldsymbol{F}_i^{spring}|_{\parallel}$ is the parallel-to-the-MEP component of the inter-replica nudging force and $\nabla E(\boldsymbol{R}_i)|_{\perp}$ is the perpendicular-to-MEP component of the physical force because of the gradient of the potential energy. The first term, $\boldsymbol{F}_i^{spring}|_{\parallel}$ can be further expressed as

$$\boldsymbol{F}_i^{spring}|_{\parallel} = k(|\boldsymbol{R}_{i+1} - \boldsymbol{R}_i| - |\boldsymbol{R}_i - \boldsymbol{R}_{i-1}|) \cdot \hat{\boldsymbol{\tau}}_i \hat{\boldsymbol{\tau}}_i \tag{1.2}$$

, where $\boldsymbol{R}_{i-1}$, $\boldsymbol{R}_i$, $\boldsymbol{R}_{i+1}$ represent three consecutive replicas with replica $i$ sitting in between, $\hat{\boldsymbol{\tau}}_i$ is the unit vector tangent at replica $i$ and $k$ is the spring constant in NEB and is usually kept the same for all replicas. This linear nudging force is implemented to let each replica equally spaced. The second term, $\nabla E(\boldsymbol{R}_i)|_{\perp}$ can be expressed as

$$\nabla E(\boldsymbol{R}_i)|_{\perp} = \nabla E(\boldsymbol{R}_i) - \nabla E(\boldsymbol{R}_i) \cdot \hat{\boldsymbol{\tau}}_i \tag{1.3}$$

, where E represents the potential energy of each replica. It allows the MEP to converge towards the MEP. In the second stage of NEB, which is sometimes called barrier-climbing NEB or climbing-image NEB, a virtual force will be applied to the specific replica with the highest potential energy after the first stage to drive it up to the exact saddle point, while the other replicas rearrange themselves along the MEP to keep equally spaced. The force imposed to the highest energy replica is

$$\boldsymbol{F}_s = -\nabla E(\boldsymbol{R}_s) + \nabla E(\boldsymbol{R}_s)|_{\parallel} + \nabla E(\boldsymbol{R}_s)|_{\parallel} \tag{1.4}$$

, where $\boldsymbol{R}_s$ denotes the replica with the highest energy after the first stage of NEB. While the first two terms in Equation (1.4) is exactly the same as $-\nabla E(\boldsymbol{R}_i)|_{\perp}$ in Equation (1.1) and therefore still confines replica $s$ to the MEP, the third term is a force along the elastic band induced by the

inverted potential and hence allows $\boldsymbol{R}_s$ to move up the potential energy surface to the actual saddle point [60].

### 1.6. Twin-mesh engineering

Twinning has the potential to strengthen and toughen the material simultaneously, while other strengthening mechanisms, such as precipitation hardening, generally sacrifice the toughness of the material [66]. This idea is originated from the finding that in face center cubic (fcc) Cu, nanoscale twins are able to improve the strength without a significant loss of ductility [67]. The mechanisms for strengthening are that twin boundaries can act as barriers to dislocation motion since dissociations of dislocation is not energetically favorable without necessary stress concentration at twin-slip band intersection [68] and that for alloys, the segregation of solute atoms at the twin boundary also strengthens the material through the pinning effect [20]. The toughening is enabled by the fact that the twin boundary still allows some of dislocation slip to get through or to be absorbed by the boundary itself [11,17–19,67,68], so the material does not fracture in a brittle manner. In polycrystal Mg and Mg alloys, adjoined twin pairs attached to the same grain boundary have been frequently observed under different temperature and strain rate [69]. This junction of twins or the ensuing twin-twin interactions allow for the possibility to "design" a twin structure and alleviate the strong texture as well as the anisotropy and boost the microstructural stability by the three-dimensional configuration of the twin network [66]. In summary, materials with a high density of twins would gain a significant improvement on strength and toughness due to the above-mentioned mechanisms.

While the same type of the dislocation slip is quite microstructurally analogous, deformation twinning features a significant statistical variation in its morphology, size, variant and spatial distribution [23]. This allows researchers to modulate the twin's microstructural characteristics by controlling the grain size [23], the distribution of grain orientation (i.e., the texture) [23], the applied strain [70], and alloying elements [2]. The idea of "twin-mesh engineering" tries to achieve the goal of hardening and toughening by building 3D twin meshes in polycrystalline Mg or Mg alloys. As one of the ultimate goals of this study, twin-mesh engineering has been recently proven to be promising in Mg as supported by the finding that: (1) it is possible to generate a twin network composed of thinner twins in compressed coarse-grained Mg-4 wt. % Li [45] and SPEX-milled pure Mg foil [71]; (2) parallel nanotwins with a high density are observed in Mg-8 wt. % Li compressed with ultrahigh hydrostatic pressure [72]; (3) the twin network/mesh optimizes the mechanical property of the Mg material [45,71].

### 1.7. Dissertation objectives and organization

The goal of this dissertation research was to use modeling and experimentation to provide insight into the mechanisms of twin behavior in Mg, particularly into the conditions that facilitate twin nucleation as well as to the behavior of twins under an applied stress field. To accomplish this goal, this thesis is organized as follows. First, Chapter 1 introduces the relevant background and the motivation of the thesis study and briefly explains the key methods that are used, and the subsequent chapters are arranged as follows:

- Chapter 2: An EBSD-based statistical analysis to investigate the $\{10\bar{1}2\}$ twin evolution in Mg-Y alloys during deformation and establish statistical correlations between grain-level microstructural characteristics and twin behavior.
- Chapter 3: A STEM-based characterization on room-temperature, deformation-induced Y segregation at faceted $\{10\bar{1}2\}$ twin boundaries in the form of Y-rich columns and nanoscale clusters in a Mg-3Y alloy.
- Chapter 4: An NEB-based simulation on a systematic study of the stress-dependent energy barrier of CTB migration.
- Chapter 5: Unexpected observation of twin nucleation from disconnection-dense sites between two stacking faults inside a randomly generated defect network using MD.
- Chapter 6: A summary of the dissertation and an outlook for future work to further enhance the understanding of deformation twinning in Mg and thereby enhance mechanical properties through twin-mesh engineering.

## Chapter 2: An EBSD-based Statistical Analysis on Twin Evolution in Mg-Y Alloys

### 2.1. Abstract

We report on an investigation of twin evolution in Mg-Y alloys using quantitative statistical analysis of large datasets acquired by electron backscatter diffraction. In particular we studied the influence of strain in Mg-3 wt. % Y (Mg-3Y) as well as the influence of Y concentration in four different Mg-Y alloys on twin evolution. Our results reveal multiple correlations between grain-scale characteristics and twin behavior. We show that the twin area fraction evolution in Mg-3Y follows a different trend than the simpler model effective in heavily textured Mg alloys. The $\{10\bar{1}2\}$ deformation twins are the most active in accommodating the plastic strain before profuse twin-twin interactions occur. The positive correlation between grain size/grain boundary perimeter and the probability of observing at least one twin inside the grain is confirmed for all strain levels for Mg-3Y and all Mg-Y alloys studied. The Schmid factor analysis shows a nearly constant ratio for the number fraction between three co-zone twin variant pairs. As the applied strain increases, the twin variant with a larger Schmid factor in the co-zone twin variant pair is preferred. The lower twin area fraction observed inside Mg-3Y is attributable to the higher Y concentration rather than to a weakened texture. A higher frequency of the co-zone and the 1$^{st}$ type non-co-zone twin-twin intersections in Mg-3Y is also observed. This study generally validates the notion that EBSD can be used as a promising data source to execute high-throughput analyses of microstructure, particularly in the case of crystallographic orientation-based features.

## 2.2. Introduction

Magnesium (Mg) is a promising lightweight material for structural applications. Such a lightweight structural material provides benefits and is particularly well suited for eco-friendly transportation by virtue of the potential weight savings in vehicles and hence fuel consumption. However, extensive application of Mg and its alloys in structural applications is impeded due to its limited room temperature ductility as well as its relatively low strength. These poor mechanical characteristics are attributed to the limited amount of active slip systems. To satisfy the von Mises criterion [11], $\{10\bar{1}2\}<10\bar{1}\bar{1}>$ tension twins and $\{10\bar{1}1\}<10\bar{1}\bar{2}>$ compression twins, in addition to basal <**a**> slip and prismatic <**a**> slip are frequently activated in polycrystalline Mg to allow for a homogenous plastic deformation without cracking [1].

Deformation twins play an important role in plastic deformation of Mg by: (1) accommodating *c*-axis strain [15]; (2) forming twin boundaries that may interact with or impede dislocation slip in different ways [17–19]; (3) modulating the texture of Mg by reorientating the crystal in the twin domain [70]; (4) sometimes leading to the formation of cracks and fractures [11,45]. Therefore, understanding the evolution of deformation twins under an applied strain is important to describe the plastic flow in Mg. Deformation twins do not nucleate, propagate, and grow totally in a random manner. So far there have already been many reported rules proposed to describe twin evolution in Mg and Mg alloys. For example, twin nucleation preferably happens in larger grains [23,73]; while the grain boundary is generally more likely to be the twin nucleation site due to stress concentration, grain boundaries with a lower misorientation angle provide preferred sites for twin nucleation [23,73–75]; the Schmid factor for each grain in reference to the twinning mode, provides a useful prediction on whether this twinning mode will be active or not, but with some exceptions, possibly due to microstructural features that occur at the nanoscale [23,73,76].

Mg-Y alloys, as one of the widely researched Mg-rare earth alloys, have an outstanding mechanical properties due to the weakening of the texture, the decreased critical resolved shear stress (CRSS) for <**c**+**a**> dislocations and the increased CRSS for twins [2,5,77]. However, to date there are limited quantitative reports how different the twin evolution in Mg-Y alloys is as a function of Y concentration and the applied deformation. Hence, to provide insight into twin behavior in Mg-Y and compare it with that in pure Mg and other Mg alloys, it would be helpful to pursue a systematic study on how the modification of properties by Y, such as the texture and the relative ease of multiple plastic deformation modes, change twinning, based on a substantial amount of experimental data.

In view of the above discussion, the goal of this study is to investigate twin evolution in Mg-Y alloys from two perspectives – (1) Mg-3 wt. % Y (Mg-3Y) compressed along rolling direction (RD) to multiple strain levels and (2) four binary solid solution Mg-Y alloys with different Y concentrations compressed along RD by the same strain. To visualize the microstructure of twins at the micron scale, electron backscatter diffraction (EBSD) was used to capture the crystallographic orientation on the cross-sections of Mg-Y alloys after deformation. After EBSD, the crystallographic orientation data were further processed by Microstructure Evaluation Tool for Interface Statistics (METIS) to output the data into structured query language (SQL) databases. The databases, which automate the identification of different types of twins and classify the twin statistics, enable a high-throughput quantitative analysis to understand the role of microstructural characteristics and alloy composition on twin evolution. A statistical study reveals some grain-scale local characteristics, including grain size, grain boundary perimeter, and grain orientation and sample-scale parameters such as the compressive strain and the alloying element concentration, all impact twinning, but in different ways. The correlation between

microstructural characteristics established through statistical analysis can provide insight into plasticity theories regarding twinning. The findings on the prediction of deformation twinning also help design materials with desired activity of deformation twinning by modulating the grain-level microstructure.

## 2.3. Experimental Methods

### 2.3.1. Material

Mg-0.2 wt. % Y (Mg-0.2Y), Mg-0.6 wt. % Y (Mg-0.6Y), Mg-1 wt. % Y (Mg-1Y) and Mg-3 wt. % Y (Mg-3Y) alloys (Helmholtz-Zentrum Geesthacht) were studied in this work. The four Mg-Y alloys, as cast ingots, were first homogenized and hot rolled at 500 °C with a thickness reduction of 50% to 6 mm. Subsequently, a recrystallization heat treatment was carried out for all Mg-Y alloys in order to remove all pre-existing twins and keep the grain sizes of each alloy nearly the same. The recrystallization parameters, as well as the grain sizes, are listed in Table 2.1.

Table 2.1. The recrystallization parameters and average grain sizes of Mg-Y samples studied in this work.

| Sample | Mg-0.2Y | Mg-0.6Y | Mg-1Y | Mg-3Y |
|---|---|---|---|---|
| Recrystallization conditions | 400 °C, 10 min | 400 °C, 10 min | 400 °C, 10 min | 450 °C, 10 min |
| Average grain size | 35 µm | 21 µm | 22 µm | 26 µm |

Figure 2.1 shows the optical microscopy images of the four Mg-Y alloys validating the twin-free starting structures, the equiaxed grains and the similar grain sizes (except for that of Mg-0.2Y due to the rapid grain growth under a low concentration of Y) following recrystallization. Figure 2.2 shows the starting texture of all four Mg-Y alloys characterized with X-ray diffraction

(XRD). The Mg-Y samples before deformation reveal a basal texture typical of Mg due to the rolling. However, as the concentration of Y increases, the so-called rare earth texture [2] starts to become more dominant, which indicates that the basal texture is weakened by the addition of rare earth elements such as Y in this study. Quantitatively, the maximum intensities of each (0002) pole figure are 16.7, 17.2, 9.1 and 7.1 multiples relative to that of a uniform distribution for Mg-0.2Y, Mg-0.6Y, Mg-1Y and Mg-3Y, respectively.

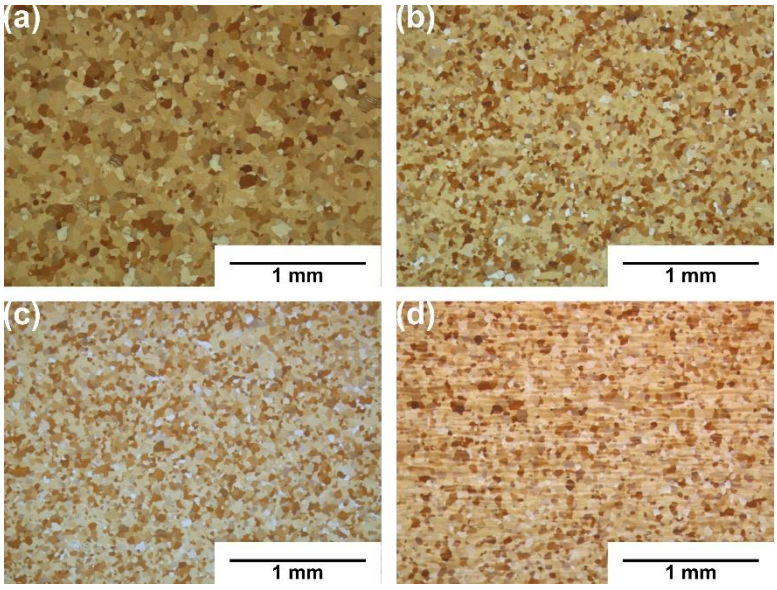


Figure 2.1. The optical microscopy images of (a) Mg-0.2Y, (b) Mg-0.6Y, (c) Mg-1Y and (d) Mg-3Y samples after recrystallization.

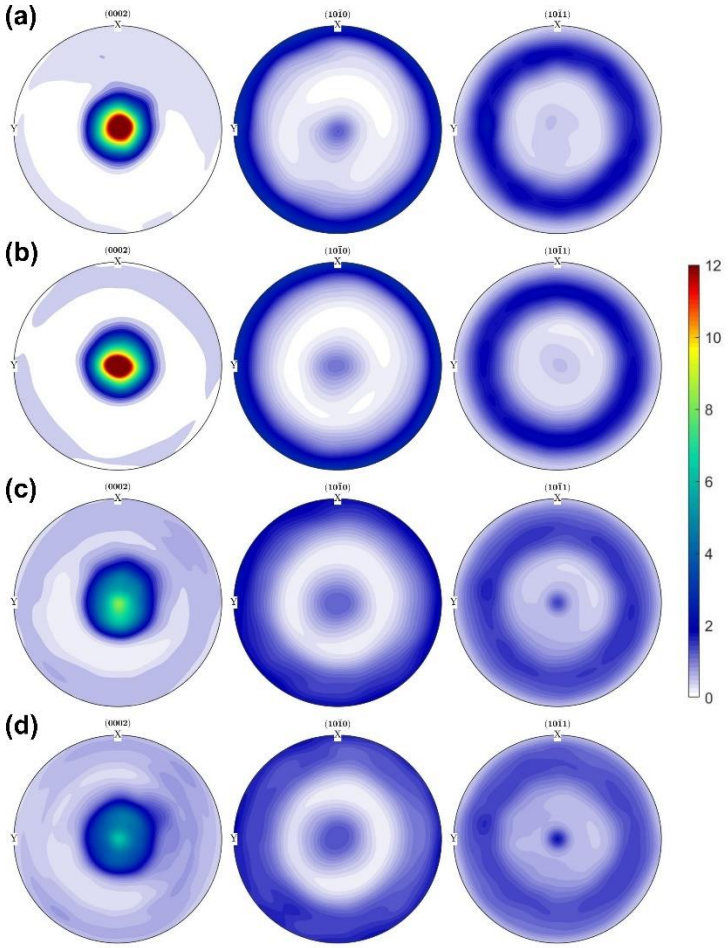


Figure 2.2. (0002), (10-10), (10-11) pole figures showing the initial texture of (a) Mg-0.2Y, (b) Mg-0.6Y, (c) Mg-1Y and (d) Mg-3Y samples. In each pole figure, X denotes rolling direction (RD), and Y denotes traverse direction (TD).

### 2.3.2. Mechanical testing

Compression tests were performed with an Instron 8801 servohydraulic universal testing platform. The Mg-Y alloys were sectioned into 4 x 4 x 6 (ND x TD x RD) mm cubes using wire cut electrical discharging machining to avoid significant damage to the material induced by cutting. The samples were compressed along RD with a strain rate of $10^{-3}$ $s^{-1}$ in a quasi-static manner for all compression tests discussed. To deform the samples to different strain level, a critical compressive strain was set to stop the compression test at the desired strain along RD.

For Mg-3Y, six samples were deformed to the true strain of 1.5%, 3.0%, 5.0%, 7.0%, 9.0% and 11.0%, respectively, to investigate the twin evolution in Mg-3Y. For the other three compositions, only one sample for each composition was deformed until an intermediate true strain level, 5.0% to show the effect of Y concentration on the twin evolution.

### 2.3.3. Microstructural characterization

The as-deformed sample was mechanically polished down to 0.05 μm using colloidal silica in ethylene glycol. Then chemical etching was performed using an etchant comprised of 10% nitric acid, 20% hydrochloric acid and 70% ethanol by volume, to remove the surface layer associated with polishing-induced residual stress, for better electron backscatter pattern quality.

EBSD was performed in a Tescan GAIA3 field emission scanning electron microscope equipped with an Oxford AztecHKL NordlysMax2 integrated EBSD system. EBSD was performed on the RD x ND plane. EBSD maps were acquired from six 500 x 500 μm regions for each Mg-Y alloy, with the step size being 1 μm to meet the balance of scanning time and resolution. The regions for EBSD scanning were randomly selected while keeping them distributed over the entire sample surface and not in the proximity of each other.

### 2.3.4. Statistical analysis

After the data acquisition by EBSD, the software METIS was applied to realize the twin statistics. METIS can execute an automatic detection of twin relationship in the EBSD data of hcp materials and output an SQL database which contains the quantified crystallographic information, especially twin-related parameters. The software also allows manual edit to correct any mislabeled twin relationship. Interested readers are referred to reference [52] for more details

regarding METIS. The statistical analysis was accomplished using MATLAB based on the data extracted from the SQL database.

## 2.4. Results

### 2.4.1. Stress-strain curves

Figure 2.3 shows the true compressive stress-strain curves collected for Mg-3Y at various strain levels and for all Mg-Y alloys to 5.0% compressive strain. Figure 2.3(a) demonstrates that stress-strain curves of Mg-3Y deformed to six compressive strain levels are in good agreement with each other. Figure 2.3(b) compares the true stress-strain curves of Mg-0.2Y, Mg-0.6Y, Mg-1Y and Mg-3Y for the 5.0% RD compression test. The hardening rule is slightly different among the four compositions of Mg-Y alloys – the yield stress and the hardening rate in the plastic regime increases marginally with Y concentration.

Although the relationship between total strain and twin evolution is often discussed in the literature, plastic strain represents the portion which a deformation twin would accommodate. By assuming that the elastic constant does not change during hardening, the total strain for each sample can be further decomposed into elastic strain and plastic strain by visually extending the linear elastic portion of the true stress-strain curve to the ending stress level, as illustrated in Figure 2.3(a). The value of plastic strain, along with actual total strain, is shown in Tables 2.2 and 2.3. Hereinafter, the nominal total strain will be used to denote each sample, while the plastic strain will be mentioned if plastic deformation is discussed.

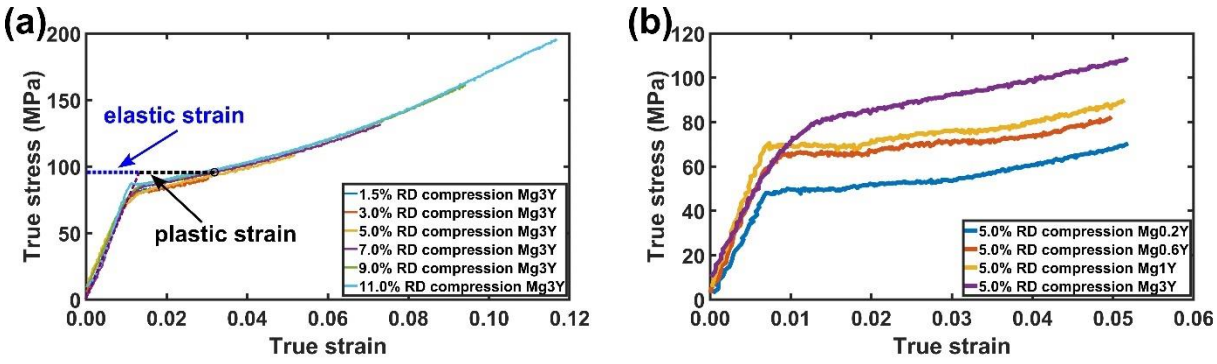


Figure 2.3. (a) True stress-true strain curves of six Mg-3Y samples deformed until each of six strain levels with the definitions of elastic strain and plastic strain labeled; (b) True stress-true strain curves of Mg-0.2Y, Mg-0.6Y, Mg-1Y and Mg-3Y deformed until 5.0% compressive strain.

Table 2.2. The total strain levels and plastic strain levels for each RD compressed Mg-3Y sample.

| Nominal strain | 1.5% | 3.0% | 5.0% | 7.0% | 9.0% | 11.0% |
|---|---|---|---|---|---|---|
| Actual strain | 1.7% | 3.1% | 5.2% | 7.3% | 9.4% | 11.7% |
| Plastic strain | 0.6% | 1.8% | 3.8% | 5.6% | 7.3% | 9.1% |

Table 2.3. The total strain levels and plastic strain levels for 5.0% (nominal strain) RD compressed Mg-Y alloys.

| Sample | Mg-0.2Y | Mg-0.6Y | Mg-1Y | Mg-3Y |
|---|---|---|---|---|
| Actual strain | 5.2% | 5.0% | 5.1% | 5.2% |
| Plastic strain | 4.2% | 4.0% | 4.2% | 3.8% |

### 2.4.2. EBSD characterization

Figure 2.4 illustrates a series of EBSD inverse pole figure (IPF)-Y colored maps for all Mg-3Y samples strained to 1.5%, 3.0%, 5.0%, 7.0%, 9.0% and 11.0%. In the EBSD micrographs for slightly strained samples (e.g., 1.5% and 3.0% true strain in Figures 2.4(a) and 2.4(b), most of the deformation twins appear with a lenticular morphology. While the amount of deformation twins is limited, the deformation twins are not randomly distributed in the sample, instead there

are a few subregions that exhibit preferential twin nucleation and growth. In those subregions with more twins, twin-twin transmission between neighboring grains is observed frequently due to the locally relaxed shear-induced backstress at grain boundaries, which has been reported elsewhere [23,74]. It is also observed that there are usually either zero or multiple twins in a grain. In a grain with multiple twins, the lenticular-shaped twins usually propagate along the same or a nearly perpendicular direction. This indicates these twins are either of the same twin variant (mutually parallel) or of co-zone twin variant pairs (mutually perpendicular).

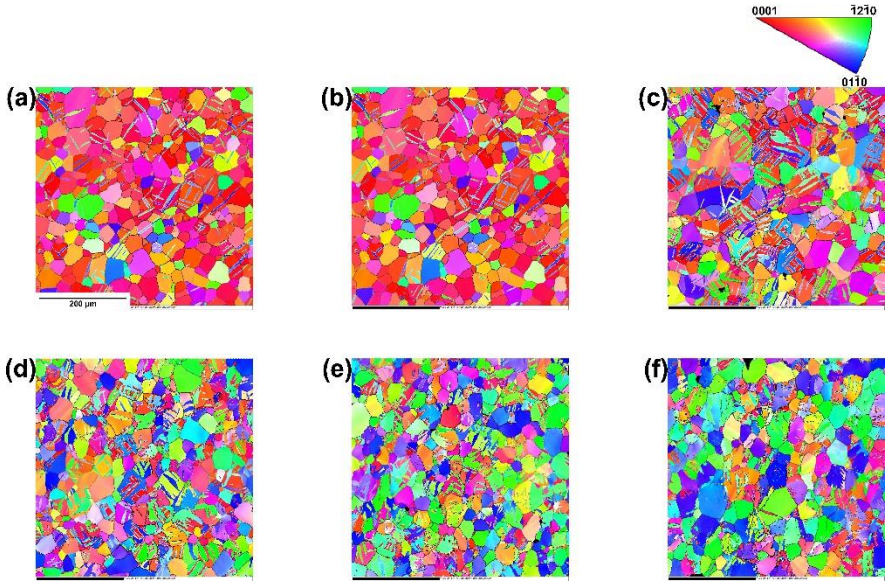


Figure 2.4. EBSD IPF-Y micrographs for Mg-3Y compressed along RD to (a) 1.5%; (b) 3.0%; (c) 5.0%; (d) 7.0%; (e) 9.0% and (f) 11.0%, colored coded to represent the crystal axis along ND (the legend is shown on the top of (c)). TD is perpendicular to the scanned plane, while RD and ND are along the horizontal and the vertical direction of the EBSD micrographs, respectively.

Within the mid-strain range (e.g., 5.0% and 7.0% true strain in Figures 2.4(c) and 2.4(d)), the main morphological change for twins associated with twin-twin intersections is that lenticular-shaped deformation twins merge (for twins with the same or mutually co-zone variants) or combine (for mutually non-co-zone twin variants) together to form complex morphologies that

are confined by grain boundaries or by twin-twin boundaries (TTBs). Three different types of twin-twin interactions are possible: (1) twin-twin intersections between the same twin variant lead to merged lenticular shaped twins, without the formation of TTBs; (2) those between the non-co-zone twin variant pairs form a TTB with a misorientation of ~60°, similar to that of the $\{10\bar{1}1\}$ twin boundary whose ideal misorientation angle is 56° in Mg; (3) those between the co-zone twin variant pair, however, don't necessarily have a detectable TTB because their theoretical misorientation is merely ~7°.

In the EBSD micrographs for heavily strained samples (e.g., 9.0% and 11.0% true strain in Figures 2.4(e) and 2.4(f)), the propagation, growth and intersections of the deformation twins greatly change the texture of the sample. Many grains in the heavily strained samples appear to be free of twins, but their grain orientation distributions sharply deviate from the texture of the starting material, indicating those grains might have been fully reoriented by the deformation twins. Because it is sometimes hard to identify twin boundaries and therefore twinning relationships, some of the statistics discussed hereinafter may not contain the data from the Mg-3Y sample strained to 11.0%.

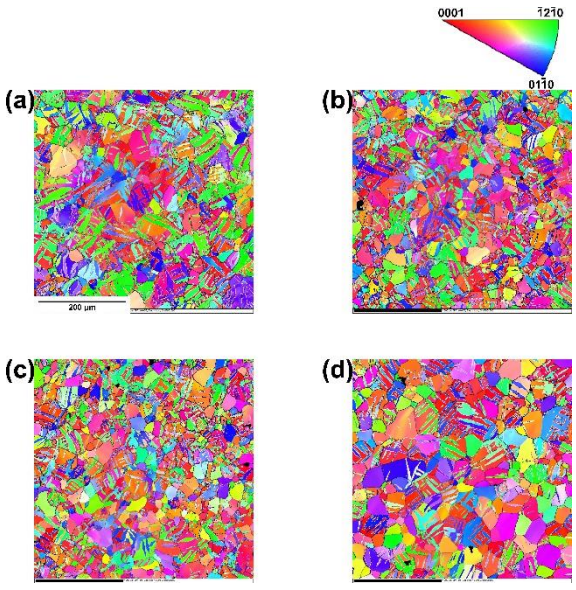

Figure 2.5. EBSD IPF-Y micrographs for 5.0% RD compressed (a) Mg-0.2Y; (b) Mg-0.6Y; (c) Mg-1Y and (d) Mg3Y, colored coded to represent the crystal axis along ND (the legend is shown on the top of (b)).

Figure 2.5 shows another series of EBSD IPF-Y figures for 5.0% RD compressed Mg-0.2Y, Mg-0.6Y, Mg-1Y and Mg-3Y. The twin occupies fewer area as Y concentration is higher. The morphologies of deformation twins in 5.0% RD compressed Mg-0.2Y, Mg-0.6Y and Mg-1Y are similar to that in the RD compressed Mg-3Y with an applied strain larger than 5.0%.

### 2.4.3. Twin area fraction (TAF) statistics

Among all of the twin-related statistical parameters, the twin area fraction (TAF) is a key parameter that can be effectively used to describe twin evolution. It should be noted that the TAF is expected to represent the twin volume fraction (TVF) from a two-dimensional characterization of EBSD according to stereology [78]. Figure 2.6(a) and Table 2.4 shows the TAF evolution output by METIS and SQL database. To understand how the increasing trend of the TAF, a relative increasing rate is defined as $\frac{\Delta TAF}{\Delta\varepsilon_{pl}\cdot(1-TAF)}$ and given in Table 2.4, where $\frac{\Delta TAF}{\Delta\varepsilon_{pl}}$ is a differential quotient showing the average rate of change in TAF between the current and the previous strain. $(1-TAF)$ in the denominator denotes that this relative increasing rate is with respect to the region which is not the twin at the previous strain level. It turns out that $\frac{\Delta TAF}{\Delta\varepsilon_{pl}\cdot(1-TAF)}$ changes for different stages during the deformation – it is relatively lower during three stages: (1) below ~0.6% plastic strain when the plastic deformation onsets and the $\{10\bar{1}2\}$ twins just start to nucleate; (2) when the plastic strain is between ~3.8% and ~5.6% and the twins begin to intersect with each other; (3) when the plastic strain is above ~7.3% and the twins saturate plenty of grains.

In recent years, a few publications have contributed to building an analytical model for TVF evolution [70,79]. A model featuring the exponential decay of the area of the "untwinned" region has been reported by assuming the TVF increasing rate is proportional to the area of the "untwinned" region. In other words, under this assumption it is equally probable for twins to form in any "untwinned" area during an infinitesimal strain increment $\Delta\varepsilon \to 0$. This simple model matches well with the experimental results of TVF evolution in extruded Mg-3Al-0.3Mn compressed along or perpendicular to extrusion direction [70]. However, in this study of the TAF evolution of RD compressed Mg-3Y, the TAF increasing rate with respect to the "untwinned" region, or $\frac{\Delta TAF}{\Delta\varepsilon_{pl}\cdot(1-TAF)}$ in Table 2.4, cannot be considered constant, so the exponential decay rule does not hold true here. One of the reasons behind this discrepancy is that the as-rolled Mg alloys, including Mg-3Al-0.3Mn in Ref. [70] usually have a strong basal texture, but the texture of as-rolled Mg-Y alloys, however, is strongly weakened by Y, as seen in Figure 2.2(d). There is another texture component called "rare earth texture", which deviates from the basal pole by about 25° [5,80]. Grains within the texture component other than basal texture have different probability to twin due to the changed Schmid factor. Therefore, the "equal twinning probability" assumption may not be correct for Mg alloys with weak textures.

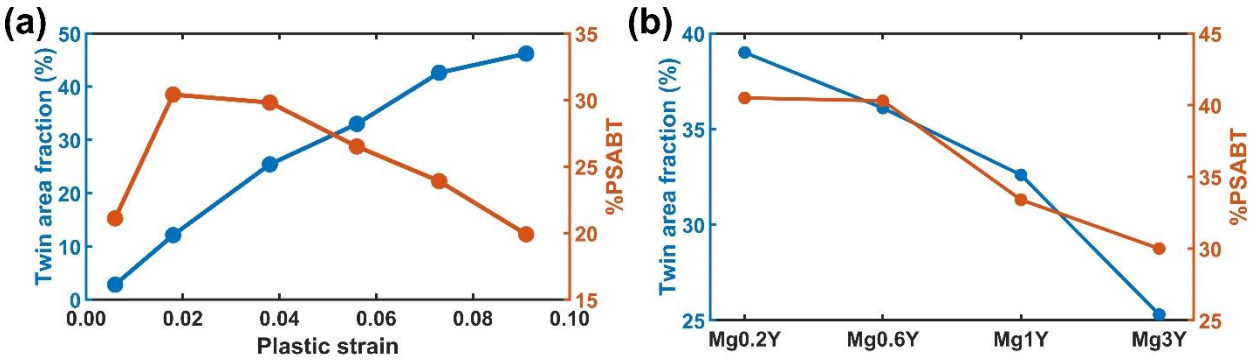


Figure 2.6. The TAF evolution (a) as a function of plastic strain and (b) as a function of Y concentration for all four Mg-Y alloys.

Table 2.4. TAF and %PSABT for RD compressed Mg-3Y at six different strain levels.

| Nominal strain | 1.5% | 3.0% | 5.0% | 7.0% | 9.0% | 11.0% |
|---|---|---|---|---|---|---|
| Plastic strain | 0.6% | 1.8% | 3.8% | 5.6% | 7.3% | 9.1% |
| TAF | 2.8% | 12.1% | 25.4% | 33.0% | 42.6% | 46.2% |
| $\Delta\mathrm{TAF}/\Delta\varepsilon_{\mathrm{pl}}$ | 4.67 | 7.75 | 6.65 | 4.22 | 5.65 | 2.00 |
| $\Delta\mathrm{TAF}/\Delta\varepsilon_{\mathrm{pl}} \cdot (1-\mathrm{TAF})$ | 4.67 | 7.97 | 7.57 | 5.66 | 8.43 | 3.48 |
| %PSABT | 21.1% | 30.4% | 29.8% | 26.5% | 23.9% | 19.9% |

Here we define another value, plastic strain accommodated by twins (PSABT), which is also included in Table 2.4 and Figure 2.6(a). This parameter takes the plastic strain accommodation by $\{10\bar{1}2\}$ twins along the compression direction (i.e., RD in this study) into account, while the TAF is a summation of the twin area and is not necessarily mechanically meaningful. PSABT is calculated by the following method. The strain tensor induced by twinning in the local coordinate system of the $\{10\bar{1}2\}$ twin is first converted into the sample coordinate system. One can execute a weighted sum of the RD strain accommodated by each twin, using the area as the weight since it is assumed that the plastic strain accommodated by one twin is proportional to its area. Accordingly, the percentage of plastic strain accommodated by twin (%PSABT) is defined by normalizing PSABT by plastic strain of the sample. As the deformation continues, %PSABT will firstly increase to a constant value and then goes down as the strain exceeds ~7%. The trend indicates that: (1) there is a threshold plastic strain level before 1.8% at which the nucleation and propagation of the deformation twin is suppressed ; (2) between 1.8% and 3.8% plastic strain, a balance is shown between the $\{10\bar{1}2\}$ twin and other plastic deformation modes (e.g., dislocation slip) in accommodating the plastic strain; (3) after 5.6% plastic strain, the plastic strain accommodated by the $\{10\bar{1}2\}$ twin saturates as %PSABT drops almost linearly.

Combining the trends of TAF and %PSABT, it is found that the increase in the TAF does not necessarily mean another increase in the plastic strain accommodation.

Figure 2.6(b) gives the TAF of 5.0% RD compressed Mg-0.2Y, Mg-0.6Y, Mg-1Y and Mg-3Y. Both the TAF and %PSABT decrease monotonically with increasing Y concentration, which indicates the addition of Y would suppress deformation twinning as well as its capability to accommodate plastic strain. To accommodate the same amount of total strain, more dislocation slip is expected for Mg-Y alloys containing more Y.

### 2.4.4. The effect of grain size and grain boundary perimeter on twinning probability

Deformation twins are usually not homogeneously distributed in polycrystal Mg due to the variation of local microstructure, such as varied grain sizes. It has been broadly reported that larger grains will prefer the formation of twins in Mg and Mg alloys [23,81–83]. This effect may also be attributable to the longer grain boundary perimeter of larger grains.

To validate the grain size effect in Mg-Y alloys, Figure 2.7 illustrates the probability that the grain has at least one $\{10\bar{1}2\}$ twin as a function of grain size for Mg-3Y at the five different strain levels. It clearly shows the positive correlation between grain size and twinning probability, despite the difference in strain levels. When the true strain is larger than 5.0% (shown in Figure 2.7(c)), the twinning probability in each grain group does not further increase with the applied strain, indicating that the grains without twins at 5% true strain may not be able to generate twins even if the strain increases. Figure 2.8 shows the same positive correlation between grain size and twinning probability among the four Mg-Y alloys, while as a result of the lower activity of deformation twins in Mg-Y alloys with higher Y concentration, Mg-1Y and Mg-3Y show lower twinning probability for the same grain group. Comparing with the same

statistics performed in 3% TD compressed pure Mg [23], our results are in conflict with the reported zero correlation between grain size and the probability of observing at least one twin inside the grain. Though further studies are needed to reveal the reason behind this contradiction, it may show a significant difference between the twin evolution in pure Mg and Mg-Y alloys.

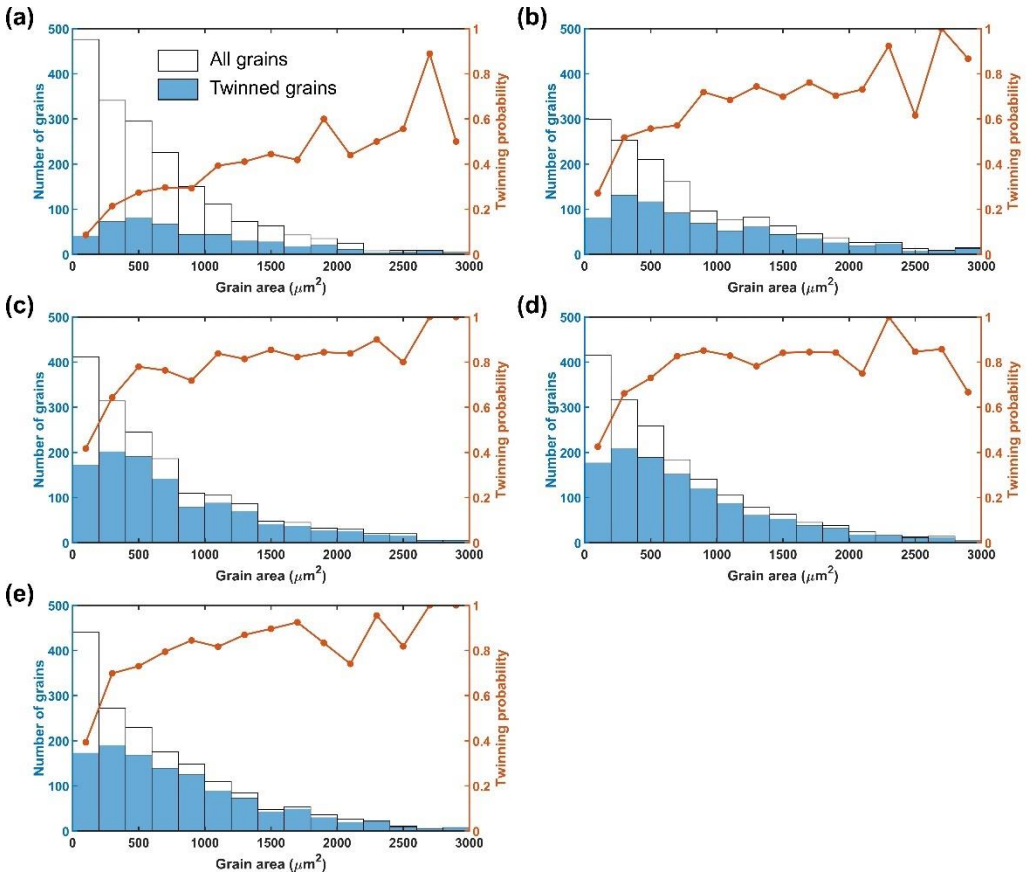


Figure 2.7. Total grain counts and twinned grain (i.e., grains that have at least one twin in it) counts as a function of the grain area in RD compressed Mg-3Y by a total strain of (a) 1.5%; (b) 3.0%; (c) 5.0%; (d) 7.0% and (e) 9.0%. Grains equal to or smaller than 20 μm$^2$ are discarded. The twin probability in grains within the grain area range of each rectangle in the histogram is illustrated by the line and symbols.

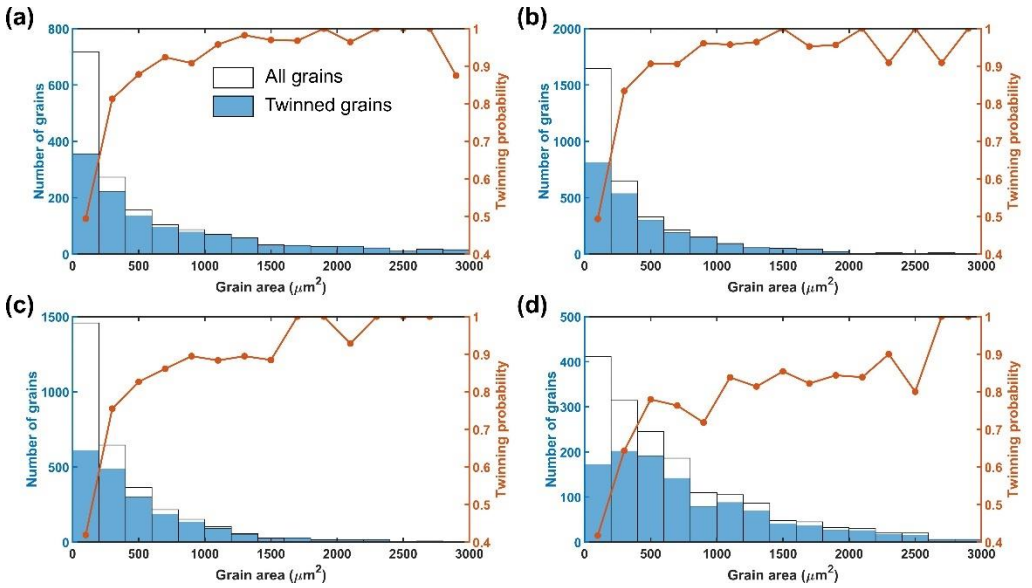


Figure 2.8. Total grain counts and twinned grain (i.e., grains that have at least one twin in it) counts as a function of the grain area in 5.0% RD compressed (a) Mg-0.2Y; (b) Mg-0.6Y; (c) Mg-1Y and (d) Mg-3Y. Grains equal to or smaller than 20 μm$^2$ are discarded. The twin probability in grains within the grain area range of each rectangle in the histogram is illustrated by the line and symbols.

Figures 2.9 and 2.10 illustrate the twinning probability as a function of grain boundary perimeter for Mg-3Y at the five different strain levels and among the four Mg-Y alloys, respectively. Interestingly, a better monotonicity is observed for the positive correlation between grain boundary perimeter and twinning probability, except for the perimeter range where data size is not large enough due to the sample microstructure (i.e., > 300 μm). This indicates that grain boundary perimeter may be a better parameter to determine the twinning probability, rather than grain size. This finding also agrees with the theory that stress concentration and the profuse pre-existing defects in the vicinity of grain boundaries boost twin nucleation and growth [84].

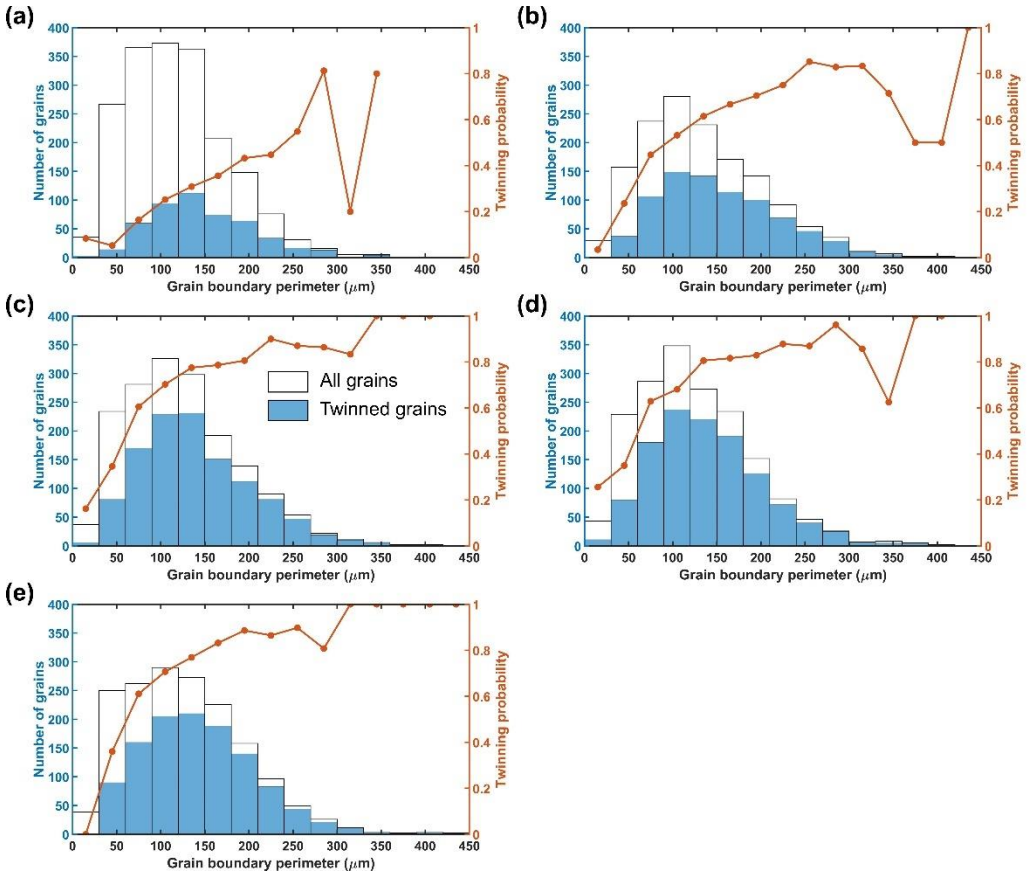


Figure 2.9. Total grain counts and twinned grain (i.e., grains that have at least one twin in it) counts as a function of grain boundary perimeter in RD compressed Mg-3Y by a total strain of (a) 1.5%; (b) 3.0%; (c) 5.0%; (d) 7.0% and (e) 9.0%. Grains equal to or smaller than 20 μm$^2$ are discarded. The twin probability in grains within the grain area range of each rectangle in the histogram is illustrated by the line and symbols.

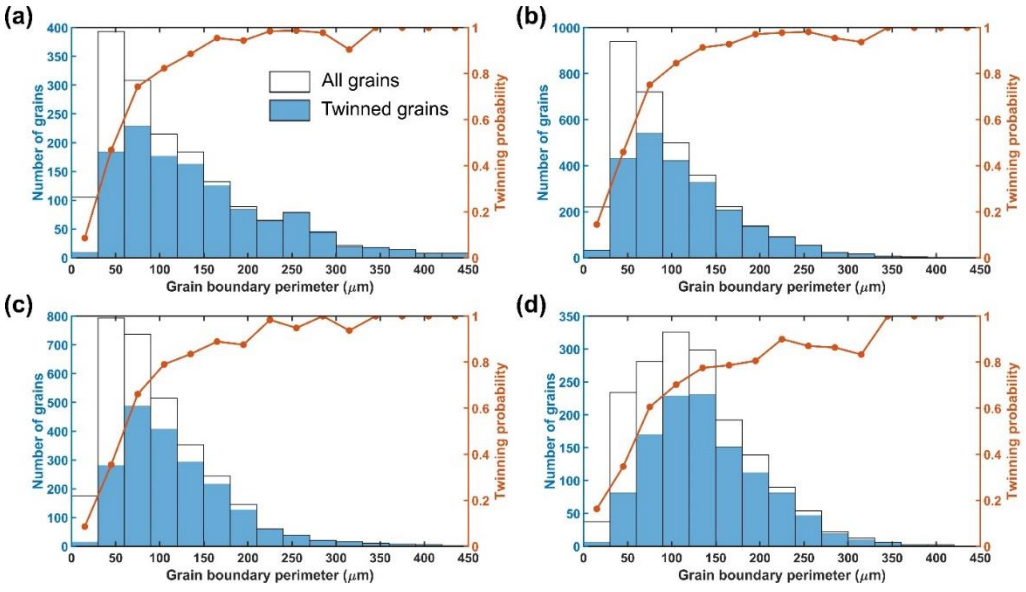

Figure 2.10. Total grain counts and twinned grain (i.e., grains that have at least one twin in it) counts as a function of grain boundary perimeter in 5.0% RD compressed (a) Mg-0.2Y; (b) Mg-0.6Y; (c) Mg-1Y and (d) Mg-3Y. Grains equal to or smaller than 20 $\mu m^2$ are discarded. The twin probability in grains within the grain area range of each rectangle in the histogram is illustrated by the line and symbols.

### 2.4.5. Double twinning area fraction

Double twinning is a phenomenon in which one or more secondary twins form inside a primary twin [45,46]. In the samples we studied, only one type of double twinning, $\{10\bar{1}1\}$-$\{10\bar{1}2\}$, is observed. Figures 2.11(a) and 2.11(b) show the $\{10\bar{1}1\}$-$\{10\bar{1}2\}$ secondary twin area fraction among the six strain levels of Mg-3Y and among the four Mg-Y alloys, respectively. An abrupt increase in the secondary twin area fraction is revealed after the total strain reaches 9.0%. In all four Mg-Y alloys, no significant variation of this fraction is shown. In summary, double twinning activity seems to be dictated by the strain level.

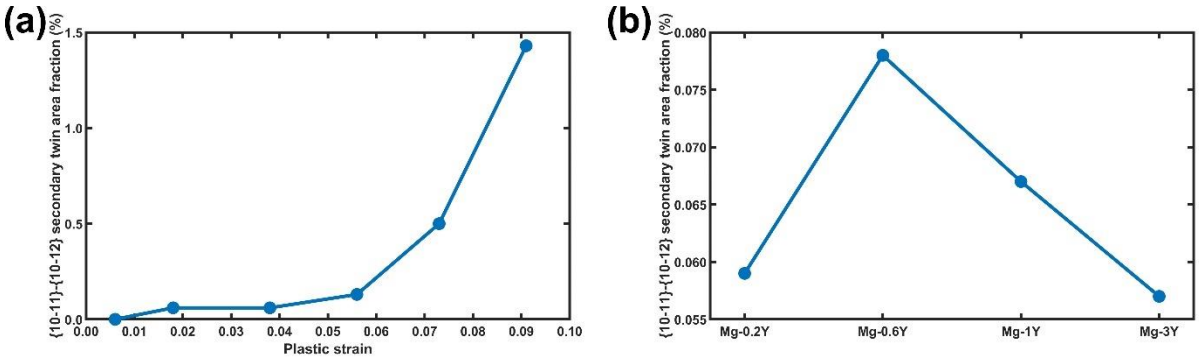


Figure 2.11. {10-11}-{10-12} secondary twin area fraction evolution (a) as a function of plastic strain and (b) as a function of Y concentration for all four Mg-Y alloys.

### 2.4.6. Twin boundary misorientation

Ideally, the misorientation of a coherent $\{10\bar{1}2\}$ twin boundary is approximately 86.3° $<11\bar{2}0>$. However, in practice, defects interacting with or in the vicinity of the twin boundary may lead to

the loss of coherency and therefore deviate the actual misorientation from the ideal value [85,86]. As a result, the deviation is a measure of how many defects are near the twin boundary. Figures 2.12 and 2.13 illustrate the misorientation angle deviation distribution as well as the mean deviation angle among the five strain levels of Mg-3Y and among the four Mg-Y alloys, respectively. Figure 2.12 shows a larger mean deviation as the compressive strain increases since the fraction of twin boundaries with a small deviation angle decreases. Figure 2.13 highlights a smaller misorientation deviation in Mg-3Y, while the similar mean deviation angles are observed in the other three Mg-Y alloys. This difference indicates that dislocation absorption and transmutation may be less active near the twin boundary in Mg-3Y.

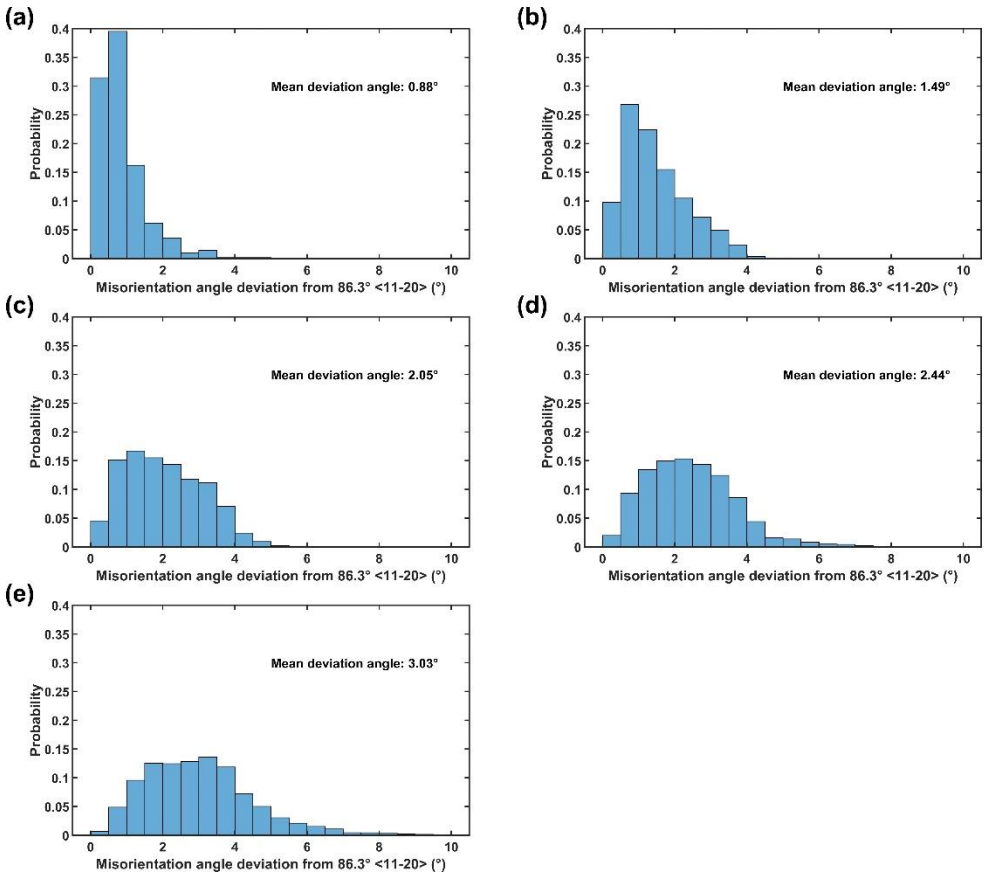


Figure 2.12. The angle deviation of {10-12} twin boundary misorientation from the ideal 86.3° <11-20> in RD compressed Mg-3Y by a total strain of (a) 1.5%; (b) 3.0%; (c) 5.0%; (d) 7.0%

and (e) 9.0%. Twin boundaries shorter than 10 μm are discarded. The average deviation angle is labeled in each subfigure.

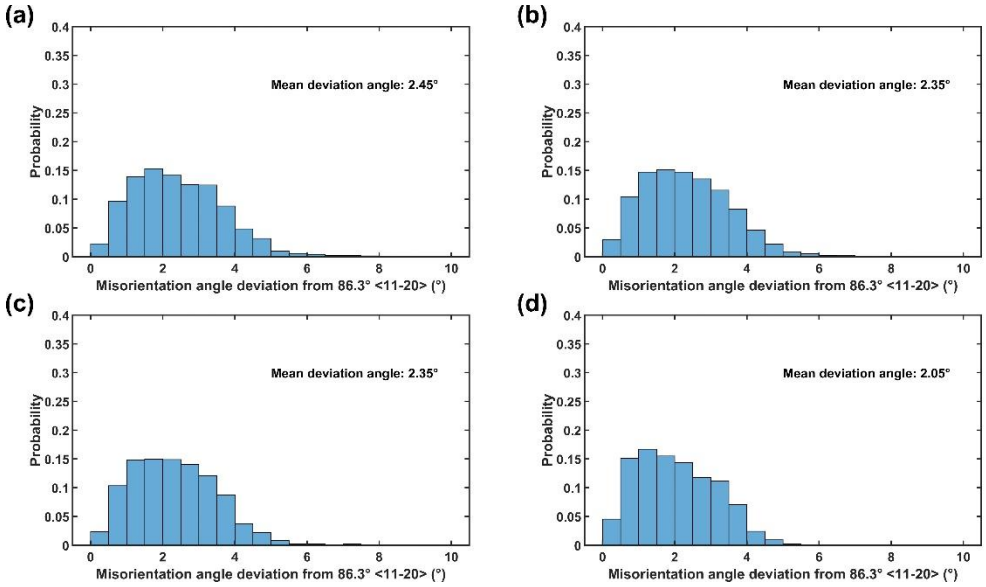


Figure 2.13. The angle deviation of {10-12} twin boundary misorientation from the ideal 86.3° <11-20> in 5.0% RD compressed (a) Mg-0.2Y; (b) Mg-0.6Y; (c) Mg-1Y and (d) Mg-3Y. Twin boundaries shorter than 10 μm are discarded. The average deviation angle is labeled in each subfigure.

### 2.4.7. Twin aspect ratio

The twin aspect ratio is a quantitative indicator of the twin morphology and is defined by METIS as the ratio between a twin's length and thickness. The length/thickness is estimated as four times the square root of the largest/smallest eigenvalue of the covariance matrix [52]. This covariance matrix gives the covariance between each coordinate (i.e., x and y coordinate) of pixels within the $\{10\bar{1}2\}$ twin. Figures 2.14 and 2.15 illustrate the aspect ratio distribution as well as the mean aspect ratio among the five strain levels of Mg-3Y and among the four Mg-Y alloys, respectively. The large aspect ratio at lower strain levels indicates that most $\{10\bar{1}2\}$ twins have a lenticular shape as shown by the EBSD micrographs. As deformation continues, twins

may grow along the other dimension (i.e., thicken) and therefore lower down the aspect ratio. On the other hand, still Mg-3Y is different from the perspective of the aspect ratio – its mean value appears to be larger and is indicative of slower twin thickening.

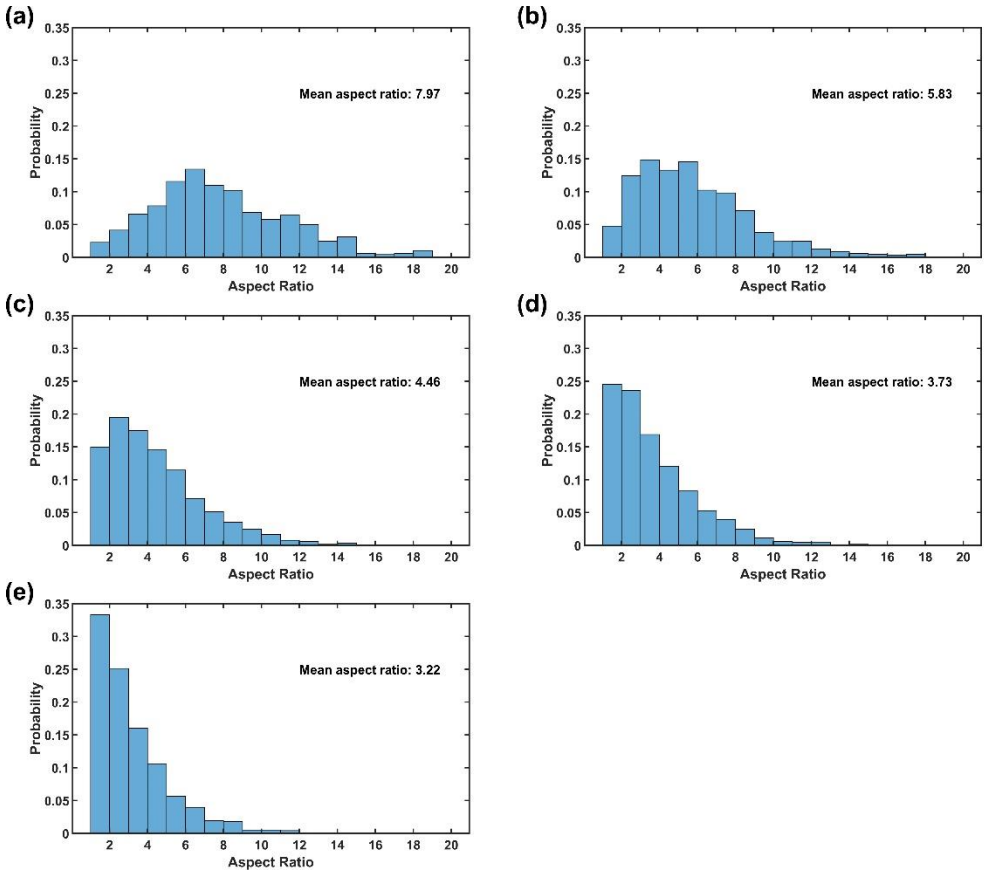


Figure 2.14. The aspect ratio of the observed {10-12} twins in RD compressed Mg-3Y by a total strain of (a) 1.5%; (b) 3.0%; (c) 5.0%; (d) 7.0% and (e) 9.0%. Twins equal to or smaller than 20 $\mu m^2$ are discarded because lengths and thicknesses are hard to estimate for these small twins. The average aspect ratio is labeled in each subfigure.

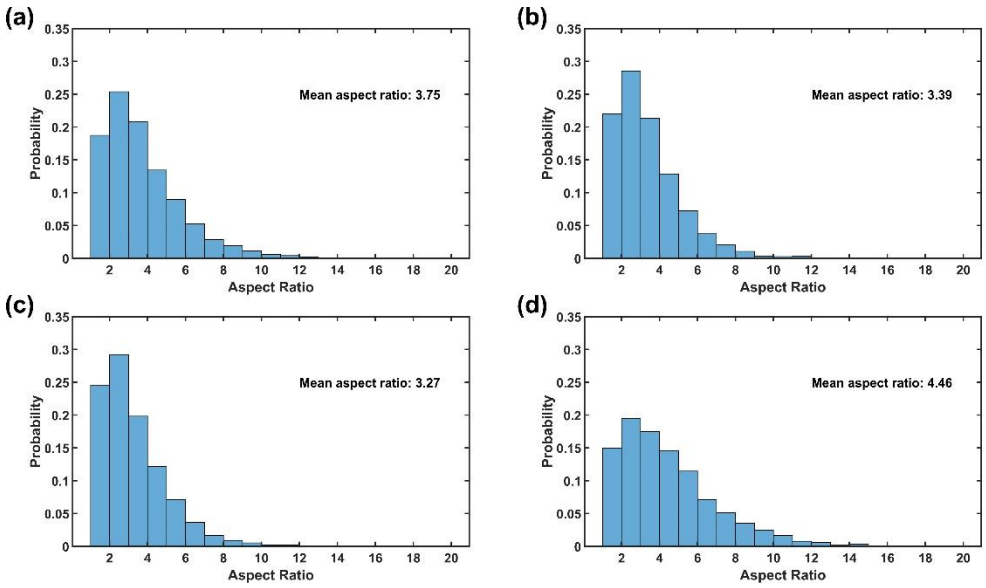


Figure 2.15. The aspect ratio of the observed {10-12} twins in 5.0% RD compressed (a) Mg-0.2Y; (b) Mg-0.6Y; (c) Mg-1Y and (d) Mg-3Y. Twins equal to or smaller than 20 $\mu m^2$ are discarded because lengths and thicknesses are hard to estimate for these small twins. The average aspect ratio is labeled in each subfigure.

## 2.5. Discussion

### 2.5.1. Schmid factor statistics

There are six Schmid factors for the $\{10\bar{1}2\}$ twin for each grain corresponding to the six twin variants. Though the Schmid factor is only geometrically calculated based on the crystallography and macroscopic loading direction, it is still an essential parameter in predicting whether the deformation twin will nucleate under polycrystal plasticity by transforming the full stress tensor into a shear stress along the twinning direction [24]. It is also efficient to convert the crystal orientation information, which must be described in three independent parameters, into a Schmid factor, which is a lower dimensional parameter.

It has been statistically shown that in polycrystal Mg the higher Schmid factor of a specific twinning system is, the larger the formation probability of that twinning system will be [23]. In

this study, we will re-validate this relationship. Figures 2.16 and 2.17 illustrate the fraction of Schmid factor ranking based on the variants of each observed $\{10\bar{1}2\}$ twin among the five strain levels of Mg-3Y and among the four Mg-Y alloys, respectively. While they validate that the twin variant with a larger Schmid factor is preferred, it also indicates that the Schmid factor is not deterministic in variant selection since twins that correspond to lower Schmid factor ranking (mainly 3$^{rd}$ and 4$^{th}$) are still possible to form for data acquired from all samples. Another feature of these figures is that the Schmid factor ranking can be categorized in three pairs, which are the largest and 2$^{nd}$, 3$^{rd}$ and 4$^{th}$, 5$^{th}$ and smallest. Roughly, the twin number fractions for the three pairs follow the ratio of 80%:20%:0%. The fraction difference within each pair is the most significant variation among all these figures – the difference is larger when the imposed strain increases regardless of Y concentration. It can be found that each pair mostly corresponds to co-zone twins due to geometrical relationships of co-zone twin pairs. Consequently, this feature results from the more deterministic co-zone variant selection under larger strain levels.

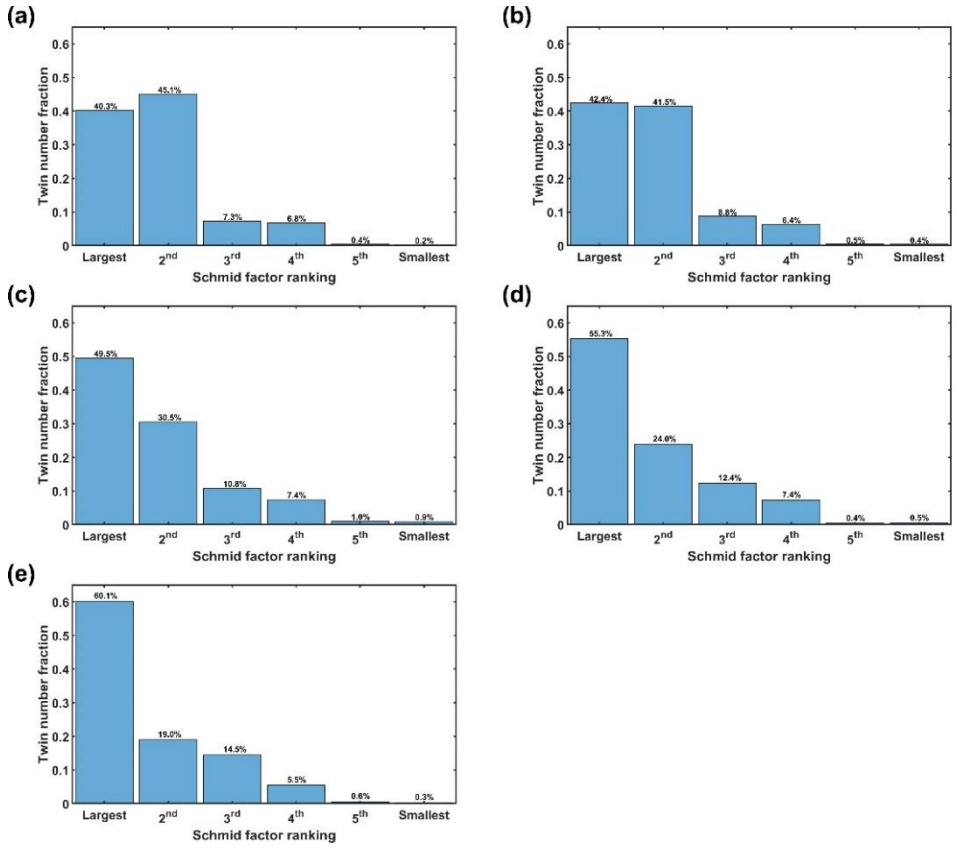


Figure 2.16. The {10-12} twin number fraction based on its Schmid factor ranking among all the possible six twin variants in RD compressed Mg-3Y by a total strain of (a) 1.5%; (b) 3.0%; (c) 5.0%; (d) 7.0% and (e) 9.0%. Twins that are inside grains equal to or smaller than 20 $\mu m^2$ are discarded for statistics.

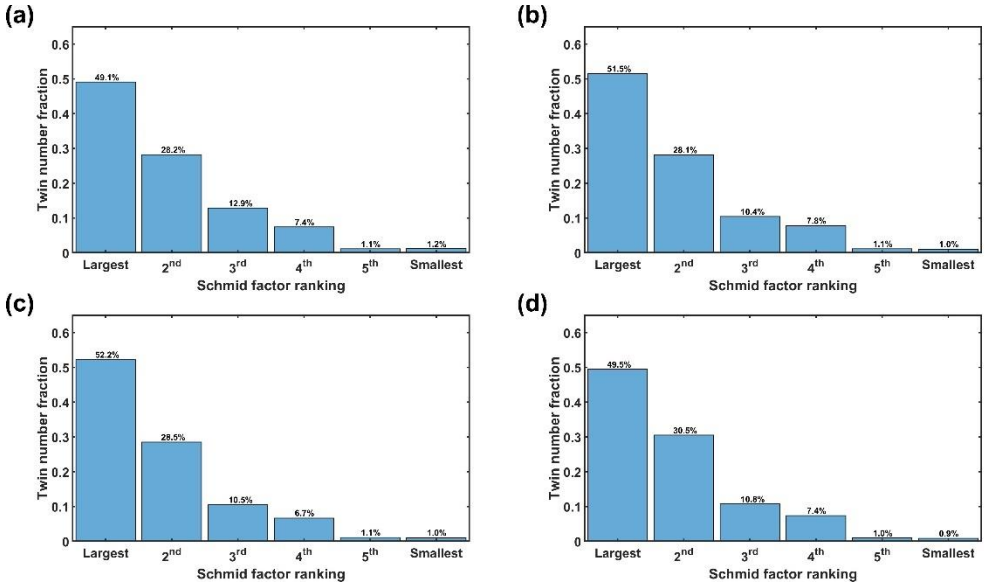

Figure 2.17. The {10-12} twin number fraction based on its Schmid factor ranking among all the possible six twin variants in 5.0% RD compressed (a) Mg-0.2Y; (b) Mg-0.6Y; (c) Mg-1Y and (d) Mg-3Y. Twins that are inside grains equal to or smaller than 20 $\mu m^2$ are discarded for statistics.

Figures 2.18 and 2.19 illustrate the Schmid factor values for each $\{10\bar{1}2\}$ twin among the five strain levels of Mg-3Y and among the four Mg-Y alloys, respectively. The Schmid factor value distribution looks more intuitive – at lower strain levels, generated $\{10\bar{1}2\}$ twins mostly have a large Schmid factor value (i.e., > 0.3) while at larger strain levels, those with a lower or even negative Schmid factor value may be possible to form. Similar to the trend shown in Figure 2.17, Y concentration does not significantly affect the Schmid factor value distribution.

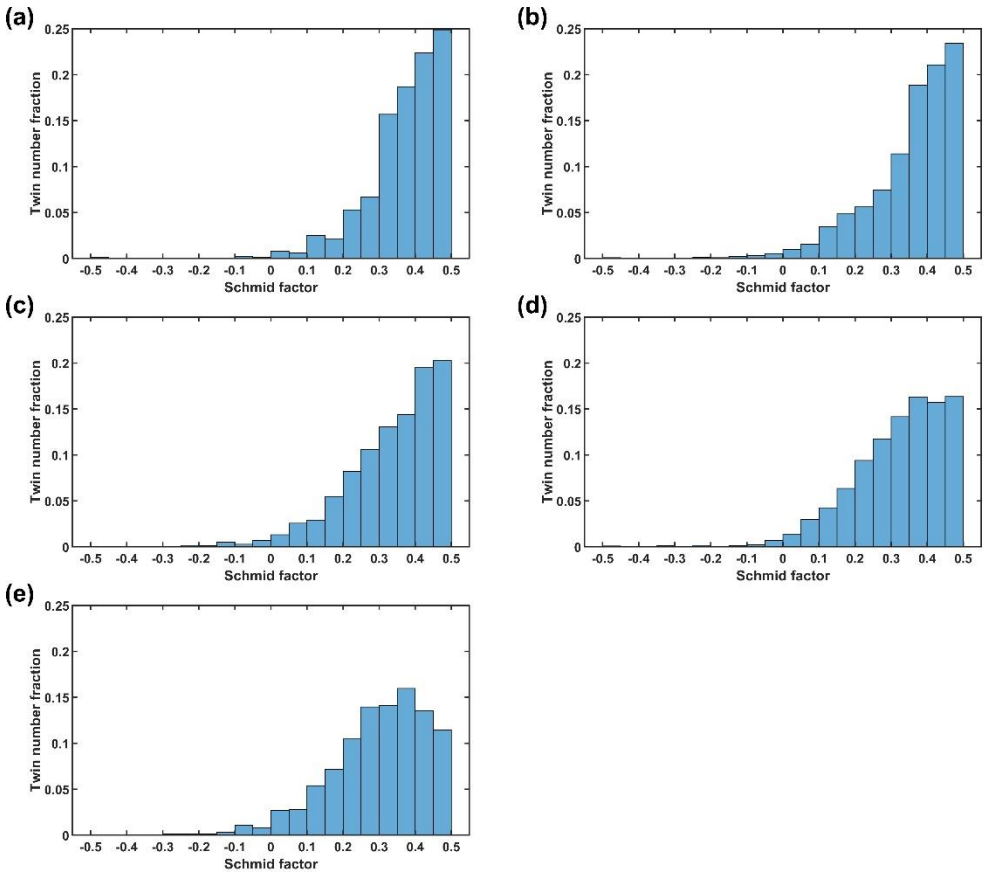


Figure 2.18. The Schmid factor distribution of the observed {10-12} twins in RD compressed Mg-3Y by a total strain of (a) 1.5%; (b) 3.0%; (c) 5.0%; (d) 7.0% and (e) 9.0%. Twins that are inside grains equal to or smaller than 20 $\mu m^2$ are discarded for statistics.

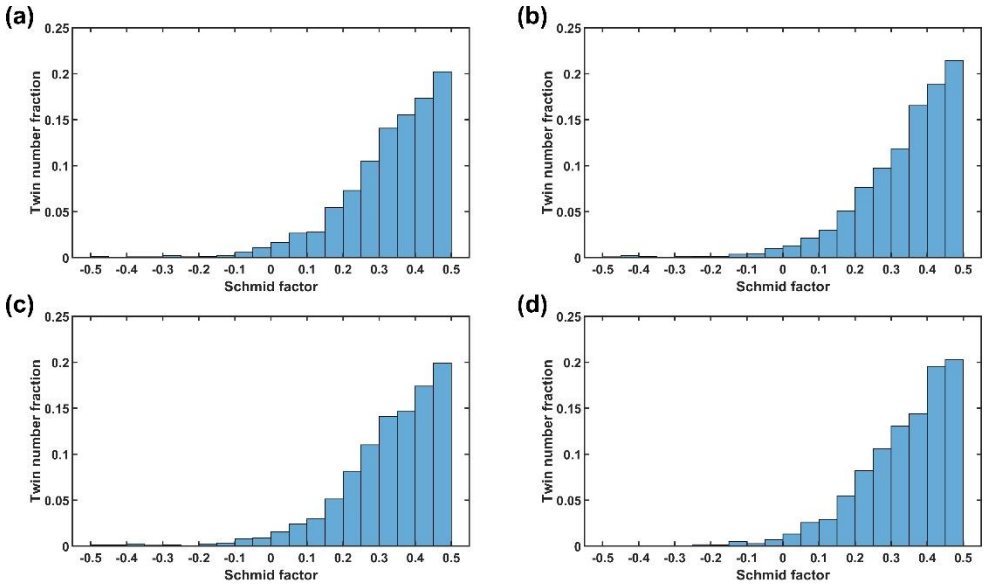


Figure 2.19. The Schmid factor distribution of the observed {10-12} twins in 5.0% RD compressed (a) Mg-0.2Y; (b) Mg-0.6Y; (c) Mg-1Y and (d) Mg-3Y. Twins that are inside grains equal to or smaller than 20 $\mu m^2$ are discarded for statistics.

### 2.5.2. Grain categorization by the Schmid factor

#### 2.5.2.1. For the Mg-Y alloys RD compressed by 5.0%

It is intuitive that different grains with different crystal orientation with respect to the loading direction do not behave in a similar manner upon deformation and therefore have a distinct twinning activity. Consequently, grain categorization can help deconvolute their relative impact on twinning. An effective grain categorization criterion is their maximum Schmid factors of $\{10\bar{1}2\}$ twin. Though the Schmid factor is a simplified description of the crystal orientation of grains with respect to the ease of $\{10\bar{1}2\}$ twin nucleation, it is still proven both by this work in section 2.5.1 and others [23,73] that a positive correlation holds between Schmid factor value and twin probability. In this study, the grains with a highest Schmid factor value larger than 0.1 are categorized into 4 groups, 0.1-0.2, 0.2-0.3, 0.3-0.4 and 0.4-0.5. Those with lower Schmid

factor values are left out since there may not be abundant amount of the $\{10\bar{1}2\}$ twins inside them to enable a reasonable statistical analysis. The categorization of all grains allows for an analysis of $\{10\bar{1}2\}$ twinning activity within each grain group and helps answer the question: which factor, the weakened basal texture or the hardening modulated by higher Y concentration, further lowers down the TAF in Mg-3Y?

Figure 2.20(a) illustrates the area fraction for grains from each group and shows that the weakened basal texture, or so-called rare earth texture is shown by a lower area fraction of grains with larger Schmid factors (i.e., > 0.3). Figure 2.20(b) shows the TAF evolution by each grain group among the four Mg-Y alloys. The TAF is significantly lower in Mg-3Y, regardless of the grain group. Comparing Mg-0.6Y with Mg-3Y (since they have similar grain sizes), the four grain groups in Figure 2.20(b) contribute almost 100% of the total TAF for both (35.7% out of 36.1% for Mg-0.6Y and 25.2% out of 25.6% for Mg-3Y). If supposing Mg-3Y have the same texture and therefore the same area fractions for each grain group as Mg-0.6Y, these four grain groups will have an aggregated TAF of 28.5% instead of 25.2%. On the other hand, if Mg-3Y has the TAF for each grain group as high as that of Mg-0.6Y, it will give an aggregated TAF of 31.7%.

A similar comparison can also be done between Mg-1Y and Mg-3Y. If we assume their textures are the same, these four grain groups in Mg-3Y will give an aggregated TAF of 25.1%, which is approximately equal to the original aggregated TAF for these four grain groups of Mg-3Y and indicates their textures are alike. The TAF difference is solely attributed to, again, the different hardening behavior resulted from the higher Y concentration in Mg-3Y, because if Mg-3Y has the group-by-group TAFs as high as that of Mg-1Y, the aggregated TAF for Mg-3Y will reach 32.8%. Clearly, while the two factors both play a role, the lower TAF for each grain group

induced by different hardening behavior and the higher Y concentration is more essential in determining the lower TAF inside Mg-3Y.

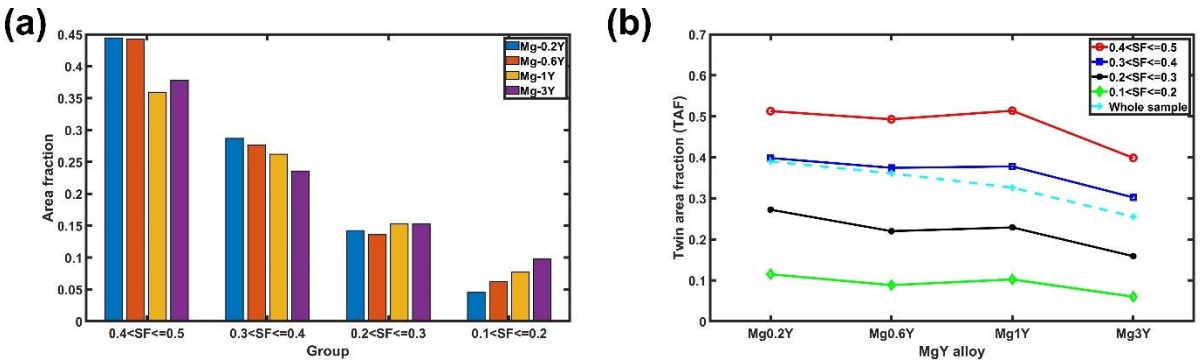


Figure 2.20. (a) The area fraction for each grain group categorized by the highest Schmid factor for {10-12} variants in that grain; (b) The group-by-group and the total TAF for all the four Mg-Y alloys. SF in the figure means Schmid factor.

### 2.5.2.2. For Mg-3Y RD compressed at six different strain levels

Following the same grain categorization strategy, we can also perform a similar analysis for Mg-3Y RD compressed at six different strain levels. Figure 2.6(a) and Table 2.4 have indicated that the TAF evolution cannot be described by a simple exponential decay model possibly due to the rare earth texture of Mg-3Y. Now the question to be answered becomes, if grains are categorized by a descriptor of twinning probability (e.g., the Schmid factor), whether it is possible to find out some correlations between the TAF in each group and the applied strain.

Figure 2.21(a) illustrates the area fraction for each grain group from Mg-3Y. Figure 2.21(b) follows with the TAF evolution by each group as well as the entire sample as a reference. Except for the grain group with the Schmid factor ranged from 0.4 to 0.5, the increase of the TAF appears to have two steps: after 7.0% true strain at which the twin-twin intersection becomes more frequent, the increasing rate is higher. The exception can be explained by the limitation of

EBSD characterization: Figure 2.21(a) shows a lower area fraction for the grain group with the Schmid factor ranged from 0.4 to 0.5, which reveals that the fully twinned grain fails the detection of grains and twins due to the disappearance of twin boundaries as the twin saturates the entire grain. Considering this artifact, the same two-step increasing trend should hold true for all grain groups. However, more data are needed to validate this two-step linear relationship. We argue that it is challenging to mathematically describe the TAF evolution for each group on the basis of a fundamental function.

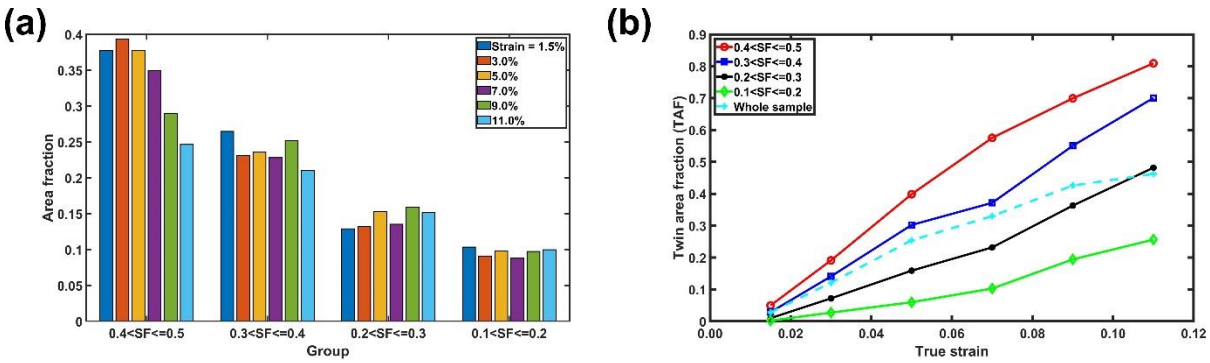


Figure 2.21. (a) The area fraction for each grain group categorized by the highest Schmid factor for {10-12} variants in that grain; (b) The group-by-group and the total TAF for RD compressed Mg-3Y at six different strain levels. SF in the figure means Schmid factor.

### 2.5.3. Twin-twin intersection analysis through TTB statistics

Before TTB statistics is discussed, 3 types of TTB in Mg are defined. As is shown in the inset of Figure 2.22(a), the six twin variants of $\{10\bar{1}2\}$ twin is labelled as $V_1$, $V_2$, …, $V_6$. The boundary between the oppositely aligned twin variant (e.g., $V_1$ and $V_4$) is defined as co-zone TTB; the boundary between the closest aligned twin variant (e.g., $V_1$ and $V_2$) is called $1^{st}$ type non-co-zone TTB; the boundary between the second closest aligned twin variant (e.g., $V_1$ and $V_3$) is defined as $2^{nd}$ type non-co-zone TTB. Again, the threshold misorientation angle to detect the type of the boundary is set to be 5°.

Figures 2.22(a) and 2.22(b) reveal the TTB length fraction among the six strain levels of Mg-3Y and among the four Mg-Y alloys, respectively. Generally, the twin-twin intersections begin to occur at an early stage of the deformation, indicated by the non-zero TTB length fraction for all data points. For Mg-3Y, it appears that the co-zone twin-twin intersection is only dominant at lower strain levels and the highest strain level, while the 1st type non-co-zone TTB is more profuse as the true strain increases before 11.0%. What is more, the two types of non-co-zone TTB are not equivalent, and the 1st type is always preferred. For each Mg-Y alloy strained to 5.0%, the TTB length fractions are quite similar, except for a significant fraction drop for the co-zone TTB of Mg-3Y. While the mechanism for this observation is not clear on the basis of statistical analysis, the low TAF and fewer twin-twin interactions in Mg-3Y are likely to be important factors.

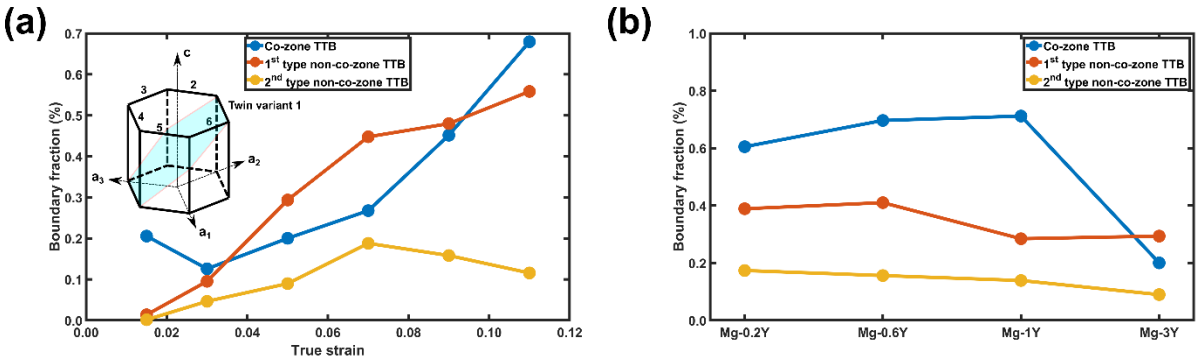


Figure 2.22. Boundary fractions by length for co-zone TTB, 1st type non co-zone TTB, and 2nd type non co-zone TTB in (a) RD compressed Mg-3Y at six strain levels and (b) four different 5% RD compressed Mg-Y alloys.

### 2.6. Conclusions

This chapter described a systematic statistical study of $\{10\bar{1}2\}$ twin behavior at the micrometer level using large datasets acquired by EBSD and processed by METIS. The effect of the compressive strain along RD and Y concentration on features like the twin area, the twin count,

twin morphology, and grain size dependency of twinning probability etc., have been examined. Key conclusions are summarized as below:

1. The TAF evolution follows a more complicated multi-step trend rather than the model describing the evolution of the "untwinned" area fraction using exponential decay in heavily textured Mg alloys.

2. The indicator %PSABT shows that the $\{10\bar{1}2\}$ deformation twins are the most active in accommodating the plastic strain within the plastic strain range from ~2% to ~4%, before profuse twin-twin interactions happen.

3. The positive correlation between grain size and the probability of observing at least one twin in the grain holds for all strain levels of Mg-3Y and all Mg-Y alloys studied. On the other hand, grain boundary perimeter appears to be a better predictor for this twinning probability.

4. Both twin aspect ratio and twin boundary misorientation statistics reveal that twin thickening and dislocation absorption at twin boundaries occur slower in Mg-3Y, because of a lower TAF and relatively sluggish twin growth.

5. The twinning prediction and the twin variant selection based on the Schmid factor are reasonable but not absolutely correct. For the twinning prediction, most generated $\{10\bar{1}2\}$ twins have a large Schmid factor value, but it is still possible for the twins with lower Schmid factor values to form, especially at higher strain levels. For the twin variant selection, it is found that approximately the twin number fraction for the three twin variant pairs containing the two mutually co-zone variants with largest Schmid factor values, with the 3$^{rd}$ and 4$^{th}$ largest Schmid factor values and with the lowest Schmid factor values, respectively, follow the ratio of

80%:20%:0%. As the applied strain increases, the twin variant with a larger Schmid factor in the co-zone twin pair will be preferable.

6. The grain categorization by the Schmid factor reveals that the higher Y concentration plays a more important role in determining the lower TAF inside Mg-3Y than the weakened texture.

7. A preliminary twin-twin intersection analysis through TTB statistics shows the higher frequency of the co-zone and the 1$^{st}$ type non-co-zone twin-twin intersections in Mg-3Y.

8. EBSD is potentially a promising data source to execute high-throughput statistical studies that requires a substantial size of the dataset.

As an outlook for future work, it will be interesting to apply other statistical analysis tools, such as machine learning to build a multiple-to-one correlation that enables a direct prediction of whether a given grain with known characteristics (e.g., grain size, misorientations of grain boundaries, etc.,) will be favorable for twin nucleation. Also, for the many correlations established in this work, it will also be necessary to identify the mechanisms responsible using other theoretical and characterization methods, such as stress-field simulations.

# Chapter 3: Room Temperature Deformation-induced Solute Segregation and its Impact on Twin Boundary Mobility in a Mg-Y Alloy

## 3.1. Abstract

The mechanical behavior of alloys is influenced by segregation of solute atoms, which affects deformation mechanisms, such as slip and twinning. In this study, we report on an atomic-scale investigation into room temperature, deformation-induced solute segregation in a Mg-Y alloy. High concentrations of Y were observed at the dislocation cores. In addition, we found that $\{10\bar{1}2\}$ twins were bounded by coherent twin boundaries and basal-prismatic facets, which contained periodic segregation of Y-rich columns and nano-sized Y-rich clusters, respectively. The observed segregation arrangement was energetically attributed to the fact that it minimizes the overall lattice distortion and is kinetically assisted by the dynamic interaction between solute atoms and crystallographic defects and the slip-twin interaction during plastic deformation. Moreover, segregated Y atoms exert a pinning effect and lead to anisotropy on the mobility of twin boundaries. This finding offers a potentially new alloy design path to control the mechanical response of Mg alloys

## 3.2. Introduction

The discovery of new materials to meet the ever-changing industrial demands is often achieved through alloying. In the past few decades, this effort has been extensively applied to Mg, which holds significant potential for lightweight structural applications. Because of its hexagonal close

packed crystal structure, Mg has inherent plastic anisotropy, typically leading to insufficient room temperature formability. The active slip modes in Mg are largely confined to its close-packed basal planes, without easy slip systems to accommodate deformation in the *c*-direction [77,87–91]. $\{10\bar{1}2\}$ twinning can be activated to accommodate strain along *c*-axis tension, making it an important deformation mechanism in Mg in addition to dislocation slip [92–94]. It has been well documented that the addition of alloying elements, particularly dilute concentrations of rare earth elements, such as Y [95–99] or Ce [100,101], can dramatically weaken the crystallographic texture and simultaneously improve the formability and strength of Mg. Such an effect has been attributed to the influence of solute atoms on the flow stresses and relative activities of different slip and twinning modes. Elucidating the fundamental mechanisms by which alloying elements affect slip and twinning is critical for the design of new advanced Mg alloys.

One important question concerns the spatial distribution of alloying elements. Most studies modeling solute strengthening in Mg include assumptions that the alloying addition stay in solution and are randomly distributed in dilute alloys without considering the potential for rearrangement during plastic deformation [102–104], although the diffusion of solute atoms to the elastic strain field of dislocations, a phenomenon known as strain aging, has been reported in a wide range of material systems [105–107]. Besides dislocations, high-angle annular dark-field scanning transmission electron microscopy (HAADF-STEM) results have demonstrated that solute atoms, e.g., Gd, Ag, Zn and Al, can segregate on coherent twin boundaries (CTBs) in Mg alloys after annealing [20,21,108–110]. Such segregation increases the thermal stability and hinders the motion of CTBs [20,21]. However, compared to solute segregation observed after annealing, deformation-induced TB segregation at room temperature [35] and its impact on the mechanical

behavior and microstructural evolution of Mg alloys have not been explored. Moreover, both experimental [111–113] and simulation [35,37,112–115] studies have demonstrated the potential importance of basal-prismatic (BP) facets on $\{10\bar{1}2\}$ twin boundaries (TBs) during twin growth; however, segregation of solute atoms to such facets and its impact on the energetics associated with $\{10\bar{1}2\}$ TB migration have not been investigated. To address this lack of understanding, we report on the segregation of solute atoms to dislocations and faceted $\{10\bar{1}2\}$ TBs, composed of CTBs and BP facets, in a Mg-Y binary alloy that has been deformed at room temperature without subsequent annealing. High-resolution STEM and atomistic modeling were combined to investigate the distribution and pinning effects of segregated Y atoms, shedding light on a mechanism by which alloying affect the subsequent mechanical behavior of Mg.

### 3.3. Experimental Methods

The starting material is a pre-rolled and fully recrystallized single-phase Mg-3 wt.% Y (Mg-3Y) alloy, provided by Helmholtz-Zentrum Geetchacht, Germany. The alloys were cast with high-purity Mg and pure Y, as described in previous studies using similar materials [116,117]. The sample was sectioned into 4×4×6 mm cuboids and quasi-statically compressed at room temperature along the rolling direction (RD) to ~2% plastic strain. Energy dispersive X-ray spectroscopy (EDS) and electron backscattered diffraction (EBSD) were performed using a Tescan GAIA3 scanning electron microscope, equipped with an Oxford Aztec Energy Advanced EDS System and an AztecHKL NordlysMax2 EBSD system. EDS of the starting material (Figure 3.1(a)) estimates the weight percent of Y is approximately 3 wt.%, which is consistent with its nominal composition. EBSD maps show the starting material (Figure 3.2(a)) has equiaxed grains

with an average size of ~26 μm and is free of twins, while profuse newly formed lenticular-shaped $\{10\bar{1}2\}$ twins were observed after compression (Figure 3.2(b)), with a twin area fraction of ~9.2%. To prepare specimens for STEM observation, the compressed Mg-3Y was sectioned parallel to the RD, mechanically polished and chemically etched by a nital solution. The thin foils were ion milled to electron transparency at cryogenic temperature. A double aberration-corrected JEOL JEM-ARM300F TEM operated at 300 kV was used for microstructure and chemical analyses. For HAADF-STEM imaging, a 35-pA probe current and 6-cm camera length were used, with the inner and outer collection angles being 106 and 180 mrad, respectively.

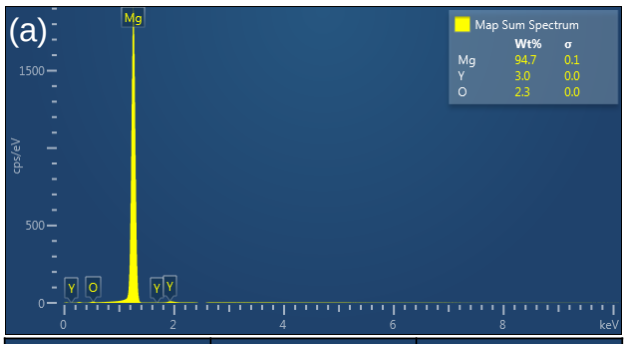


| Element | Line type | Weight% |
|---|---|---|
| Mg | K series | 94.72 |
| Y | L series | 2.96 |
| O | K series | 2.31 |
| Total | | 100.00 |

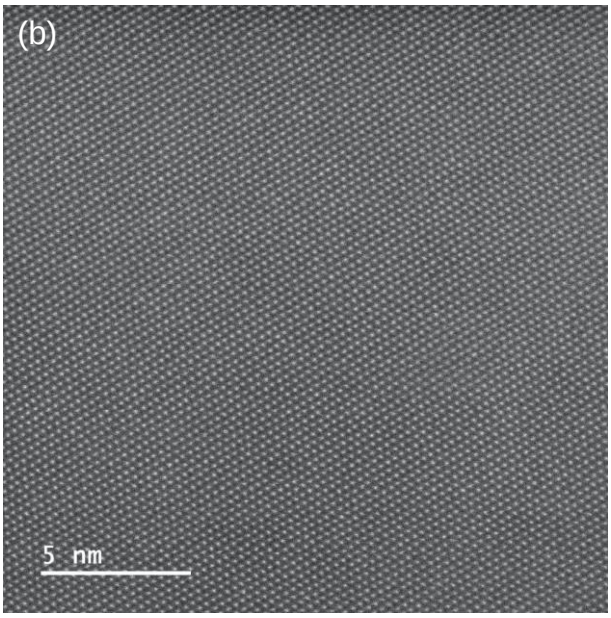


Figure 3.1. (a) SEM EDS spectrum of Mg-3Y and the calculated weight percent quantification results. (b) HAADF-STEM of undeformed Mg-3Y, showing no Y-rich clusters before deformation.

### 3.4. Results and Discussion

Figure 3.1(b) shows a representative HAADF-STEM image of the undeformed Mg-3Y sample. No Y-rich nanoclusters exist in the starting material. Figure 3.2(c) shows an annular dark field (ADF)-STEM image of a representative TB in the deformed Mg-3Y. The inset in the figure is the

corresponding fast Fourier transform image showing the $\{10\bar{1}2\}$ twin-matrix orientation relationship. The STEM-EDS map using K lines signals of Mg and Y (Figure 3.2(d)) for the same region as Figure 3.2(c) shows the enrichment of Y along the $\{10\bar{1}2\}$ TB.

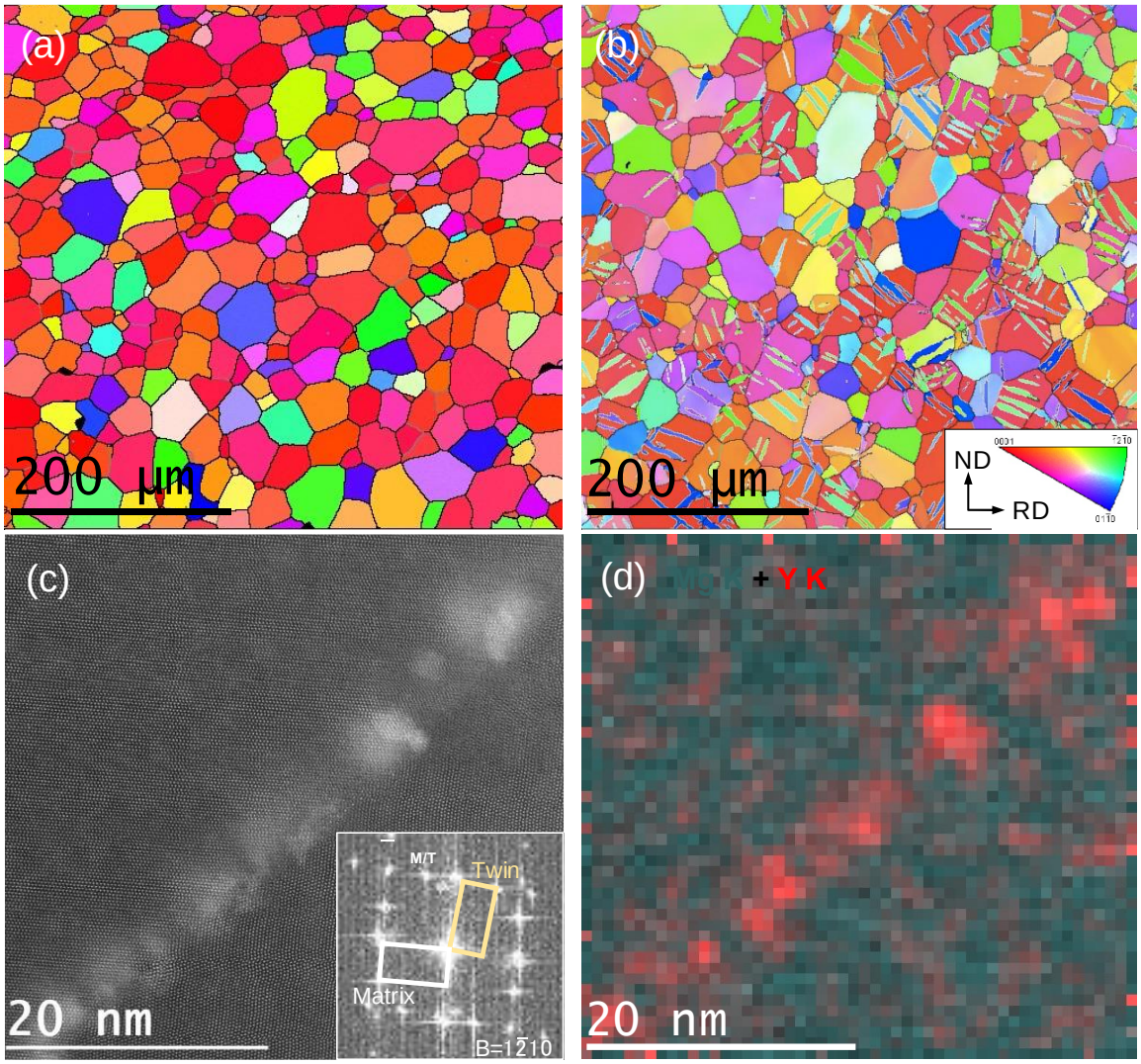


Figure 3.2. Grain orientation maps of the Mg-3Y sample (a) before compression and (b) after ~2% plastic compressive strain, at room temperature, along the rolling direction. (c) ADF-STEM image of a {10-12} twin boundary. Inset is the corresponding fast Fourier transform image showing the {10-12} twin-matrix orientation relationship. (d) STEM-EDS of the same region as (a) showing the segregation of Y at the twin boundary.

Atomic-resolution HAADF-STEM images in Figure 3.3 show the detailed microstructure of deformation-induced Y segregation in Mg-3Y at dislocations and along $\{10\bar{1}2\}$ TBs. Figure 3.3(a) along a $<1\bar{2}10>$ zone axis shows a low-angle tilt boundary formed by an array of dislocations. The Burgers circuit for these dislocations yields a Burgers vector that appears to be $1/2<10\bar{1}0>$ which is most likely the projection of $1/3<11\bar{2}0>$, the Burgers vector of the most common basal dislocations in Mg alloys [77,87–91]. Less than 10 layers of brighter atomic columns are observed on the side of basal dislocation cores that experience tensile strain, suggesting the segregation of a heavier element, i.e., Y, at the dislocation cores. The STEM-EDS map in Figure 3.3(b) confirms Y segregation at the dislocation cores. While basal dislocations are shown here, we note that Y segregation may occur near other dislocations as well, including those whose Burgers vectors contain a <**c**> component. Diffusion of Y atoms with larger metallic radius than Mg [118] towards dislocations is thermodynamically driven by the volume misfit of the Y atoms and stress field created by the dislocations. This phenomenon is expected to hinder the motion of dislocations, which could influence the strength and texture evolution in Mg alloys.

High-resolution STEM analysis shows that the $\{10\bar{1}2\}$ TBs in the RD compressed Mg-3Y often have serrated morphologies, containing both CTB segments and BP facets. Figure 3.3(c) shows a typical $\{10\bar{1}2\}$ CTB, with a single layer of alternating brighter and darker columns. The brighter columns along the $\{10\bar{1}2\}$ CTB, which are Y-rich, are located on the sites with larger volumes than that in the perfect Mg crystal, while darker columns are at the adjacent sites with smaller volumes, as schematically illustrated in the figure in Figure 3.3(d). Although such segregation has not been previously reported in Mg alloys deformed at room temperature, the presence of periodic Y segregation patterns along CTBs in the current study is consistent with that reported in deformed and annealed Mg-Gd [20], Mg-Zn [20], and Mg-Ag [110] alloys. Moreover, along a serrated

$\{10\bar{1}2\}$ TB shown in Figure 3.3(e) that contains $\{10\bar{1}2\}$ CTB segments (marked by red lines) and BP facets (marked by blue lines), Y-rich clusters were observed on the BP facets. The diameters of the Y-rich clusters on BP facets were measured from HAADF-STEM images taken along the $<11\bar{2}0>$ zone axis. The sizes of these clusters range from less than 1 nm to ~4 nm, with an average size of 2 nm. Compared to segregation of solute atoms to CTBs, there are far fewer reports about segregation and clustering on BP facets. For the atomistic simulations that show the segregation tendency of a single Y atom to lattice sites near the BP facet and the influence of segregated Y on the twin boundary mobility, readers are referred to [119] for more information.

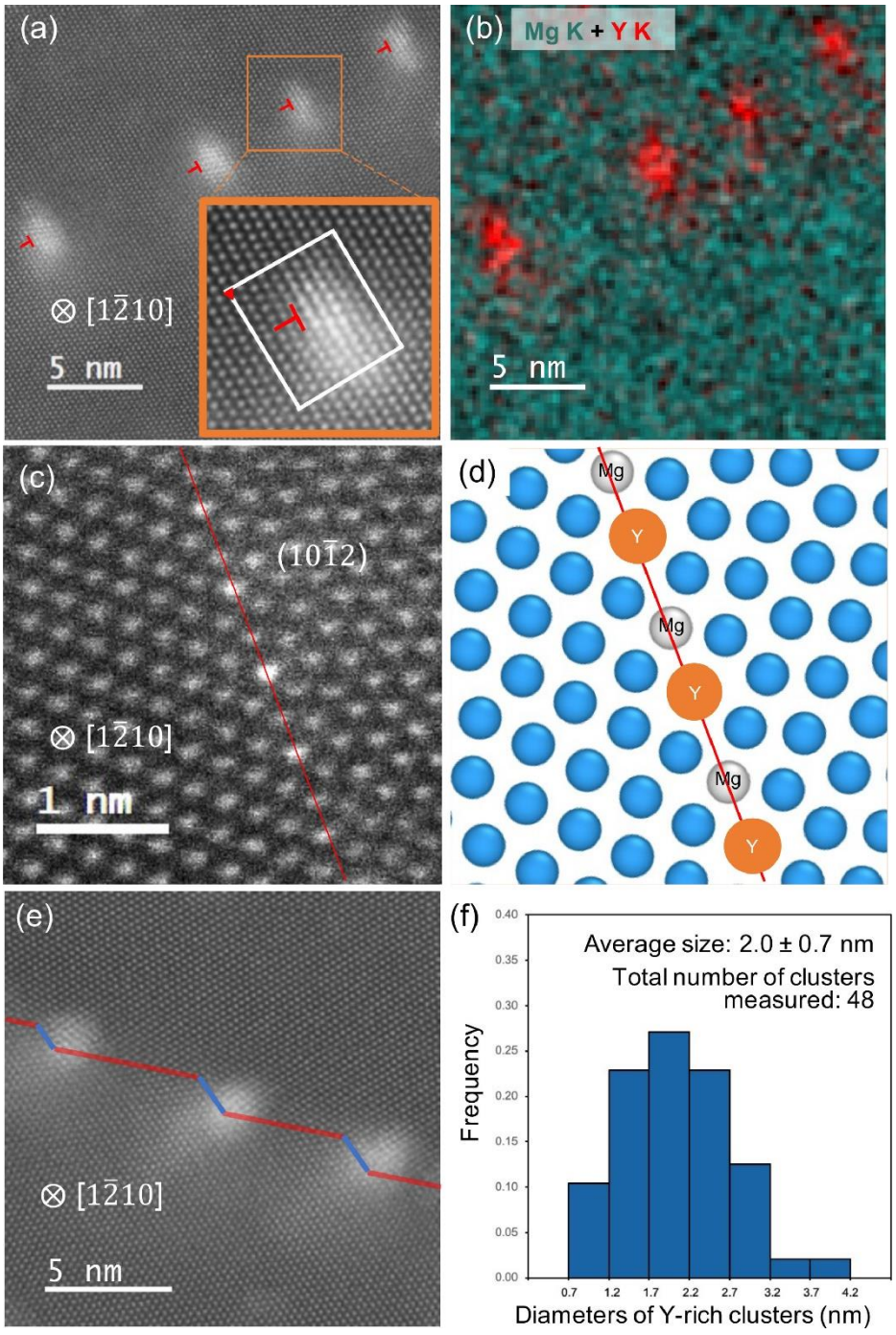


Figure 3.3. Y segregation at atomic resolution in the Mg-3Y after deformation at room temperature. (a) HAADF-STEM image of Y segregation at the tensile regions of <**a**>-type dislocation cores along a low-angle prismatic tilt boundary. (b) STEM-EDS of the same region as (a). (c) HAADF-STEM image of Y segregation at a {10-12} coherent twin boundary segment. The schematic image in (d) shows the atomic positions of Y-rich columns on the tensile sites along the {10-12} coherent twin boundary. (e) HAADF-STEM image showing Y-rich clusters

formed at a faceted {10-12} twin boundary containing basal-prismatic facets. (f) Size distribution of Y-rich clusters on basal-prismatic facets.

### 3.5. Conclusions

In summary, deformation-induced segregation of Y was observed in a Mg-Y solid solution alloy after deformation at room temperature, without subsequent annealing. Atomic resolution HAADF-STEM images show Y-rich columns at lattice dislocation cores, on the sites under tension along $\{10\bar{1}2\}$ CTBs, and clustered adjacent to BP facets. Atomistic simulations indicate that Y segregation on CTBs and BP facets is mainly driven by the local lattice distortion. Such Y segregation and clustering can hinder TB motion and lead to anisotropic mobility of faceted TBs, which will affect twinning-related hardening and plastic anisotropy. Our results suggest that the mechanical behavior and microstructural evolution in Mg alloys can be strongly affected by deformation-induced solute segregation.

# Chapter 4: Influence of Non-glide Stresses on {10-12} Twin Boundary Migration in Mg

## 4.1. Abstract

Twin thickening occurs via the migration of the twin boundary during deformation and serves as an important mechanism for accommodating plastic strain. In principle, twin boundary migration is strongly affected by the local stress state. However, the exact relationship remains unclear and challenging to determine experimentally. Here, we investigate $\{10\bar{1}2\}$ coherent twin boundary migration in Mg under various stress fields by using the nudged elastic band method to calculate its minimum energy path and hence migration barrier. The results reveal an appreciable influence of non-glide stresses on coherent twin boundary migration. Specifically, a compressive normal stress reduces the energy barrier. We formulate a phenomenological model to describe the energy barrier as a function of the ratio between the shear stress and the critical resolved shear stress for coherent twin boundary migration and reveal that non-glide stresses can change the critical resolved shear stress and, consequently, the probability of coherent twin boundary migration. In addition, by examining the atomic mechanisms underlying coherent twin boundary migration, we find that the Burgers vector of the twinning disconnection observed during coherent twin boundary migration is smaller than the one widely reported in the literature. The energetically favorable configuration of this twinning disconnection varies for different non-glide stresses causing a non-glide stress-dependent energy barrier. As a whole, this study improves our understanding of fundamental deformation mechanisms and enables more accurate models of twinning-induced plasticity.

## 4.2. Introduction

The limited strength and low ductility of Mg and Mg-rich alloys are a direct result of their hexagonal close packed (hcp) structure [2]. According to the von Mises criterion, five independent slip systems are needed to accommodate an arbitrary shape change without cracks for a polycrystalline material under plastic deformation [11]. However, Mg has only four independent slip systems that can be easily activated at room temperature (i.e., 2 independent systems of basal <**a**> slip and 2 independent systems of prismatic <**a**> slip). Consequently, $\{10\bar{1}2\}$ deformation twinning, in addition to dislocation slip, is an active deformation mechanism in Mg and has been shown to play a significant role in accommodating plastic strain, often determining material strength and ductility.

Extension $\{10\bar{1}2\}$ twins develop in multiple stages when deformation is applied, starting with twin embryo nucleation, then propagation of the embryo along the twinning direction into a planar-shaped lamella, and finally thickening (growth), during which the lamella expands perpendicular to the twinning plane. Twin thickening involves twin boundary migration, which is generally assisted by nucleation and propagation of twinning disconnections (TDs). TDs are a type of interfacial defect that resides in the twinning plane and is described by a combination of a Burgers vector component, $\boldsymbol{b}$, and a step height component, $h$ [25,26,120]. TDs are highly mobile and can glide along the twin boundary, the basal-prismatic (BP) interface, and/or the prismatic-basal (PB) interface [38] to enable the reorientation of the crystal and, therefore, allow twin boundary migration to occur.

While prior studies of twin boundary migration have involved the interaction between TDs and BP/PB interfaces [121,122] and the sources of TDs [36,37], it is also important to understand the fundamental energetics of the underlying mechanism behind the observed phenomena. For

example, $\{10\bar{1}2\}$ deformation twinning in Mg is dominated by atomic shuffling at room temperature and under normal strain rates, at least during the twin nucleation stage [62]. Other studies have shown that a lower energy barrier allows for easier glide of $\{10\bar{1}2\}$ TDs compared to $\{10\bar{1}1\}$ TDs [39]. By studying the energetics of TD glide, the stable configuration of TDs for each twinning mode can be identified [40].

The energy barrier acts as a key parameter for the Arrhenius equation that describes the rate at which an event occurs [61]. Many studies have shown that the applied stress modulates the mobility of not only twin boundaries [123], but also grain boundaries [63]. When the twin resolved shear stress (TRSS) for twin boundary migration reaches a threshold value, the critical resolved shear stress (CRSS), migration will be spontaneous. Although the inaccuracy of twin behavior prediction based only on the TRSS and Schmid factor (i.e., "the non-Schmid effect") has been widely reported [23,73,124–128], it is usually argued that stress concentrations or other defects are responsible for pushing the local stress state away from the applied stress [124,125]. However, non-glide stresses which are not accounted for in the TRSS have been mostly ignored and excluded in the activation models for twinning [24,123], with only a few studies discussing the role of non-glide stresses on deformation twinning of hcp materials [129–131]. Through an elastic continuum model, the influence of hydrostatic pressure on twin nucleation and propagation has been found to be negligible compared to that of the TRSS when they are on the same order [129]. In another study, it was proposed that non-glide stresses will influence the dislocation core structure before plastic deformation and promote deformation twinning or dislocation glide [130,131]. However, to date there is no systematic study to quantify the enhancement or the hinderance of non-glide stresses on deformation twinning.

In view of the above discussion, we formulate an energetic framework to study coherent twin boundary (CTB) migration in pure Mg. Using the nudged elastic band (NEB) method, we evaluate the energy barrier of this event and show how it varies not only with glide stresses but also strongly with non-glide stresses. Specifically, results reveal that the compressive stress significantly reduces the barrier for CTB migration. We formulate a phenomenological model to include the non-glide dependence of the energy barrier upon the applied stress field, enabling prediction of CTB migration under an arbitrary deformation state. We also study the CTB migration mechanism and highlight the importance of bulk atom displacement in addition to the boundary migration assisted by TDs. By structural analysis of the intermediate states, our findings suggest that the Burgers vector of TDs during CTB migration may not necessarily be the widely reported value and the energetically favored TD configuration is subject to change under a non-glide stress.

### 4.3. Methods

To study $\{10\bar{1}2\}$ coherent twin boundary (CTB) migration in pure Mg, we use the Large-scale Atomic/Molecular Massively Parallel Simulator (LAMMPS) [55] with a modified embedded atom method (MEAM) potential developed by Wu et al. [132]. This interatomic potential makes robust prediction of $\{10\bar{1}2\}$ twin behavior because it produces the $\{10\bar{1}2\}$ twin interface and the core structure of the $\{10\bar{1}2\}$ TD which match first-principles density function theory calculations [132]. Figure 4.1(a) shows the simulation cell consisting of a $\{10\bar{1}2\}$ CTB aligned on the xy-plane near the center, with visualization accomplished using OVITO [133]. Hereinafter, the region above the CTB is defined as the twin and that below the CTB as the matrix.

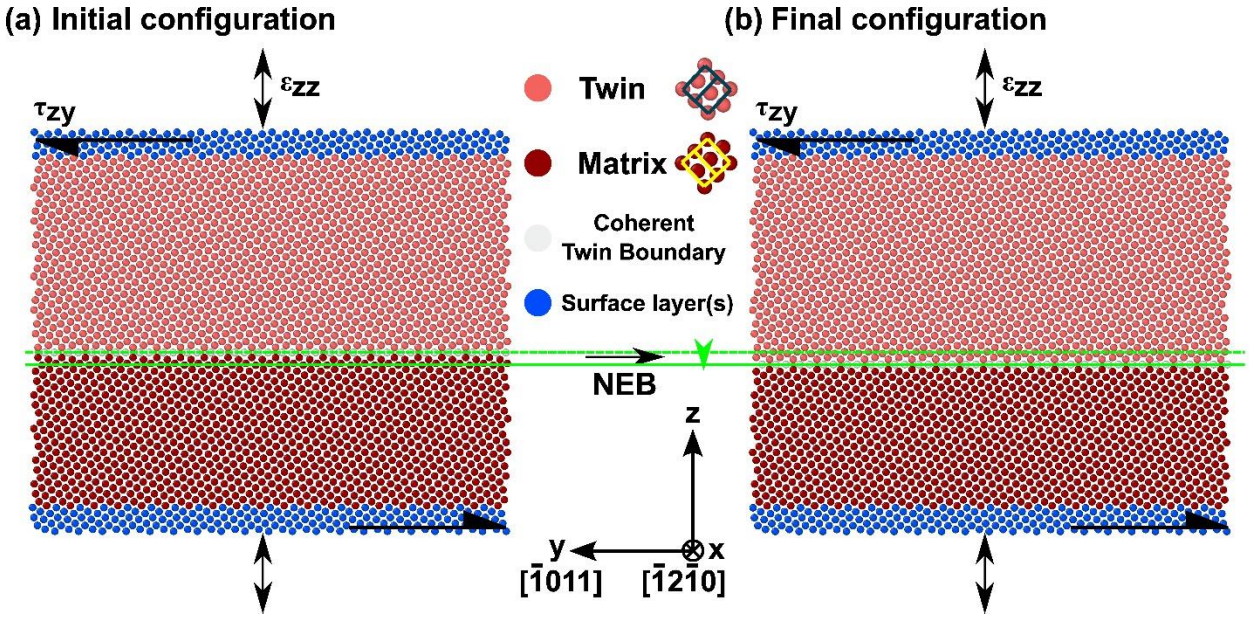


Figure 4.1. The atomic snapshots of the initial and final configurations (before and after twin boundary migration) used in the nudged elastic band (NEB) calculations. Atoms are colored based on different regions, i.e., matrix, twin, and coherent twin boundary. The coherent twin boundary (CTB) in the final configuration has migrated two atomic layers from its initial configuration. The shear stress $\tau_{zy}$ and the normal strain $\varepsilon_{zz}$ can be imposed on the system, as indicated.

The simulation box of the initial configuration contains 10,880 atoms and its dimensions are 1.27 nm along the x-direction (i.e., $[\bar{1}2\bar{1}0]$), 15.14 nm along the y-direction (i.e., $[\bar{1}011]$, the twinning direction) and 12.71 nm along the z-direction (i.e., the normal direction to the twinning plane $(10\bar{1}2)$). Periodic boundary conditions (PBCs) are applied along the x- and y-directions, while a non-periodic and shrink-wrapped boundary condition is used in the z-direction. Figure 4.1(b) displays the targeted final configuration that has the same type of CTB but after the boundary has migrated two atomic layers with respect to the initial configuration, which is the smallest unit distance of CTB migration. Note that the atomic layer between the initial and the final CTB locations is another $\{10\bar{1}2\}$ plane with different x coordinates. Using these initial and final configurations, the NEB method is adopted to study the minimum energy path (MEP) of CTB migration at zero temperature (T = 0 K) [60].

By varying the shear stress and the normal strain as the two independent variables, one can evaluate how stress modulates the activation energy for CTB migration because the local stress at the twin is close to the uniformly applied stress when only the defect is isolated in the center of the simulation cell. Under this simulation setup, it can be assumed that the applied shear stress approximates the TRSS, and the applied normal strain does not contribute to the TRSS and therefore is the non-Schmid component that is focused on in this study. For the first set of NEB calculations, a constant normal strain (0% normal strain, 2% compressive strain or 2% tensile strain) is set for each group, while the shear stress is varied in 0.1 GPa increments until the energy barrier reaches zero and CTB migration becomes spontaneous. Similarly, in the other set of calculations, a shear stress (0, 0.3 GPa or 0.6 GPa) is kept constant for each group, while the normal strain is varied by increments of 1% in the range of -5% to 3%. The lower tensile strain limit is due to an instability of NEB algorithm under a large tensile strain. The shear stress $\tau_{zy}$ is applied by setting atomic forces to the top and bottom layers, and the normal strain $\varepsilon_{zz}$ is applied by imposing a shape change along z to the simulation box. Due to the positioning of PBCs along x- and y- direction, Poisson tension/compression is not allowed, which results in normal stresses $\sigma_{xx}$ and $\sigma_{yy}$. The magnitude of $\sigma_{xx}$ and $\sigma_{yy}$ is ~50% of $\sigma_{zz}$.

NEB calculations under a pure tensile strain are performed using 32 replicas (i.e., 30 intermediate configurations plus 1 initial configuration and 1 final configuration) and the stress-free case using 46 replicas. All other NEB calculations are performed with 64 replicas. Different numbers of replicas are chosen to attain better convergence for all the NEB calculations described in this chapter and this adjustment does not significantly affect the results. Before the NEB calculation starts, both initial and final configurations are relaxed using a conjugate gradient algorithm to make sure systems are at a local minimum of potential energy.

## 4.4. Stress-dependent migration path and energy barrier

### 4.4.1. Stress-dependent minimum energy path (MEP)

Figure 4.2(a) shows the normal strain-dependent MEPs of CTB migration under zero applied shear stress. The reaction coordinate represents the progress of CTB migration and is defined as the two-norm of 3N-length distance vector between the atoms at the current replica and those at the initial replica, where N is the total number of atoms in the system. Note that in the MEPs of this work, the y-axis is labelled as Δ potential energy (i.e., change in potential energy) and that the absolute value of potential energy for these initial configurations under different applied stress is not the same. The energy barrier is defined as the potential energy difference between the maximum potential energy along the MEP and the initial potential energy, as shown in Figure 4.2(a).

The MEP under stress-free condition is depicted by the "0% normal strain" curve in Figure 4.2(a). The symmetry of the MEP curve also indicates that the stress-free migration event is equally likely to happen also in a reverse way (i.e., CTB migrating upwards by 2 atomic layers from the final configuration to the initial one). The MEP curve gets "flattened" as the normal strain increases either way, compressive or tensile, while the curve remains nearly symmetric as long as there is no shear stress. The migration path flattening and decrease in energy barrier indicate the normal stress dependence of CTB migration. In all the MEPs illustrated in this work, two special replicas corresponding to TD nucleation and TD recombination are labeled. These two replicas divide the whole migration process into three stages.

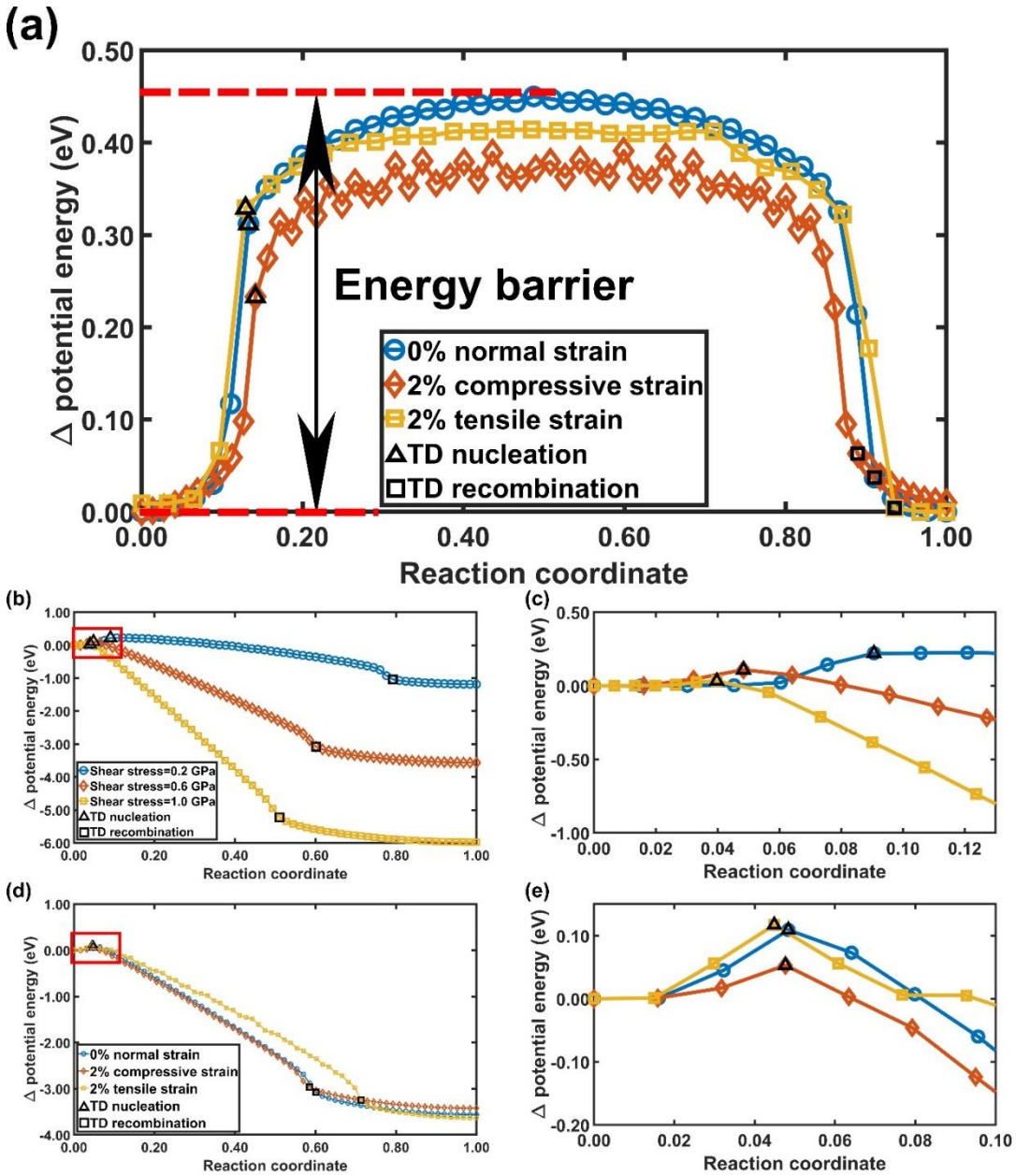


Figure 4.2. (a) Normal strain-dependent minimum energy paths (MEPs) under zero applied shear stress as a function of reaction coordinate (RC). The replica labeled with triangle represents when TDs nucleation and that labeled with square represents when TDs recombine and cancel each other. Energy barrier in this study is defined as the energy difference between the saddle point and the initial local minimum. (b) Shear stress-dependent MEPs under zero applied normal strain as a function of reaction coordinate. An enlarged view of a few highlighted starting replicas including the saddle point is provided in (c). (d) Normal strain-dependent MEPs under an applied shear stress of 0.6 GPa as a function of RC. An enlarged view of a few highlighted starting replicas including the saddle point is provided in (e).

In Figure 4.2(b), the MEPs of CTB migration are found to vary with the applied shear stress (i.e., with a zero normal stress). Figure 4.2(c) enlarges the highlighted section of Figure 4.2(b). As shear stress increases, a potential energy difference between the initial and the final configuration appears. This directly results in a lower energy barrier for CTB migration and a higher energy barrier for the reverse migration. Therefore, CTB migration is heavily biased towards moving along the -z direction of the simulation box. Another important observation is that the downward shift of the central region of the MEP with increasing shear stress, which corresponds to spontaneous TD migration.

In Figure 4.2(d), we show MEPs in which the normal strain was varied while the shear stress was kept constant at 0.6 GPa. Figure 4.2(e) enlarges the critical region of the MEPs delineated by a red box in Figure 4.2(d). The normal strain, unlike the shear stress, does not result in a significant energy difference between the initial and the final configuration. The compressive strain lowers the energy barrier for TD nucleation while the tensile strain slightly increases it compared to that without normal strain. The replicas where TDs nucleate have a similar reaction coordinate for all three normal strain levels, while the TD recombination happens later under tensile strain compared to the other two.

### 4.4.2. Energy barrier as a function of shear stress and normal strain

To evaluate how the stress field can affect CTB migration energy barrier, the data are presented from two perspectives – (1) varying the shear stress at three constant normal strain levels in Figure 4.3(a) and (2) varying the normal strain at three constant shear stress levels in Figure 4.3(b). For all the three normal strain values (-2%, 0%, 2%) in Figure 4.3(a), the imposed shear stress lowers the energy barrier. The CRSS at which the energy barrier reaches zero is no longer a constant and dependent upon the applied normal strain. The compressive strain lowers the CRSS significantly

and therefore makes CTB migration much easier. The tensile strain only slightly increases the CRSS, hindering CTB migration.

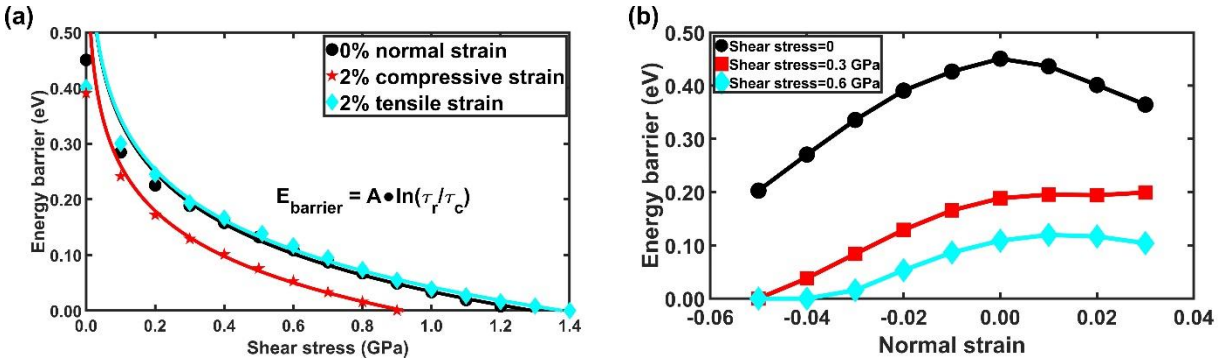


Figure 4.3. (a) Energy barrier of CTB migration as a function of shear stress under three different normal strain levels (0% normal strain, 2% compressive strain and 2% tensile strain). Fitted curves and the equation the fitting model follows are also given, where $\tau_c$ is a constant dependent on the imposed normal strain. (b) Energy barrier of CTB migration as a function of normal strain under three different shear stress levels (0, 0.3 GPa, and 0.6 GPa).

Some but not all crystal plasticity (CP) models assume the shear rate caused by a certain plastic deformation system is proportional to the ratio of the resolved shear stress and the CRSS for that system via a power law relationship

$$\dot{\gamma^s} = \dot{\gamma_0}(\frac{\tau_r^s}{\tau_c^s})^n \tag{4.1}$$

where $\dot{\gamma}$ is the shear rate, n is a constant that is independent of applied shear and normal loading, $\tau_r$ is the resolved shear stress, $\tau_c$ is the CRSS, and the superscript s is the notation of a given plastic deformation system [134,135]. In this way, the contribution of every plastic deformation system to the plastic flow is always considered even if its resolved shear stress is below its CRSS. This power-law relationship is a mathematical model inspired by the constitutive equation for describing non-linear viscosity [136].

Here in Figure 4.3(a), the ratio between the TRSS and the CRSS is also found to be correlated with the calculated energy barrier under different shear stress. The fitting curves show a relationship in the form of

$$E_{barrier} = A \cdot ln\left(\frac{\tau_r}{\tau_c}\right) \tag{4.2}$$

where $\tau_r$ is the TRSS and equal to the applied shear stress since the normal loading does not contribute to the TRSS [24], $\tau_c$ is the CRSS for CTB migration and is the x intercept of the curve and A is a constant. The logarithmic function best fits the relationship among all the elementary functions.

For all the shear stress levels above zero in Figure 4.3(b), the imposed compressive strain decreases the energy barrier while the tensile strain increases the energy barrier but less significantly, expect for 3% tensile strain under 0.6 GPa shear stress where the energy barrier slightly decreases. The zero energy barriers shown in Figure 4.3(b) also indicate that the CRSS is further lowered down to below 0.6 GPa under 4% compressive strain and to below 0.3 GPa under 5% compressive strain. Briefly, Figures 4.3(a) and 4.3(b) altogether reveal the important role the compressive strain may play in assisting CTB migration.

The computational results show the non-glide stress induced CRSS and CTB migration barrier variation. This may provide an explanation to the reported breakdown of the Schmid law from experiments [23,73,130]. To further reveal the shear rate dependency upon the TRSS and the CRSS, we assume thermal activation theory which states that an event's probability can be described with an Arrhenius equation such as:

$$\dot{\gamma} \propto exp\left(-\frac{E_{barrier}}{kT}\right) \tag{4.3}$$

where $\dot{\gamma}$ here represents the rate of CTB migration, k is Boltzmann constant, and T is the absolute temperature. It is also implicitly assumed that the energy barrier is independent of temperature by using the calculated energy barrier under a non-zero temperature. Combining Equations (4.2) and (3), one can reduce them to the form of Equation (4.1), which is

$$\dot{\gamma} \propto \left(\frac{\tau_r}{\tau_c}\right)^n \tag{4.4}$$

where n is the same constant in (1) and equal to $-\frac{A}{kT}$. Table 4.1 contains the model parameters for three groups of calculations under different normal strains. The applied non-glide stress varies the CRSS value in this model, while the power n is around 5 for all groups under room temperature, indicating the n may be a constant for a given plastic deformation system.

Table 4.1. Parameters in Equations (4.3) and (4.4) under different normal strain (T = 300 K, this temperature is chosen arbitrarily to provide a numerical value of n).

| | CRSS (GPa) | A (eV) | n |
|---|---|---|---|
| 0% normal strain | 1.29 | -0.133 | 5.15 |
| 2% compressive strain | 0.92 | -0.117 | 4.54 |
| 2% tensile strain | 1.38 | -0.131 | 5.08 |

This model matches well with the acquired data from NEB calculations with R-squared values of all three fittings above 0.99. The only discrepancy appears when the shear stress approaches zero. For Equation (4.3), mathematically one will have an energy barrier value approaching infinity if $\tau_r$ stays positive but gets closer to 0, which is physically unrealistic and causes the deviation. This will not affect the migration rate prediction by the model too much. This is because under a shear stress approaching 0, the CTB migration has nearly the same probability of happening in each direction (i.e., migrating upwards or downwards) and the net migration is thus much less likely to

happen. Consequently, $\dot{\gamma}$ in Equation (4.4) should, both theoretically and via this model, be at a very low level in the case of $\tau_r \sim 0$.

Generally, Equation (4.4) has the same format as Equation (4.1) and the data from NEB calculations can even give a suggested value of the constant in the exponent of the ratio between the TRSS and the CRSS (i.e., *n* in this study) because NEB analysis correlates the energy barrier and the TRSS. The two scales, the TRSS through the flow rule and the energy barrier through the Arrhenius equation, are consistent in predicting the CTB migration event at this point.

## 4.5. Migration mechanism and mechanistic model

### 4.5.1. Migration mechanism

In addition to the energy barrier, the NEB calculations can also reveal the intermediate states along MEPs, which can provide information on the CTB migration mechanism at the atomic scale. To demonstrate, we first consider the load-free CTB migration case to elucidate the migration mechanism and then introduce a case where the shear stress is applied. Figure 4.4(a) includes the MEP curve of the load-free CTB migration. Three stages, separated by the two events (i.e., the TD nucleation and the TD recombination), are labeled. Five states (replicas) denoted with A-E along the MEP in Figure 4.4(a) are highlighted and their atomic structures are shown in Figure 4.4(b).

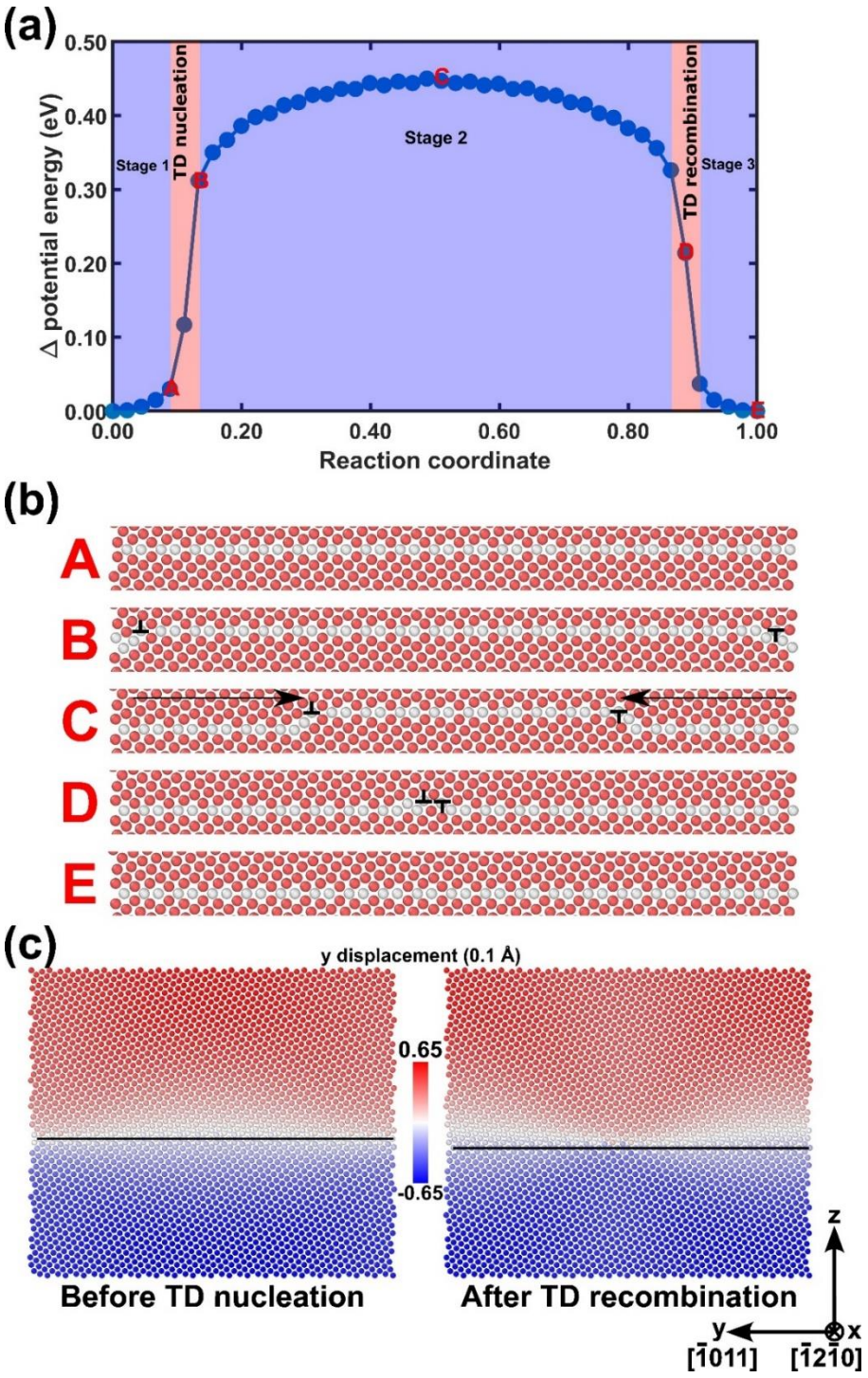


Figure 4.4. (a) The MEP of the CTB migration under the stress-free condition. Three key stages, TD nucleation, and TD recombination are colored along the MEP. Five representative states (replicas) A-E are labeled, and their atomic structures are presented in (b). Atoms are colored based on their local structural environment, red: hcp, gray: boundary atoms that are not of any specified structure type. (c) The atomic displacement during Stage 1 (before TD nucleation) and Stage 3 (after TD recombination) along y direction. The unit of y displacement is 0.1 Å.

Replica A is the critical state right before the pair of TDs nucleates. The atomic configuration of the initial CTB shows that the twin boundary is flat, while the other atomic layers have the corrugated structure (i.e., two nearest atoms in the same atomic layer have different z coordinates) as shown by the atomic configuration of the twin boundary (colored in white) in Replica A of Figure 4.4(b). Atoms in the vicinity of the CTB remain static during stage 1, while atoms that are farther away from the CTB (referred to as bulk atoms) moves, as shown in Figure 4.4(c). Only the y displacement is plotted since it is the dominant component comparing to x and z displacements. The twin shear seems to happen in bulk atoms even before and after the boundary migrates. The collective motion of these atoms, which corresponds to a minor rise in the total potential energy of the system, is a prerequisite of TD nucleation and later CTB migration. This finding indicates that the atomic configuration in and near the CTB alone cannot fully describe CTB migration, but that bulk atom displacement is required.

After the prerequisite displacement of bulk atoms, a few atoms near the TD nucleation site in the CTB start to move in replica B. Those atoms show the formation of a pair of TDs by shear (i.e., the collective horizontal displacement) and shuffle (i.e., the relative vertical displacement) of the two atoms. In a CTB, to conserve the Burgers vector, the TDs must nucleate in pairs. Figure 4.4(a) also indicates the process of TD nucleation consumes much energy though the actual atomic displacement and the corresponding range of reaction coordinate is relatively short.

Theoretically the site where the TD pair nucleates in replica B should be random because every site on the CTB is identical given the coherency of the twin boundary and the PBC along horizontal direction. However, in this study, the nucleation always occurs at the edge of the simulation box, which may be caused by some precision-induced minor variation of the lattice parameter along the CTB. A comparative calculation where the CTB atom at the center of the simulation box is

displaced by a tiny distance (e.g., 0.001 Å) is also conducted. Shown by Figure 4.5, it is observed that the nucleation occurs at the site where the boundary atom is displaced in the CTB instead of the edge, while the MEP and the energy barrier value do not significantly change. Consequently, we do not anticipate that the exact location of the nucleation site will significantly alter the results.

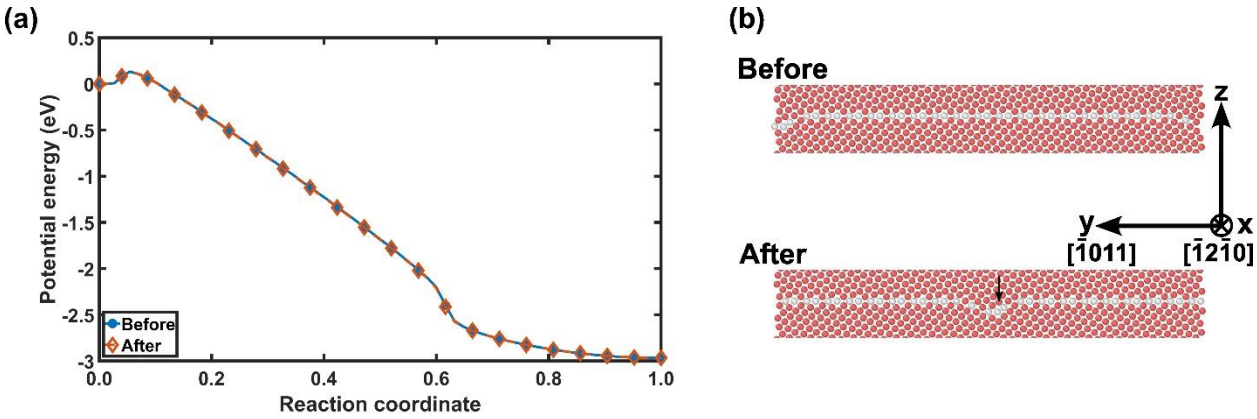


Figure 4.5. (a) The MEP of the CTB migration under a shear stress of 0.5 GPa before (i.e., the condition adopted in the above-mentioned study) and after the +0.001 Å y-displacement of an atom in the middle of the initial CTB. (b) The atomic configuration of the replicas where the TDs nucleate before and after the tiny displacement.

To complete the boundary migration, each TD must propagate in opposite directions on the CTB. Replica C is chosen within Stage 2, TD migration. As the TD pair sweeps through, part of the crystal is reoriented with the final CTB growing. This process also turns the atomic layer of original CTB to be corrugated as other non-CTB atomic layers. Only one representative atomic configuration on the process of TD migration is shown in Figure 4.4(b) since the atomic configuration near all TDs is the same. Energetically, this process also sees a slight potential energy increase to the saddle point in the middle of the MEP followed by a symmetrical potential energy drop. Physically, the symmetry is due to the similarity in both structure and energy of the initial and the final configuration. The saddle point is in the middle because the interaction energy

increases as the two TDs depart from each other and then decrease again as they get closer again [120].

At the end of the travel of the TD pair, one TD would finally meet the other somewhere in the CTB. Replica D sees the recombination of TDs. Like that in TD nucleation, the potential energy drops dramatically due to the restoring of the CTB structure. Moving forward, Replica E marks the end of CTB migration. It is observed that bulk atoms, again, displace themselves to further relax the energy of the system and complete the twin shear, as shown in Figure 4.4(c).

Based on the above mechanism, there are two key events during the CTB migration process, the nucleation of a pair of TDs and the recombination of it. The former one marks the beginning of TD migration along the twinning direction, and the latter sees its end where the pair of TDs meets and must recombine and restore the coherency of the twin boundary.

As highlighted in the MEPs of Figures 4.2(a), 4.2(b) and 4.2(d), all CTB migration processes under different applied stress will go through the processes of bulk atom displacement, TD nucleation, TDs migration, TD recombination, and bulk atom recovery. The similar migration mechanism also explains why the MEPs shown in Figure 4.2 share some common features like (1) a steeper potential energy rise/fall at the replicas where TDs nucleate/recombine, (2) a smooth potential energy change during the two stages of bulk atom displacement. However, there are still a few noticeable stress-induced variations to the energy pathway. Figure 4.6 shows another example of CTB migration, but under a shear stress of 0.5 GPa. While all these processes still exist, both TD nucleation and TD recombination shift to an earlier stage of the MEP under a larger shear stress because of a smaller energy barrier and shear stress-induced broken symmetry of the initial and the final configuration. Also, for all cases with a reasonably high shear stress (precisely, equal to or larger than 0.3 GPa), the energy barrier sits at the exact replica where a pair of TDs nucleates,

which means the TD migration may not consume energy and become spontaneous, as shown in Figure 4.6(a). Here, the applied stress field, instead of the TD interaction, significantly changes the energy barrier and the MEP, different from the stress-free case. Figure 4.6(b) shows the similarity of atomic configurations near the twin boundary. Figure 4.6(c) indicates that another feature, the bulk atom displacement before TD nucleation and after TD recombination still occurs, but with a shorter displacement especially before TD nucleation. There is also no other type of disconnections but only a stress-induced configuration variation observed. We need to refer to that structural variation of TDs to understand how the stress field makes a difference to the MEP.

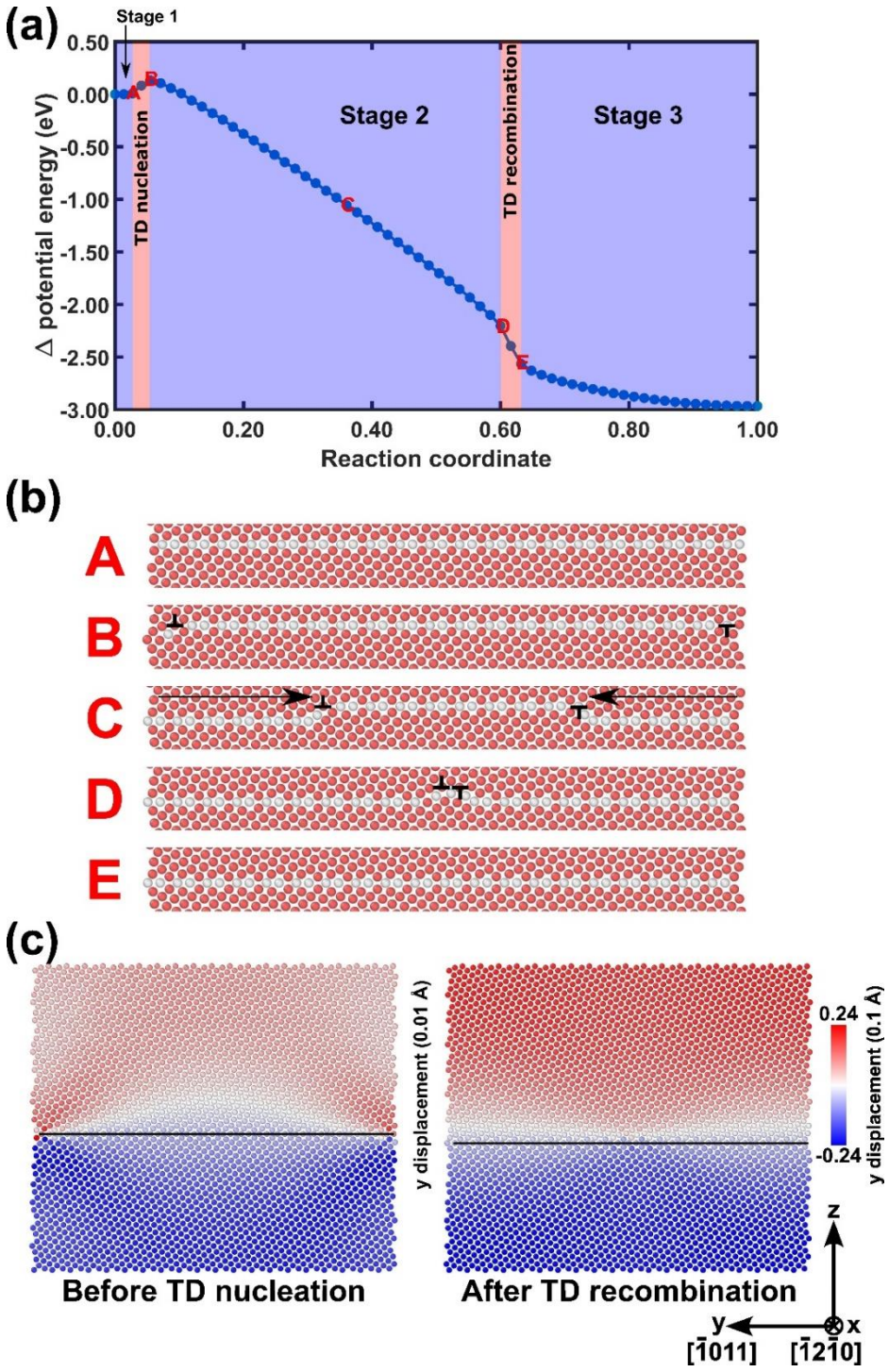


Figure 4.6. (a) The MEP of the CTB migration under a shear stress of 0.5 GPa. Three key stages, TD nucleation, and TD recombination are colored along the MEP. Five representative states (replicas) A-E are labeled, and their atomic structures are presented in (b). Atoms are colored based on their local structural environment, red: hcp, gray: boundary atoms that are not of any specified structure type. (c) The atomic displacement during Stage 1 (before TD nucleation) and Stage 3 (after TD recombination) along y direction. Note that the unit of y displacement is 0.01 Å and 0.1 Å for the left figure in (c) and the right figure in (c), respectively.

### 4.5.2. Structural variation of the CTB and the TDs upon applied load

The stress-dependent energy barrier difference can be ultimately attributed to the structural variation of both the atomic structure of the CTB and the TDs upon the stress field. Before discussing the structural variation of the CTB, the atom numbering and the TD labeling is defined in Figure 4.7(a) for the clarity of discussion. Figure 4.7(b) illustrates the kite-shaped structural unit in the vicinity of both the initial and the final CTB, which visualizes the structural variation through this structural unit.

Figures 4.7(c) and 4.7(d) both depict two neighboring structural units captured from the initial configuration. For Figure 4.7(c), it shows how the structural unit would vary when the applied shear stress increases from 0 to 1.2 GPa – as the shear stress goes up, the structural unit shears accordingly, while the distance between the two neighboring units remains unchanged. In this way, the lattice symmetry about the CTB is broken, which is the structural reason why the MEP will not be symmetrical about the saddle point and CTB migration downwards is energetically favorable. Figure 4.7(d) presents the difference of the structural unit upon different applied normal strains. As the normal strain goes from 5% compressive to 3% tensile, there is no net shear of the structural unit, and the symmetry of the CTB is kept, which is consistent with the symmetry of MEPs of the normal strain cases. The notable difference here is the stretch along z-direction and some accompanying horizontal displacements as indicated in Figure 4.7(d). To understand the structural variation in a quantitative manner, Figure 4.7(e) defines the relative horizontal displacement for atoms in the initial CTB by comparing the atom position with the imaginary atom belonging to the lattice below the initial CTB.

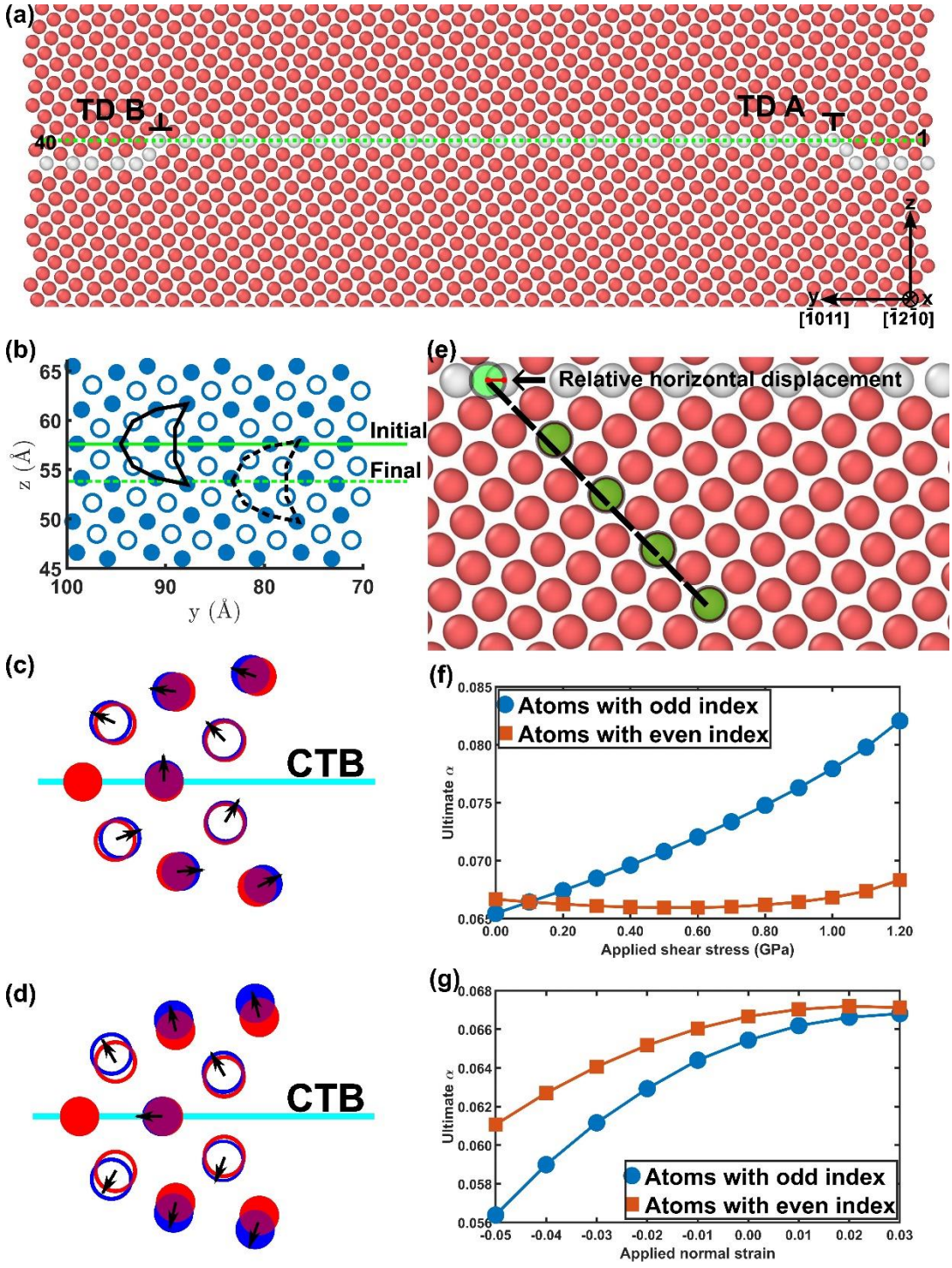


Figure 4.7. (a) The diagram showing a typical configuration during the CTB migration in which the atom number and TD A and B in (c)-(f) are defined. (b) Kite-shaped structural unit of atoms (outlined in black) in the vicinity of the initial CTB and the final CTB under the stress-free condition. The atoms represented by the filled circles have a different x coordinate than those represented by the open circles. (c) The evolution of one representative structural unit under increasing shear stress from 0 (the red atoms) to 1.2 GPa (the blue atoms); (d) The evolution of one representative structural unit when the normal strain goes from 5% compressive (the red

atoms) to 3% tensile (the blue atoms). (e) The diagram showing the CTB and its vicinity in which relative horizontal displacement of CTB atoms is defined. The displacement is exaggerated for illustrational purpose. (f) The necessary relative horizontal displacement for atoms in the initial CTB to move to their final positions, normalized by the length of [10-11] (denoted as ultimate α) as a function of shear stress; (g) Ultimate α for atoms in the initial CTB as a function of normal strain.

Figures 4.7(f) and 4.7(g) show the necessary relative horizontal displacement normalized by the length of $[10\bar{1}1]$ for atoms in the initial CTB, denoted as ultimate α, to move to their positions in the final configuration. This value should be equal to the magnitude of the Burgers vector of a full TD upon stress. The two figures show that the TD structure and the displacement field during the CTB migration will depend on the applied stress. Please note there must be two values of the horizontal displacement because the two neighboring Mg atoms at CTB are not equivalent from the perspective of crystallography. This is considered to be the structural origin of why twinning cannot be achieved by homogeneous shear, and atoms must shuffle [15].

In Figure 4.7, the structural variation of the CTB under the stress field is revealed. However, it is the potential energy at a few key configurations, including (1) the starting configuration, (2) the configuration of the saddle point (usually the one where TDs nucleate), and (3) the final configuration, which determines the energy barrier physically. It is found that the correlation between structure and energy is not that straightforward by checking the structural unit at the 3 key configurations. For example, a larger relative horizontal displacement (i.e., the y value in Figures 4.7(f) and 4.7(g)) does not necessarily result in a higher energy barrier.

Figures 4.8(a)-(d) show the relative horizontal displacement normalized by the length of $[10\bar{1}1]$ for atoms in the initial CTB, denoted as α, under four loading conditions. At the position of TDs which is denoted by the red- and magenta-colored dots, α will have the same meaning as its

Burgers vector normalized by $[10\bar{1}1]$. The contour represents the relative atomic horizontal displacement value at the specific replica (x-axis) and for the specific atom (y-axis). The behavior for a total of 40 atoms at the initial CTB is shown. The atomic numbering and how the relative horizontal displacement of CTB atoms is calculated are the same as illustrated in Figures 4.7(a) and 7(b). The left white line labels the TD nucleation, while the right one is for the TD recombination. Contours in the Figures 4.8(c)-(f) are mostly serrated because of the nonequivalence of two neighboring Mg atoms at CTB.

It is worth noting that the atomic displacement keeps increasing during the whole migration process. In other words, the reorientation of crystal from matrix to twin is not fully completed right after a TD passes or after TDs annihilate. It is only true that the atomic displacement increases at a largest rate as a TD passes that atom. The relative displacement is unable to reach the ideal value at a fully relaxed TD, about $\frac{1}{15}[10\bar{1}1]$, which is given by [26]

$$\boldsymbol{b}_{tw} = \lambda[10\bar{1}1], \lambda = \frac{3-\kappa^2}{3+\kappa^2} \tag{4.5}$$

, where $\kappa$ is c/a in Mg, until the final configuration of the stress-free migration. We find that the Burgers vectors of TDs in the intermediate states are smaller than the above theoretical value and no longer a constant. Consistent with the migration mechanism, there is no systematic variation of the relative displacement but only some value changes caused by different loading conditions, as shown by Figures 4.8(a)-(d).

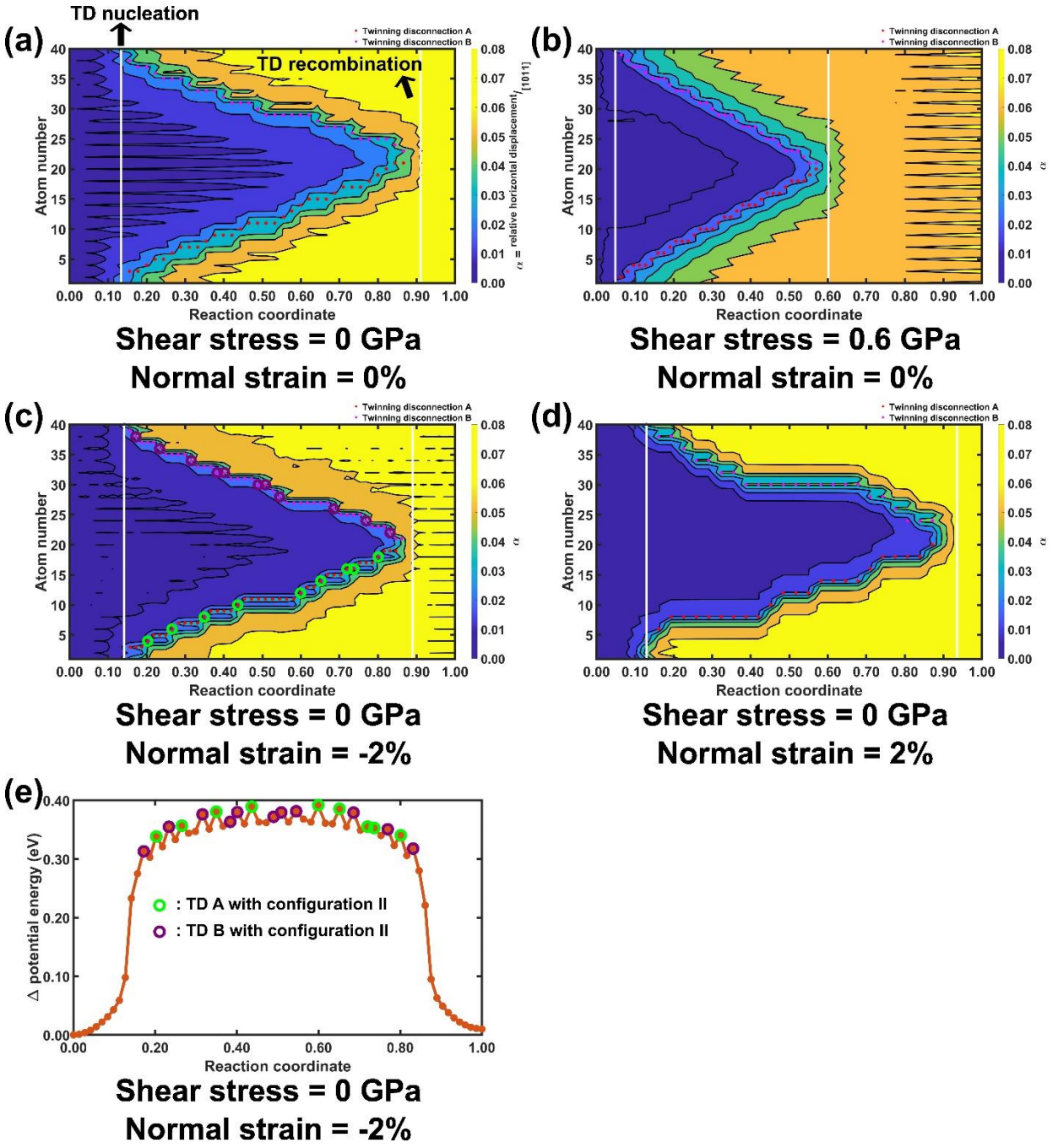


Figure 4.8. The contour plots show the relative horizontal atomic displacement normalized by the length of [10-11] (denoted as α) of 40 atoms in the initial CTB by each replica under (a) stress free condition (no imposed shear stress and normal strain); (b) Pure shear stress of 0.6 GPa; (c) a compressive strain of 2%; (d) a tensile strain of 2%. In all the contour plots, the red and magenta dots represent the position of two TDs, while the left white line means the replica where TDs nucleate and the right one means the replica where TDs recombine. Specifically, in (c), a few TDs A and TDs B with the non-dominant TD configuration are highlighted in green and purple circles and correspond to the replicas labeled in the same way in (e), the MEP under a compressive strain of 2%.

The discrepancy of the Burgers vector of TDs may be caused by the arrangement of the initial and final configuration. When the initial and final configurations are strictly fixed with boundary conditions along x and y being PBCs, it seems that the MEP will favor a steady reorientation instead of an abrupt one that completes as soon as TD sweeps through. This is also why bulk atoms would move before TD nucleation and after TD recombination. It should be noted that the TD configurations observed in this study are not energetically stable because the intermediate state they are in is not at a local potential energy minimum. Therefore, they cannot be present for a long period and may evolve to the commonly reported TD configuration with a Burgers vector of $\boldsymbol{b}_{tw}$ in a fully relaxed system. However, interestingly, NEB predicts that the steady reorientation assisted by the energetically unstable TD could lower the energy barrier more so than the commonly reported TD. While this result needs verification it nonetheless opens the possibility of a non-conventional TD configuration during CTB migration.

### 4.5.3. Two different configurations of twinning disconnections (TDs)

From the above discussion, TDs are key to understanding CTB migration because: (1) TD nucleation consumes the most energy, and the replica where the pair of TDs nucleates sits at the saddle point for cases in the large shear stress regime; (2) the TD is the only defect other than twin boundary during the CTB migration process.

The core structure of TDs can be represented by the atomic configuration near the TDs (i.e., relative positions of atoms). Figure 4.9 shows two different configurations of the TDs observed along the MEPs. Although they both have two atomic layer-high steps and similar Burgers vectors, the local environment of the step can be classified into two categories in Figures 4.9(a) and 4.9(b), denoted as configuration I and configuration II. Atoms are colored according to their local structural environment using the polyhedral template matching method in OVITO [137]. The red

atoms have a hcp-type environment while the gray ones are the boundary atoms which have no specified structure type. Following the pattern of the gray atoms, there are two atomic layers highlighted by green lines, which are nearly flat (i.e., all atoms in the atomic layer are with nearly the same z coordinate) and represent the two twin boundaries and have a TD between them. The structural reason for these two different TD configurations is that the two nearest-neighboring Mg atoms at CTB are not equivalent, and the step can be at either of them.

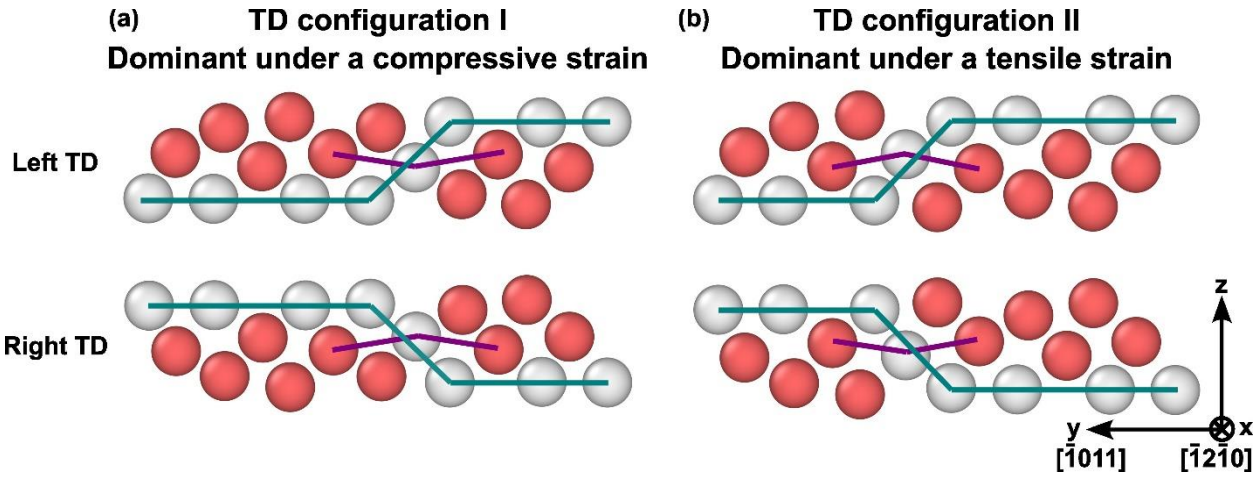


Figure 4.9. Two prevalent TD configurations under (a) compressive strain and (b) tensile strain. Atoms are colored based on their local structural environment. Green and purple lines are added as a guide to the eyes to show the difference between the two configurations.

The parity of atom number of the red and magenta dots in Figures 4.8(a)-(d), which means the position of the dislocation core of the TD, indicate which TD configuration is at the specific replica – whether the TD is at the atom with an odd or even index indicates which TD configuration it is. Energetically, the two TD configurations are different, and each would be preferred under different stress fields. While there is no stress applied to the system, Figure 4.8(a) shows it is possible to observe both two configurations during the migration process. Under a compressive strain, Figure 8(c) shows configuration A is dominant while under a tensile strain, Figure 4.8(d) shows configuration B is preferred.

It is shown in Figure 4.2(a) that the MEP curve of 2% compressive strain appears to fluctuate especially at the stage of TD migration. The fluctuation results from the switch between the two TD configurations and indicates the potential energy difference between the two configurations. Figure 4.8(e) simply takes the MEP curve of 2% compressive strain with labels as an example. The highlighted points in Figure 4.8(e) are replicas with local potential energy maximum. They correspond to the circles with the same color in Figure 4.8(e) and are the replicas where one of TDs has a different configuration different from the dominant configuration. The non-dominant TD configuration is of higher energy and thus is not energetically preferred under a certain loading. A similar fluctuation in the MEP is also seen but with lower amplitude when there is no normal strain, indicating the two configurations may be of a comparable energy value when the normal strain approaches 0. On the contrary, there is no such fluctuation in the MEP curve if the normal strain turns 2% tensile because configuration B with lower energy is observed at almost all the replicas during the stage of TD migration. Apparently, the potential energy difference between the two TD configurations is larger when the compressive strain or the tensile strain increases. From those cases varying the shear stress, it appears that the shear stress would not result in any significant preference on the two configurations.

### 4.6. Conclusions

This NEB-based study reveals a systematic stress-dependent energy barrier calculation for CTB migration. We find that while applying a shear stress, unsurprisingly, lowers down the energy barrier and thus boosts CTB migration, a non-glide stress changes the energy barrier. When the shear stress is non-zero, thereby inducing an asymmetry in the MEP and driving CTB migration, a compressive stress can reduce the energy barrier and the CRSS, and a tensile stress can increase

it. Assuming the Arrhenius equation applies, the rate of CTB migration is shown to be proportional to the ratio between the TRSS and the non-glide stress dependent CRSS to the power of a constant around 5. We note that the model considering the impact of the non-glide stress can be used to predict the twinning behavior under a complex stress field.

In addition to the energy barrier, the migration mechanism is also revealed by the structural evolution during CTB migration, especially that of TDs. While the migration mechanism does not change with the imposed stress, the dominant TD configuration may be different upon either tensile or compressive stress because one of the two possible TD configurations is more energetically favorable. On the other hand, the TD configuration itself in the intermediate state does not match with the widely reported TD configuration for $\{10\bar{1}2\}$ twin boundary and has a smaller and non-constant Burgers vector at every applied stress. It shows that the local reorientation during the CTB migration process does not complete as the TD passes through. Other than the behavior of TDs, the bulk atom displacement before TD nucleation and after TD recombination is also important to activate/conclude the CTB migration. We believe that these findings complement the current understanding of the TD configuration. Future studies will also focus on migration of the incoherent twin boundary and twin boundary with segregation where interactions between TD and other defects are possible.

# Chapter 5: Twin Nucleation from Disconnection-dense Sites between Stacking Fault Pairs in a Random Defect Network

## 5.1. Abstract

Deformation twinning, an important plastic deformation mode, critically influences the strength and ductility of Mg. As such, a fundamental understanding of twin nucleation will provide us with important insight into the conditions that favor the onset of this deformation mode. To reveal the twin nucleation mechanism, we construct a defect network without making assumptions about the types and relative densities of dislocations present. The generated defect network features a high density of $I_1$ stacking faults as well as disconnections between them. Deformation modeling results suggest that this structure enables a twin nucleation event from disconnection-dense sites between $I_1$ stacking faults pairs. By probing twin nucleation and early-stage growth inside of the random defect network, we propose a geometry-based twin variant selection rule as well as a pure-shuffle twin nucleation and early-stage growth mechanism underpinning twinning in Mg.

## 5.2. Introduction

Mg-rich alloys are of interest as structural materials, due to their low densities and great potential for weight savings. However, their low strength and limited formability at room temperature have led to concerns regarding reliability and manufacturability [1]. These undesirable properties are attributable to the limited number of slip modes that can be easily activated during plastic deformation and the relative ease of twinning, a unidirectional deformation mode, in hexagonal

close packed (hcp) structure. Depending on the type of twin, deformation twinning can accommodate either *c*-axis contraction or extension but not both. To date, numerous studies have focused on uncovering the mechanisms that govern twin nucleation, as well as early-stage twin growth following nucleation, in hexagonal close packed metals like Mg and its alloys [23,47,74,86,113]. Twin nucleation typically occurs much too rapidly for direct observation via electron microscopy techniques, making it challenging to understand all of the possible ways and situations in which twins can form [16]. Therefore, there is a lack of scientific understanding on precisely how twinning occurs, and hence numerous theories and mechanisms have been proposed to explain twin nucleation and establish the conditions that enable this event [16,26–29,32,33,138]. Most of these proposed mechanisms pertain to heterogenous nucleation or defect-assisted twin nucleation since homogenous nucleation requires stresses that can be as high as the theoretical strength of the material to be activated [15].

Most conventional defect-assisted twin nucleation theories postulate that pre-existing dislocations may undergo dissociation or recombination to generate a type of precursor structure (e.g., single- or multi-layer stacking fault) for deformation twins, which assists the development of a twin nucleus [15]. In the case of the $\{10\bar{1}2\}$ twin in Mg, multiple (instead of a single) twinning disconnections (TDs) $\frac{1}{15} < 10\bar{1}\bar{1} > \{10\bar{1}2\}$ are most likely to be the precursor and facilitate the twin nucleation by simultaneously gliding [26]. This type of TD-induced $\{10\bar{1}2\}$ twin nucleation is also referred to as shear-shuffle mechanism [16] because the atomic displacement field during the TD-facilitated lattice reorientation contains both shear and shuffle components [15,139]. In the presence of a stress concentration, multiple TDs may form via the combination of a basal <**a**> dislocation and a pyramidal-I <**c**+**a**> dislocation [27], the dissociation of edge <**c**> and mixed <**c**+**a**> dislocations [28], or the interaction between a basal dislocation and a $\{11\bar{2}1\}$ twin [29].

The pure-shuffle twin nucleation mechanism postulates that atomic shuffling, a non-affine (i.e., the displacements cannot be completed solely by a linear transformation) and diffusionless atomic displacement, akin to that involved in the martensitic transformation, causes twin nucleation. While defects are still needed for the atomic shuffling, this mechanism requires far fewer TDs, other dislocations or stacking faults to be present, if any. The shuffling-induced twin nuclei feature: (1) a basal-prismatic (BP) and prismatic-basal (PB) transition and subsequently BP and PB interfaces bounding the twin embryo, and (2) a deviation of the misorientation angle from the ideal 86.3° to approximately 90° which complies with the BP and PB transition. There are more direct observations supporting the pure-shuffle nucleation mechanism than any of the other proposed mechanisms [16,32–34]. In summary, the two possible twin nucleation mechanisms, shear-shuffle mechanism featuring the nucleation of precursor $\frac{1}{15} < 10\bar{1}\bar{1} > \{10\bar{1}2\}$ TDs via multiple possible dislocation reactions and pure-shuffle mechanism featuring a B-P or P-B transformation [30], may represent mutually competing pathways that lead to the formation of twins, depending on the microstructures and stress conditions that are present.

In this study, we use the following molecular dynamics (MD) simulations procedures to shed light into twin nucleation and the associated preferred twin nucleation sites, as well as into early-stage twin growth behavior. We use a random defect network that can be considered a facsimile of a real Mg sample containing a large number of crystal defects as follows. First, we construct a defect network without making assumptions of the types and relative densities of dislocations present using the method introduced by F. Sansoz [140]. The generated defect network features a high density of $I_1$ stacking faults as well as disconnections between them. Deformation modeling reveals that this structure enables an unusual twin nucleation event happening in disconnection-dense sites between stacking fault pairs. Second, by observing twin nucleation and early-stage twin

growth inside of this system, a geometry-based twin variant selection rule and a pure-shuffle twin nucleation mechanism are proposed.

### 5.3. Computational Methods

The atomic-scale mechanism responsible for $\{10\bar{1}2\}$ twin nucleation in pure Mg was investigated with the Large-scale Atomic/Molecular Massively Parallel Simulator (LAMMPS) [55], using MD with an embedded atom method (EAM) interatomic potential by Sun et al [141]. This potential provides accurate description of dislocation core structures and stacking fault parameters [29]. To enable the twin nucleation inside bulk Mg (i.e., without the assistance of free surfaces), lattice defects like dislocations are needed to offer sites for heterogeneous nucleation [15]. Consequently, a defect network was built following the method described in Ref. [140]. This method mimics the process of dislocation formation in quenched materials with supersaturation of vacancies and no explicit assumptions of dislocation types and proportions [142]. The initial configuration was a pure Mg cube containing 963,200 atoms with dimensions of 27.40 nm along the x-direction (i.e., $[11\bar{2}0]$), 27.60 nm along the y-direction (i.e., $[\bar{1}100]$) and 28.96 nm along the z-direction (i.e., [0001]). After energy minimization under periodic boundary conditions applied along all three dimensions, 20% of Mg atoms were randomly deleted from the Mg cube and a series of heat treatments was conducted under the isothermal-isobaric ensemble (NPT) ensemble with a Nosé-Hoover thermostat and a constant pressure of 0. The simulated heat treatment is schematically illustrated in Figure 5.1: equilibration at 300 K for 50 ps, heating from 300 K to 823 K (i.e., 100 K below the melting temperature of Mg) over 50 ps, annealing at 823 K for 50 ps, quenching from 823 K to 1 K over 50 ps and another equilibration at 1 K for 50 ps. We selected 1 K as the final

temperature to minimize thermal fluctuations and enable detailed atomic analysis. By varying the random seed controlling atom removal, we prepared different microstructures that aim to validate the generality of the randomized defect network and the resulting twin nucleation mechanism.

After the heat treatment, a notable feature of the atomic configuration, besides the dislocation and stacking fault network, was the presence of a non-negligible number of residual vacancies. These were filled as best as possible with Mg atoms to minimize the effect that residual vacancies may have on the twin nucleation mechanism. The Wigner-Seitz analysis [133] was done to label the vacancies and allow the process of vacancy filling. After that, the sample was first relaxed using energy minimization, then equilibrated using the NPT ensemble at 1K for 250 ps and finally deformed along the z-axis at an engineering strain rate of $10^9$ $s^{-1}$, a strain rate that was selected because it is widely used in simulating Mg deformation [29,143,144]. The canonical (NVT) ensemble with a Nosé-Hoover thermostat was used during deformation. For all the simulations, the timestep was set to be 5 fs. The snapshots of atomic configurations in this study are all visualized by OVITO [133].

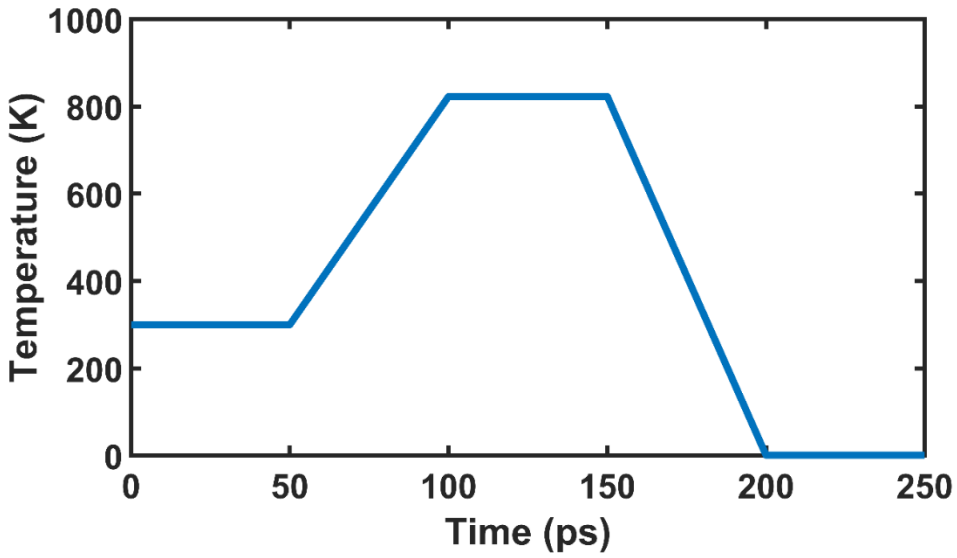

Figure 5.1. Temperature and time curve in thermal annealing simulation to generate a random dislocation network in a Mg single crystal with the *c*-axis coinciding with the z-axis of the simulation box and an initial porosity of 20%.

## 5.4. Results

### 5.4.1. Stacking fault network

Figure 5.2(a) shows the simulation cell prior to deformation. A complex and random network of defects was generated, and the corresponding dislocation density using dislocation analysis (DXA) in OVITO [145] is estimated to be on the order of $10^{17}$ $m^{-2}$, which is much higher than the dislocation density of heavily deformed metals (i.e., $10^{14} – 10^{15}$ $m^{-2}$) [142] and that of focused ion beam (FIB)-fabricated metallic nanopillars (i.e., $10^{15}$ $m^{-2}$) [140] and represents a highly defective region within a grain. DXA also shows the existence of almost all types of dislocations that have been frequently reported in Mg, including <**a**>, <**c**>, <**c**+**a**>, Shockley partial (or partial <**a**>), Frank partial and different types of partial <**c**+**a**> slip. The random generation of high-density dislocations enables the study of the interaction between stacking faults and a disconnection-dense structure resulting from these interactions. Figure 5.2(b) shows an overview of the defect network, containing plenty of $I_1$ stacking faults shown as single-atomic-layered face-centered cubic (fcc)-type defects, relatively fewer $I_2$ stacking faults, pre-existing twins, and a few residual vacancies. The most noticeable type of defects is the $I_1$ stacking fault that lies on the horizontal (0001) plane. Figure 5.2(c) shows results from the four parallel simulations which are consistent with those in Figures 5.2(a) and 5.2(b). Unlike isolated $I_1$ stacking faults that are bounded by Frank partials, $I_1$ stacking faults in this model are interconnected by disconnections. A similar but much simpler configuration has been only reported by C. He et al. [146] both via experiments and simulations in a cold-rolled Mg-Bi alloy – it has been argued that a long Frank partial bounded $I_1$ stacking fault

may interact with a basal <**a**> dislocation and result in a Shockley partial at the edge of a step structure connecting two $I_1$ stacking faults that are ½ c (i.e., one atomic layer) spaced from each other along the *c*-axis. However, in this study, the step height is not limited to ½ c, while the dislocation character of the disconnection is not necessarily only one Shockley partial.

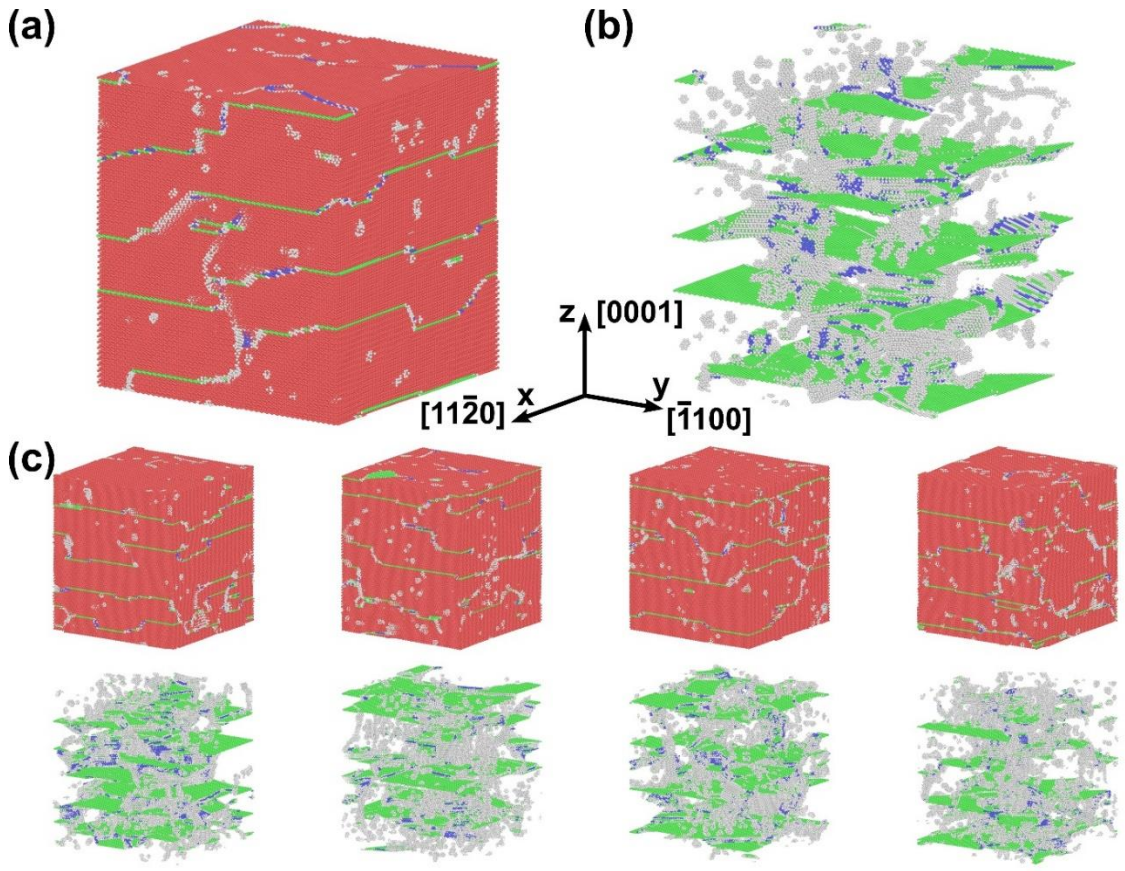


Figure 5.2. Atomic snapshots at zero strain (i.e., before deformation) (a) with hcp atoms shown, (b) without hcp atoms for clarity of the stacking fault network, (c) from the other four parallel simulations with the random seeds controlling the atom removal changed, both with (top row) and without hcp atoms (bottom row). Atoms are colored based on the polyhedral template matching algorithm in OVITO: red for hexagonal close packed (hcp), green for face-centered cubic, blue for body-centered cubic, and white for undefined local coordination structure. The color coding of atoms for the rest of this chapter also follows the same rule. Tension is applied along the z-direction.

Similar to the configuration reported by C. He et al. [146], we can formulate the stacking sequence mismatch and, therefore, the formation of the ½ c-high step as shown schematically in Figure

5.3(a). The Shockley partial represents the displacement of the atoms below the higher $I_1$ stacking fault with respect to those below the lower $I_1$ stacking fault. If this geometry is generalized by introducing a set of multiple Shockley partials layer-by-layer, a more complicated structure of disconnections between two $I_1$ stacking faults can be proposed. In Figure 5.3(b), two opposite Shockley partials participate in the formation of a two-layer high disconnection. While the first Shockley partial displaces the atoms beneath the higher $I_1$ stacking fault, the second opposing one may shift those beneath the first Shockley partial back. The overall effect is that only the stacking sequence of one layer in the middle changes from C to A, and the rest of the layers are arranged the same way as if there exists no disconnection but an ideal $I_1$ stacking fault. Similarly, multi-layer disconnections may be constructed by a series of Shockley partials, as shown in Figures 5.3(c) and 5.3(d). The Shockley partials are equally spaced layer-by-layer with nearest neighbors having opposite Burgers vectors. Theoretically, the arrangement of the Shockley partials can accommodate the stacking sequence mismatch between two $I_1$ stacking faults that are arbitrarily far away from each other while the overall Burgers vector of the disconnection is reasonably small to not further decompose.

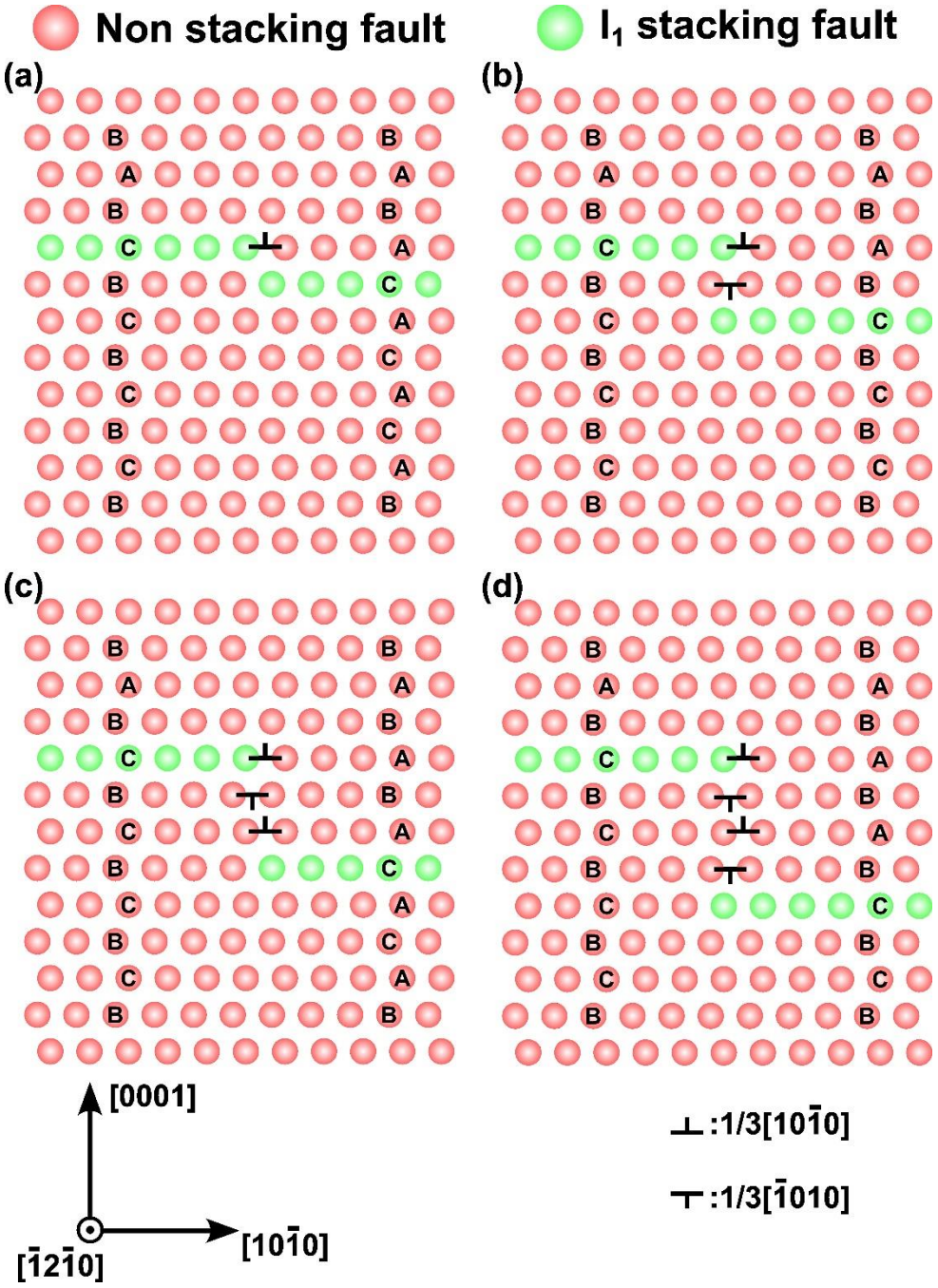


Figure 5.3. A proposed formation mechanism for a (a) single-layer-high disconnection, (b) double-layer-high disconnection, (c) (2n-1)-layer-high disconnection and (d) 2n-layer-high disconnection between two bounding $I_1$ stacking faults. The formation is enabled by the displacement along one (for (a)) or multiple mutually opposite Shockley partials in sequence (for (b)-(d)). The Shockley partial array is also plotted as well as the resultant change in stacking sequence. Note this is a schematic diagram with unrelaxed atomic positions.

Figure 5.4 shows examples of disconnections that connect the neighboring $I_1$ stacking faults. All of the disconnections are labeled with their step heights in terms of the number of atomic layers. The two disconnection sites that later allow for twin nucleation are highlighted in orange. For given two $I_1$ stacking faults, such as the highlighted two in Figure 5.4, there are multiple ways the disconnection(s) in between can arrange themselves. A disconnection may decompose into multiple disconnections with smaller step heights. As a result, there must be a few smaller $I_1$ stacking faults positioned in the middle to connect these decomposed disconnections with smaller step heights, as indicated by the five disconnections underscored with a dashed line compared to those marked by a solid line. On the other hand, these disconnections with larger step heights are stable because the horizontal spacing between the two bounding $I_1$ stacking faults is very small, usually less than 5*a* where *a* is the lattice constant of Mg, making the decomposition less likely to happen. An example with such a small horizontal spacing, which is the disconnection denoted by the orange "4" in Figure 5.4, is illustrated in the inset. Interestingly, it has been found that these disconnections with larger step heights usually have a body-centered cubic-type local atomic configuration.

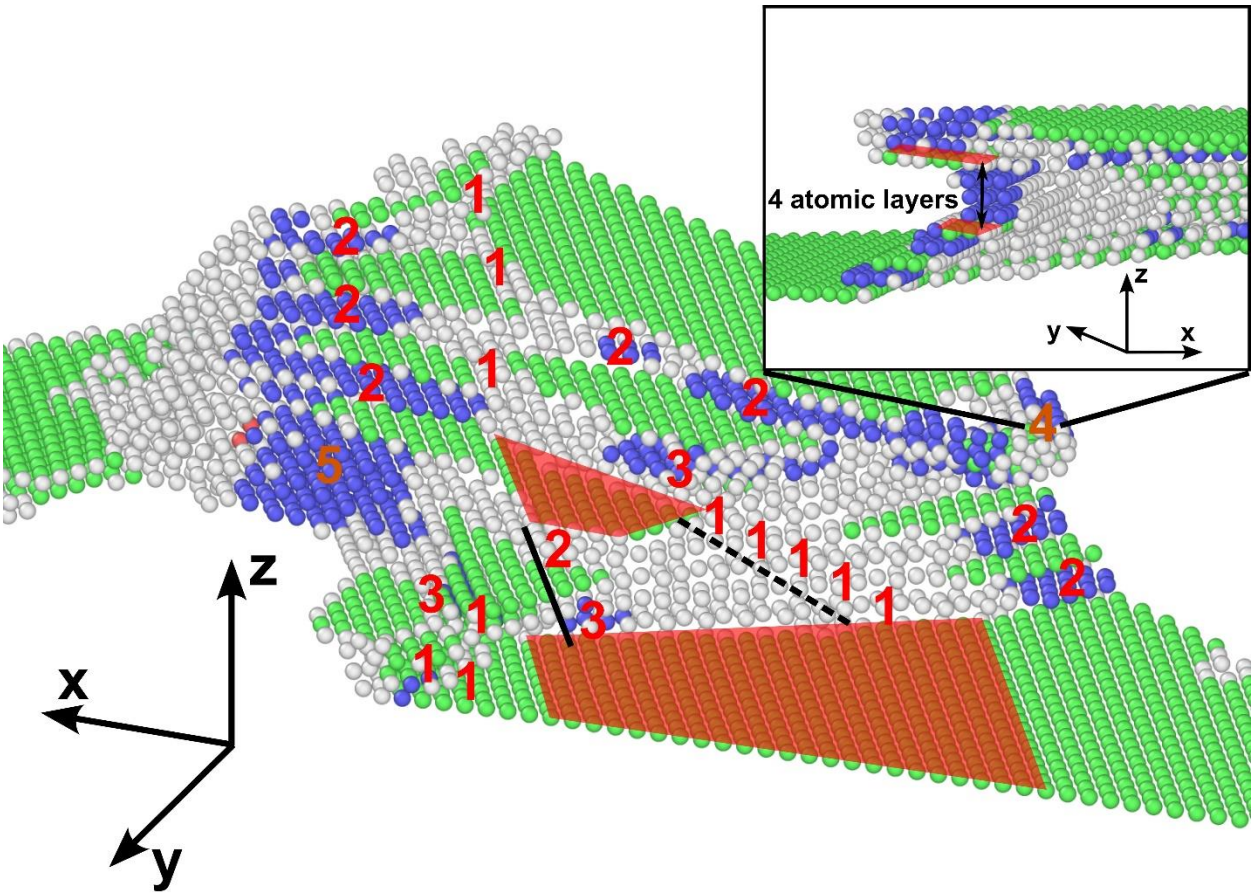


Figure 5.4. The atomic snapshot of a region with dense disconnection. The step height of each disconnection is labeled in the number of atomic layers, with 1 corresponding to a height of ½ c. Numbers are colored according to whether there is a {10-12} twin nucleating at the corresponding site: orange for the nucleation site and red for the non-nucleation site. Between the highlighted two bounding $I_1$ stacking faults, a region containing "decomposed" disconnections with lower step heights as well as smaller $I_1$ stacking faults is marked by a dashed line, while another region containing disconnections with larger step heights is also marked by a solid line as a comparison. An enlarged view of the top-right 4 atomic-layer-high disconnection is shown in the inset with its step height and the horizontal spacing of the bounding $I_1$ stacking faults highlighted.

### 5.4.2. Twin statistics

The analysis of twin statistics was used to characterize twin evolution quantitatively during deformation and provide insight into twin nucleation and subsequent growth. Through the local lattice orientation calculation in OVITO [137], twin clusters with at least 20 atoms are sorted out

for twin statistical analysis. The threshold of twin size is selected so that very small atom clusters that are erroneously labelled as twins due to the instability of the algorithm will not be counted. Figure 5.5 shows the twin statistics using 4 descriptors – twin volume fraction, the number of twins, twin variant fraction, and the aspect ratio. The data are obtained from 5 parallel simulations deletional produced the same way but with slightly different defect networks. The analysis goes until an engineering tensile strain of 5%, because fracture starts to occur at larger strains.

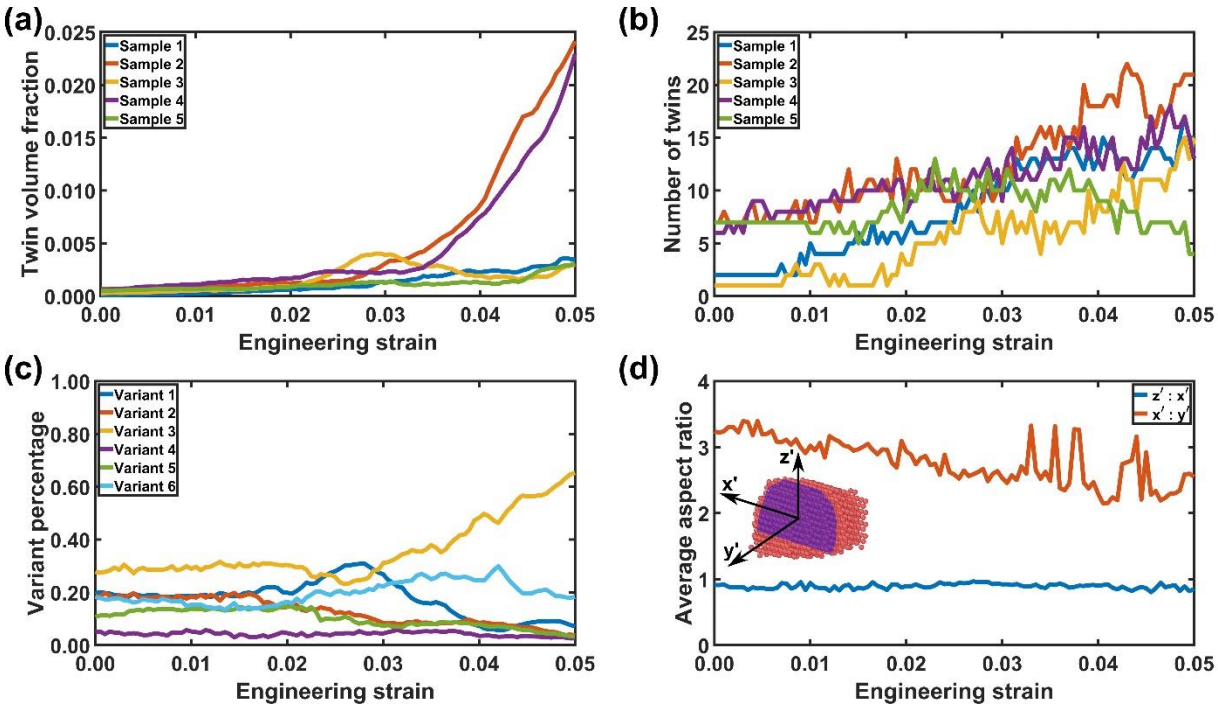


Figure 5.5. (a) Twin volume fraction evolution for each sample. (b) Twin amount evolution for each sample. (c) Twin variant distribution averaged across all 5 samples. (d) Average aspect ratio evolution across all 5 samples in two ratios (z':x' and x':y') with the inset showing a local twin coordinate system and defining x'-, y'- and z'-directions: x' for the zone axis shared by the basal plane in the matrix and in the twin, y' for the in-plane perpendicular direction to the zone axis, z' for exactly the z-direction of the simulation box. All these parameters are plotted as functions of engineering strain $\varepsilon_{zz}$.

Twin volume fraction evolution as a function of the engineering tensile strain, shown in Figure 5.5(a), reveals that two different modes of twin evolution exist. One features a critical strain of ~3% after which the twin volume fraction sharply increases, like Samples 2 and 4. The other shows

a less significant increase of the twin volume fraction, as in Samples 1, 3 and 5. The twin growth can be even locally reversible, as evidenced by a drop in the twin volume fraction for Sample 3, because some twin configurations are energetically unstable and therefore likely to de-twin.

The number of twins shown in Figure 5.5(b) generally increases as deformation continues. However, fluctuations in the curves indicate that changes in the number of twins result not only from nucleation, but also from twin coalescence or de-twinning. In this particular case, de-twinning results from twin embryos whose subcritical size makes them unstable.

The distribution of twin variants, averaged across all samples and illustrated in Figure 5.5(c), reveals an unbalanced distribution of 6 twin variants. Mechanically, the 6 variants of the $\{10\bar{1}2\}$ twin should be equally probable because the tension field was applied along the symmetry axis of the hcp crystal (*c*-axis). However, the observed disparity indicates that the twin variant is dictated by other structural reasons and hence that a variant selection rule may exist. Within the same twin, the variant indicator can be different but only within the mutually co-zone variant pair (i.e., Variant 1-Variant 4, Variant 2-Variant 5, Variant 3-Variant 6 in Figure 5.5(c)) and indicate the degeneracy of co-zone variants, which means at stages of twin nucleation and early-stage growth, co-zone twins may not be clearly distinguished. This degeneracy agrees with a prior study by Y. Hu et al. [25], which reveals that the twin embryo may undergo a stochastic incubation stage when co-zone twin variants are not yet determined until the twin embryo reaches a significant size in the deterministic growth stage.

The twin morphology is indicative of the nucleation mechanism as well as the dominant growth direction of $\{10\bar{1}2\}$ twins. The twin lengths along 3 dimensions, the zone axis shared by the basal plane in the matrix and in the twin (labeled as x' and referred to as the zone axis hereinafter), the in-plane perpendicular direction to the zone axis (y'), and the z-axis of the simulation box (z'), of

a $\{10\bar{1}2\}$ twin are shown in the inset of Figure 5.5(d) and estimated using four times the standard deviation of each coordinate of atoms (i.e., their x', y' and z' values) [52]. Figure 5.5(d) shows the evolution of two aspect ratios: z':x' and x':y'. The ratio z':x' is close to 1 and only slightly decreases as the applied strain increases, which implies that the growth along these two dimensions occurs concurrently and with similar rates. The ratio x':y' is always larger than 2 and generally decreases as deformation continues. This means the growth along the y'-direction is impeded relative to that along the x'- and z'-directions, especially for low strain levels. Hence, the results in Figure 5.5(d) indicate that the geometry of the twins in the system is plate-like.

### 5.4.3. Twin nucleation and early-stage growth during deformation

The analysis of twin statistics provides an overview of the twin evolution and therefore helps understand a few key events during deformation. In this section, the features and rules that may be active throughout the process of twin nucleation and early-stage growth will be discussed.

Prior to discussing results, it is important to note that there are a few pre-existing $\{10\bar{1}2\}$ twins present even before deformation, although these twins are far fewer than the deformation-induced ones. These pre-existing twins are induced by the vacancy filling and the equilibration that follows because no pre-existing twins are observed in the case without these two processes. There is no significant difference in twin behavior (e.g., nucleation site, growth rules) between the pre-existing twins and the deformation-induced ones. Consequently, in the section that follows, pre-existing twins will not be discussed separately.

In our results, twin nucleation is observed to consistently occur only at some of the disconnections between two $I_1$ stacking faults. A twin nucleation event is illustrated in Figure 5.6 with the atom snapshots before and after the nucleation. As shown in the inset of Figure 5.6(b) by four vertical

basal planes in the twin, the twin embryo right after the nucleation is a 90° $\{10\bar{1}2\}$ twin and the dominant boundary between the twin domain and the matrix is the BP/PB interface, which indicates the critical role of the P-B transformation (i.e., the prismatic plane in the matrix is transformed into the basal plane in the twin) on the twin nucleation. Notably, the formation of a coherent twin boundary is not observed during deformation. From an overview of all twin embryos, there seems to be a critical disconnection height that allows for twin nucleation. – the threshold value is 4 atomic layers, while the maximum height of disconnections that allows for twin nucleation is 21 atomic layers.

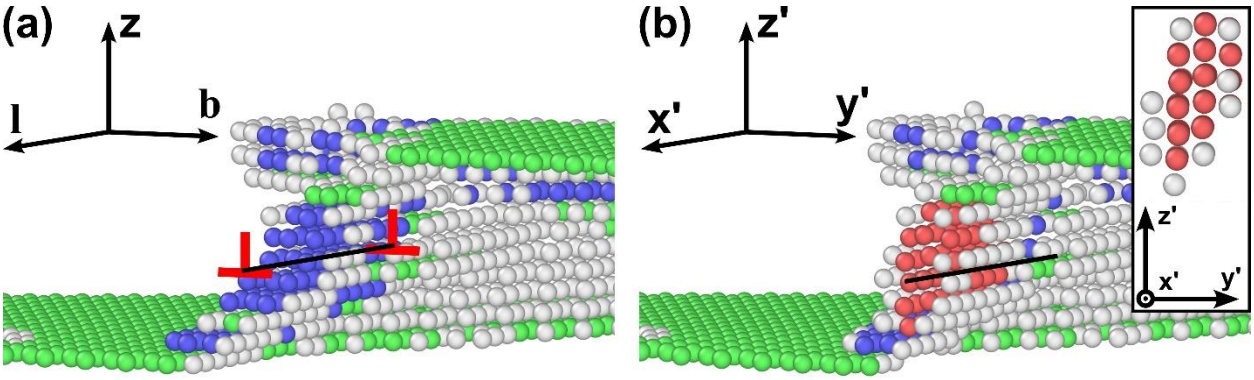


Figure 5.6. Atomic snapshots of a twin nucleation site (a) right before the nucleation and (b) right after the nucleation. The inset of (b) shows this twin embryo along the x'-axis consisting of four vertical basal planes. The black lines and the coordinate systems indicate the coincidence of the dislocation line of the edge Shockley partial and the zone axis shared by the basal plane in the matrix and in the {10-12} twin embryo. The axes of the coordinate systems have the following meaning: b for the Burgers vector of the Shockley partial, l for the line direction of the Shockley partial, z for the z-direction of the simulation box. The x', y' and z' coordinate system has the same meaning as defined in Figure 5.5.

The unbalanced twin variant frequency is evaluated by statistical analysis and indicates a geometrical reason behind it. Following the proposed formation mechanism of disconnections where the twin nucleation occurs, shown in Figure 5.3, the edge Shockley partial also has 6 variants with 3 unique line directions due to the 6-fold symmetry of the hcp structure. By observing the

nucleation of every twin embryo, the variant selection follows simply from the geometrical constraint that in order for the dissociation event to occur, the zone axis must coincide with the dislocation line of edge Shockley partials. This alignment is also illustrated in Figure 5.6. In other words, the 90° P-B transformation must happen on the plane spanned by the z-direction and the line direction of the disconnection in Figure 5.6(a), which coincides with the x'z' plane in Figure 5.6(b), and later other parallel crystal planes. Considering the twin morphology statistics, the P-B transformation happens faster along the x'-axis and much slower along the z'-axis, possibly due to the confinement induced by two bounding $I_1$ stacking faults. Also, the degeneracy of co-zone twin variants revealed by the statistical analysis is a direct consequence of the P-B transformation because the crystallographic orientation of co-zone twins will be the same after this 90° transformation.

Early-stage twin growth is defined as the significant size increase of the twin embryo that occurs immediately following twin nucleation, during which the twin size only slightly changes. Generally, the early-stage twin growth process can be divided into two substages. In the first substage, where the twin embryo grows from the state shown in Figure 5.7(a) to Figure 5.7(b), the transformed basal plane further expands but is still limited by two $I_1$ stacking faults between which the disconnection is positioned. In the meantime, the twin also grows along the y'-direction as more P-B transformations occur (denoted by three adjacent basal planes in the twin highlighted in Figure 5.7(b)) but much more slowly than along the x'-direction, the zone axis. In the second substage where the state in Figure 5.7(b) further evolves to that in Figure 5.7(c), the twin domain will also significantly expand along the z-axis and break the limit imposed $I_1$ stacking by faults by reorienting the atoms in the vicinity of them. The dimensions along the three axes x', y', and z' of this twin are also shown in Figure 5.7(d) under different strain levels as well as approximate

boundaries of the two substages. The twin growth behavior indicates that the early-stage twin growth matches the pure-shuffle mechanism instead of the shear-shuffle mechanism, since the twin growth is still facilitated by P-B transformations and the growth along the twinning direction is not observed.

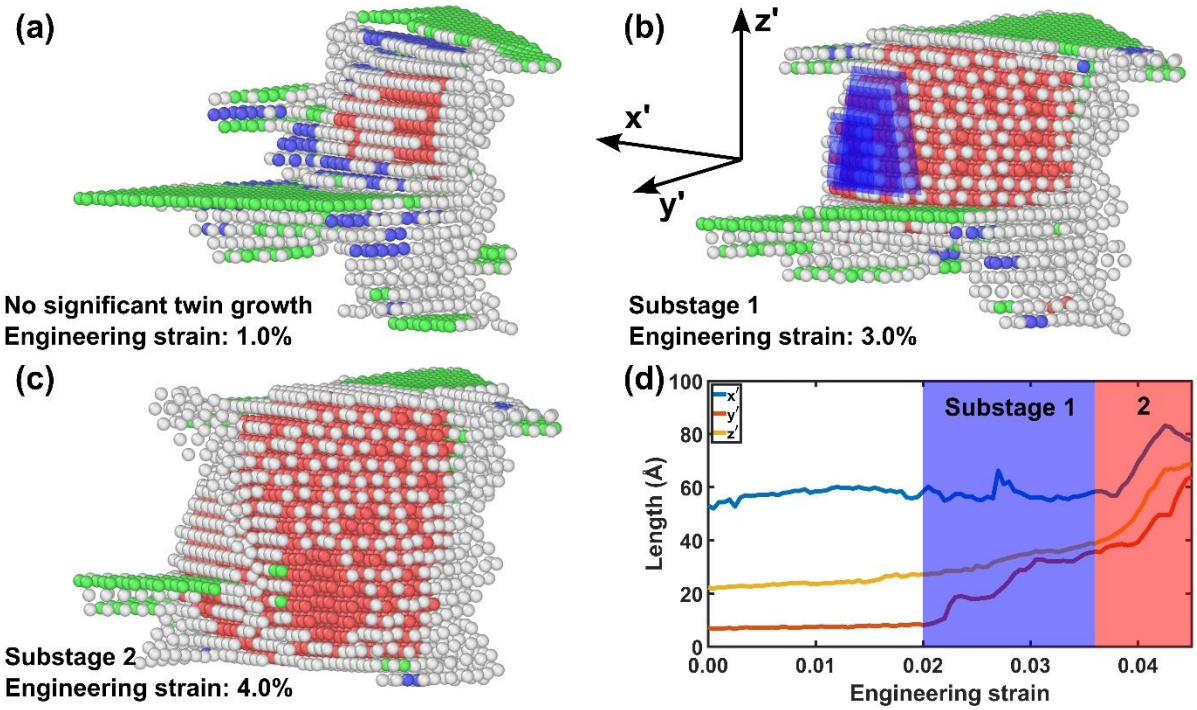


Figure 5.7. Atomic snapshots showing the two substages after the twin nucleation. (a) for the stage where no significant twin growth occurs before the two substages, (b) for substage 1, and (c) for substage 2 (as noted in (d)). Three adjacent transformed basal (B) planes in twin from prismatic (P) planes in matrix are highlighted in (b). (d) Twin lengths along the 3 axes in the local twin coordinate system, x', y' and z', is plotted as functions of engineering strain $\varepsilon_{zz}$. An approximate range of substage 1 and 2 is labelled, respectively, with substage 2 featuring a significant rise of z' length of the twin embryo.

Comparative simulations have also been done by deleting 15% Mg atoms instead of 20% while keeping all other parameters constant. Interestingly, in this case the only stacking fault type observed is the $I_2$ stacking fault, which indicates the removal of abundant Mg atoms is a prerequisite to forming the $I_1$ stacking fault. The $I_2$ stacking fault is bounded by Shockley partials as normal and is also interconnected but by an <**a**> dislocation that can be formed by the

combination of two Shockley partials. When the simulation box was deformed the same way, no deformation twins are observed until sample fracture. Similarly, another comparative simulation with 18% atom deletion was conducted. In this case, $I_1$ stacking faults are observed but with a smaller number density. The $\{10\bar{1}2\}$ deformation twin nucleates near the disconnection between two neighboring $I_1$ stacking faults, as in the case of 20% atom deletion, but with a lower number frequency due to the presence of only sparse $I_1$ stacking faults. These comparisons, as well as the parallel simulations that randomize the atom removal, validate that the most preferable twin nucleation site should be the disconnection between neighboring $I_1$ stacking faults, regardless of atom deletion percentage and the randomized structure of the stacking fault network.

### 5.5. Outlook and conclusions

This work describes and analyzes twin nucleation at disconnection-dense sites between two $I_1$ stacking faults inside a complex defect network. By mimicking the dislocation formation in quenched materials with supersaturation of vacancies, a random defect network containing different types of dislocations, stacking faults, and disconnections is generated by annealing and quenching of a porous Mg in molecular dynamics simulations, before a tensile deformation was applied. Our results indicate that the unique disconnection-dense sites are favorable for twin nucleation. These sites allow the P-B transformation to first occur on the plane spanned by the dislocation line of the disconnection and the *c*-axis of the matrix and later other parallel planes. This nucleation mechanism also results in the variant selection rule that sets the zone axis shared by the basal plane in the matrix and in the $\{10\bar{1}2\}$ twin to coincide with the dislocation line.

Early-stage growth of the $\{10\bar{1}2\}$ twin after its nucleation has also been observed within an engineering strain of 5% along the *c*-axis. The twin growth can be categorized into two substages. During the first substage, the growth is limited by two bounding $I_1$ stacking faults and anisotropic as the growth appears to be fastest along the y'-direction. The second substage occurs when the limitation imposed by neighboring stacking faults is no longer present. Therefore, the growth is less anisotropic as the $\{10\bar{1}2\}$ twin can propagate along the z-direction more easily at this stage.

Based on our study, we propose a possible pure-shuffle mechanism for the $\{10\bar{1}2\}$ twin nucleation and early-stage growth, especially in a dislocation-rich environment. However, since the structure of the disconnection between two $I_1$ stacking faults has heretofore not been reported, it remains unclear whether and how a similar structure can be formed in experiments when the dislocation density is much smaller than the level that can only be reached by molecular dynamics simulation. The energetics also need further study to explain why these disconnection-dense sites are energetically favorable for the observed twin nucleation.

## Chapter 6: Conclusions and Future Work

In this dissertation we studied multiple scenarios where the stress-strain fields influence microstructure, paying particular attention to twin behavior in Mg and Mg alloys under different conditions. These fundamental correlations between external controllable parameters and microstructural response modulate the mechanical properties of Mg and hence provide an opportunity for twin-based engineering which ultimately may be used for the simultaneous optimization of strength and ductility of Mg. Below, we summarize the key conclusions for each chapter in this dissertation.

- Chapter 2: The EBSD-based statistical analysis reveals multiple correlations between grain-scale microstructural characteristics and $\{10\bar{1}2\}$ twin behavior. For instance, the positive correlation between grain size/grain perimeter and the probability of having at least one twin in the grain is confirmed. The Mg-Y alloy with higher Y concentration experiences a lower TAF and a slower twin thickening under the same strain level, which is more attributable to the higher Y concentration rather than to a weakened texture. Most meaningfully, this study validates the notion that EBSD is a promising data source to perform high-throughput analyses of microstructure and its evolution.
- Chapter 3: Room temperature deformation-induced Y segregation in the Mg-3Y solid solution alloy is characterized through HAADF-STEM and EDS. The segregation is observed at lattice dislocation cores, alternating tensile sites along $\{10\bar{1}2\}$ CTBs and adjacent to BP facets in the form of Y clusters. Atomistic simulations further show energetic reason of the segregation and the pinning effect imposed by the segregated Y.

Overall, this study indicates that deformation-induced segregation can make a significant difference to the mechanical behavior and the microstructure evolution in Mg alloys.

- Chapter 4: The influence of applied stress-strain fields on the $\{10\bar{1}2\}$ CTB migration is systematically investigated using NEB that calculates its energy barrier and MEP. While the shear stress decreases the energy barrier and boosts CTB migration, the non-glide stress, which does not contribute to the TRSS, lowers down the energy barrier when it is compressive. Based on the relationship between the stress field and the energy barrier, the rate of CTB migration is shown to be proportional to the TRSS to CRSS ratio to the power of ~5. Microstructurally, several features and configurations during CTB migration are highlighted to complement the current understanding of this process from the perspective of the MEP, including (1) the bulk atom displacement before TD nucleation and after TD recombination; (2) the Burgers vector of the observed TD is much smaller than the widely reported value; (3) different dominant TD configurations upon compressive and tensile non-glide stress.
- Chapter 5: The $\{10\bar{1}2\}$ twin nucleation from the disconnection-dense sites between $I_1$ stacking fault pairs is highlighted inside a randomly generated defect network without making assumptions of the types and the proportion of dislocations. A pure-shuffle mechanism featuring the P-B transformation for twin nucleation and subsequent early-stage growth is observed. A geometry-based twin variant selection rule is also established.

In this dissertation we find that the presence of stress-strain fields critically influences the behavior of deformation twins, including twin evolution at the micron scale during deformation,

coherent twin boundary migration, and twin nucleation along with subsequent early-stage growth. The findings reveal that not only the presence of stress-strain fields, but also many other micro- or nano-structural characteristics, such as grain size, crystallography, alloying element concentration and pre-existing defects can be engineered to modulate the formation, propagation, and growth of deformation twins in Mg. However, to properly implement the idea of twin-mesh engineering in Mg and Mg alloys, additional research is required; some ideas of this future work are listed below.

1. Following the EBSD-based statistical study which successfully established correlations between grain-level microstructural characteristics and twin behavior in Chapter 2, it is more desirable to build some multiple-to-one correlations that allow for a more direct prediction of whether a twin will be generated inside a given grain with all information (such as grain size, the size and the crystallographic orientation of neighboring grains) known. In recent years, machine learning has been widely adopted into the field of materials science and has contributed to some notable accomplishments, including property prediction of a given material or structure [147], image processing of TEM micrographs [148] and boosting of the accuracy and calculation efficiency of MD [149]. Applying machine learning to the analysis of EBSD data is anticipated to help predict the twin nucleation/growth probability.

   There have been some preliminary studies done by our collaborators from Prof. Stacy M. Copp's Research Group. Principal component analysis has been performed to examine the relative essentiality of each parameter in predicting the twinning probability and several machine learning algorithms have been adopted to train the predictor with a reasonable accuracy. The next step will be to further tune the model based on materials

science knowledge, for example, to add Schmid factor as a feature. The more reliable prediction of twinning can facilitate the controlling and engineering of the twin mesh in a polycrystal Mg alloy.

2. The room temperature deformation-induced Y segregation at faceted $\{10\bar{1}2\}$ twin boundaries in a solid solution Mg-3Y alloy in Chapter 3 was observed, but this phenomenon was simply justified using a statics analysis that showed a lower overall potential energy after the segregation and the mechanism or the diffusion pipeline behind the segregation is still not clear. Two questions should be addressed: first, along which pathway does Y segregate to twin boundaries under an applied load? second, among all the possible segregation mechanisms, which one is dominant? Once the segregation kinetics is better understood, by either enabling or disabling such a segregation pathway through alloy design or heat treatment, segregation at twin boundaries can be accelerated or decelerated to modulate twin behavior and therefore the mechanical properties.
   To reveal the segregation mechanism, two possible methods should be considered. One of them is accelerated molecular dynamics that allows for a longer simulated time for diffusion analysis. The other is to characterize the spatial distribution of Y dopants in the vicinity of twin boundaries with methods which have an atom-scale spatial resolution (e.g., atom probe tomography, electron energy loss spectroscopy). There are several hypotheses of the fast segregation pathway inside the defective crystal under deformation to be validated: (1) Y dopant atoms mostly stay still in the bulk crystal and get dragged by a moving twin boundary. After that, Y may be carried by the moving twin boundary as it continues to migrate; (2) Dislocations may interact with twin boundaries and then allow Y dopant atoms inside the dislocation core to diffuse towards twin boundaries through

pipe diffusion; (3) Dislocations may drag Y dopant atoms in the bulk crystal as in hypothesis (1) and carry them to twin boundaries during glide via cross-core diffusion.

3. The finding of twin nucleation from disconnection-dense sites between $I_1$ stacking fault pairs reported in Chapter 5 is quite unexpected, but such a nucleation site has not been reported so far in experiments due to the ultrahigh dislocation density in the MD model. Consequently, it is important to provide experimental evidence for the existence of this particular nucleation mechanism. A possible method to validate it may be to generate locally dislocation dense sites in a nanopillar under certain heat treatments and then deform it in a way that favors twin nucleation for further TEM characterization of the twin embryo. Also, the energetics of this nucleation event deserve more study to answer why these disconnection-dense sites are preferrable for twin nucleation.
4. Inspired by other studies which observe the twin mesh-like twin networks, it may be meaningful to pay special attention to certain materials or mechanical testing methods. For example, deformed Mg-Li based alloys show a high density of twins featuring a small thickness [45] and under a compression with GPa-scale hydrostatic pressure, the Mg-Li alloy even allows for the generation of parallel nanotwins with nanoscale spacing and large number density [72]. Focusing on Mg-Li alloys with extreme deformation conditions seems an interesting starting point to realize the idea of twin-mesh engineering since the mechanism causing this phenomenon is not fully understood.

## References


[1] J.F. Nie, K.S. Shin, Z.R. Zeng, Microstructure, Deformation, and Property of Wrought Magnesium Alloys, Metall Mater Trans A. 51 (2020) 6045–6109. https://doi.org/10.1007/s11661-020-05974-z.

[2] A. Imandoust, C.D. Barrett, T. Al-Samman, K.A. Inal, H. El Kadiri, A review on the effect of rare-earth elements on texture evolution during processing of magnesium alloys, Journal of Materials Science. 52 (2017) 1–29. https://doi.org/10.1007/s10853-016-0371-0.

[3] T.B. Abbott, Magnesium: Industrial and Research Developments Over the Last 15 Years, Corrosion. 71 (2014) 120–127. https://doi.org/10.5006/1474.

[4] U. Masood Chaudry, S. Tekumalla, M. Gupta, T.-S. Jun, K. Hamad, Designing highly ductile magnesium alloys: current status and future challenges, Critical Reviews in Solid State and Materials Sciences. (2021) 1–88. https://doi.org/10.1080/10408436.2021.1947185.

[5] D. Zhang, H. Wen, M.A. Kumar, F. Chen, L. Zhang, I.J. Beyerlein, J.M. Schoenung, S. Mahajan, E.J. Lavernia, Yield symmetry and reduced strength differential in Mg-2.5Y alloy, Acta Materialia. 120 (2016) 75–85. https://doi.org/10.1016/j.actamat.2016.08.037.

[6] T. Mayama, K. Aizawa, Y. Tadano, M. Kuroda, Influence of twinning deformation and lattice rotation on strength differential effect in polycrystalline pure magnesium with rolling texture, Computational Materials Science. 47 (2009) 448–455. https://doi.org/10.1016/j.commatsci.2009.09.009.

[7] J. Hirsch, T. Al-Samman, Superior light metals by texture engineering: Optimized aluminum and magnesium alloys for automotive applications, Acta Materialia. 61 (2013) 818–843. https://doi.org/10.1016/j.actamat.2012.10.044.

[8] Q. Yu, L. Qi, R.K. Mishra, J. Li, A.M. Minor, Reducing deformation anisotropy to achieve ultrahigh strength and ductility in Mg at the nanoscale, Proceedings of the National Academy of Sciences. 110 (2013) 13289–13293. https://doi.org/10.1073/pnas.1306371110.

[9] J. Bohlen, M.R. Nürnberg, J.W. Senn, D. Letzig, S.R. Agnew, The texture and anisotropy of magnesium–zinc–rare earth alloy sheets, Acta Materialia. 55 (2007) 2101–2112. https://doi.org/10.1016/j.actamat.2006.11.013.

[10] M.-G. Lee, R.H. Wagoner, J.K. Lee, K. Chung, H.Y. Kim, Constitutive modeling for anisotropic/asymmetric hardening behavior of magnesium alloy sheets, International Journal of Plasticity. 24 (2008) 545–582. https://doi.org/10.1016/j.ijplas.2007.05.004.

[11] M.H. Yoo, Slip, twinning, and fracture in hexagonal close-packed metals, Metallurgical Transactions A. 12 (1981) 409–418. https://doi.org/10.1007/BF02648537.

[12] H. Fan, J.A. El-Awady, Molecular Dynamics Simulations of Orientation Effects During Tension, Compression, and Bending Deformations of Magnesium Nanocrystals, Journal of Applied Mechanics. 82 (2015). https://doi.org/10.1115/1.4030930.

[13] J. Zhang, Y. Dou, G. Liu, Z. Guo, First-principles study of stacking fault energies in Mg-based binary alloys, Computational Materials Science. 79 (2013) 564–569. https://doi.org/10.1016/j.commatsci.2013.07.012.

[14] S. Sandlöbes, M. Friák, S. Zaefferer, A. Dick, S. Yi, D. Letzig, Z. Pei, L.-F. Zhu, J. Neugebauer, D. Raabe, The relation between ductility and stacking fault energies in Mg and Mg–Y alloys, Acta Materialia. 60 (2012) 3011–3021. https://doi.org/10.1016/j.actamat.2012.02.006.

[15] J.W. Christian, S. Mahajan, Deformation twinning, Progress in Materials Science. 39 (1995) 1–157. https://doi.org/10.1016/0079-6425(94)00007-7.

[16] L. Jiang, M. Gong, J. Wang, Z. Pan, X. Wang, D. Zhang, Y.M. Wang, J. Ciston, A.M. Minor, M. Xu, X. Pan, T.J. Rupert, S. Mahajan, E.J. Lavernia, I.J. Beyerlein, J.M. Schoenung, Visualization and validation of twin nucleation and early-stage growth in magnesium, Nat Commun. 13 (2022) 20. https://doi.org/10.1038/s41467-021-27591-z.
[17] K.D. Molodov, T. Al-Samman, D.A. Molodov, Profuse slip transmission across twin boundaries in magnesium, Acta Materialia. 124 (2017) 397–409. https://doi.org/10.1016/j.actamat.2016.11.022.
[18] M. Gong, G. Liu, J. Wang, L. Capolungo, C.N. Tomé, Atomistic simulations of interaction between basal dislocations and three-dimensional twins in magnesium, Acta Materialia. 155 (2018) 187–198. https://doi.org/10.1016/j.actamat.2018.05.066.
[19] P. Chen, F. Wang, B. Li, Dislocation absorption and transmutation at {10-12} twin boundaries in deformation of magnesium, Acta Materialia. 164 (2019) 440–453. https://doi.org/10.1016/j.actamat.2018.10.064.
[20] J.F. Nie, Y.M. Zhu, J.Z. Liu, X.Y. Fang, Periodic Segregation of Solute Atoms in Fully Coherent Twin Boundaries, Science. 340 (2013) 957–960. https://doi.org/10.1126/science.1229369.
[21] X. Zhao, H. Chen, N. Wilson, Q. Liu, J.-F. Nie, Direct observation and impact of co-segregated atoms in magnesium having multiple alloying elements, Nat Commun. 10 (2019) 3243. https://doi.org/10.1038/s41467-019-10921-7.
[22] A. Kumar, J. Wang, C.N. Tomé, First-principles study of energy and atomic solubility of twinning-associated boundaries in hexagonal metals, Acta Materialia. 85 (2015) 144–154. https://doi.org/10.1016/j.actamat.2014.11.015.
[23] I.J. Beyerlein, L. Capolungo, P.E. Marshall, R.J. McCabe, C.N. Tomé, Statistical analyses of deformation twinning in magnesium, Philosophical Magazine. 90 (2010) 2161–2190. https://doi.org/10.1080/14786431003630835.
[24] I.J. Beyerlein, C.N. Tomé, A probabilistic twin nucleation model for HCP polycrystalline metals, Proceedings of the Royal Society A: Mathematical, Physical and Engineering Sciences. 466 (2010) 2517–2544. https://doi.org/10.1098/rspa.2009.0661.
[25] Y. Hu, V. Turlo, I.J. Beyerlein, S. Mahajan, E.J. Lavernia, J.M. Schoenung, T.J. Rupert, Embracing the Chaos: Alloying Adds Stochasticity to Twin Embryo Growth, Phys. Rev. Lett. 125 (2020) 205503. https://doi.org/10.1103/PhysRevLett.125.205503.
[26] J. Wang, J.P. Hirth, C.N. Tomé, (-1012) Twinning nucleation mechanisms in hexagonal-close-packed crystals, Acta Materialia. 57 (2009) 5521–5530. https://doi.org/10.1016/j.actamat.2009.07.047.
[27] K. Yaddanapudi, B. Leu, M.A. Kumar, X. Wang, J.M. Schoenung, E.J. Lavernia, T.J. Rupert, I.J. Beyerlein, S. Mahajan, Accommodation and formation of {-1012} twins in Mg-Y alloys, Acta Materialia. 204 (2021) 116514. https://doi.org/10.1016/j.actamat.2020.116514.
[28] M. Ghazisaeidi, W.A. Curtin, Analysis of dissociation of <c> and <c+a> dislocations to nucleate (10-12) twins in Mg, Modelling Simul. Mater. Sci. Eng. 21 (2013) 055007. https://doi.org/10.1088/0965-0393/21/5/055007.
[29] R. Aghababaei, S.P. Joshi, Micromechanics of tensile twinning in magnesium gleaned from molecular dynamics simulations, Acta Materialia. 69 (2014) 326–342. https://doi.org/10.1016/j.actamat.2014.01.014.

[30] I.J. Beyerlein, X. Zhang, A. Misra, Growth Twins and Deformation Twins in Metals, Annu. Rev. Mater. Res. 44 (2014) 329–363. https://doi.org/10.1146/annurev-matsci-070813-113304.
[31] P. Chowdhury, H. Sehitoglu, Atomistic Energetics and Critical Twinning Stress Prediction in Face and Body Centered Cubic Metals: Recent Progress, Journal of Engineering Materials and Technology. 140 (2018). https://doi.org/10.1115/1.4038673.
[32] B.-Y. Liu, J. Wang, B. Li, L. Lu, X.-Y. Zhang, Z.-W. Shan, J. Li, C.-L. Jia, J. Sun, E. Ma, Twinning-like lattice reorientation without a crystallographic twinning plane, Nature Communications. 5 (2014). https://doi.org/10.1038/ncomms4297.
[33] Y. He, B. Li, C. Wang, S.X. Mao, Direct observation of dual-step twinning nucleation in hexagonal close-packed crystals, Nat Commun. 11 (2020) 2483. https://doi.org/10.1038/s41467-020-16351-0.
[34] J. Wang, S.K. Yadav, J.P. Hirth, C.N. Tomé, I.J. Beyerlein, Pure-Shuffle Nucleation of Deformation Twins in Hexagonal-Close-Packed Metals, Materials Research Letters. 1 (2013) 126–132. https://doi.org/10.1080/21663831.2013.792019.
[35] H. El Kadiri, C.D. Barrett, J. Wang, C.N. Tomé, Why are {10-12} twins profuse in magnesium?, Acta Materialia. 85 (2015) 354–361. https://doi.org/10.1016/j.actamat.2014.11.033.
[36] L. Capolungo, I.J. Beyerlein, C.N. Tomé, Slip-assisted twin growth in hexagonal close-packed metals, Scripta Materialia. 60 (2009) 32–35. https://doi.org/10.1016/j.scriptamat.2008.08.044.
[37] A. Serra, D.J. Bacon, A new model for {10-12} twin growth in hcp metals, Philosophical Magazine A. 73 (1996) 333–343. https://doi.org/10.1080/01418619608244386.
[38] A. Ostapovets, A. Serra, Review of Non-Classical Features of Deformation Twinning in hcp Metals and Their Description by Disconnection Mechanisms, Metals. 10 (2020) 1134. https://doi.org/10.3390/met10091134.
[39] L. Leclercq, L. Capolungo, D. Rodney, Atomic-Scale Comparison Between {1-101} and {1-102} Twin Growth Mechanisms in Magnesium, (2014) 9.
[40] O. MacKain, M. Cottura, D. Rodney, E. Clouet, Atomic-scale modeling of twinning disconnections in zirconium, PHYSICAL REVIEW B. (2017) 10.
[41] Y. Liu, N. Li, S. Shao, M. Gong, J. Wang, R.J. McCabe, Y. Jiang, C.N. Tomé, Characterizing the boundary lateral to the shear direction of deformation twins in magnesium, Nat Commun. 7 (2016) 11577. https://doi.org/10.1038/ncomms11577.
[42] M. Gong, J.P. Hirth, Y. Liu, Y. Shen, J. Wang, Interface structures and twinning mechanisms of twins in hexagonal metals, Materials Research Letters. 5 (2017) 449–464. https://doi.org/10.1080/21663831.2017.1336496.
[43] Y. Liu, P.Z. Tang, M.Y. Gong, R.J. McCabe, J. Wang, C.N. Tomé, Three-dimensional character of the deformation twin in magnesium, Nat Commun. 10 (2019) 3308. https://doi.org/10.1038/s41467-019-10573-7.
[44] M. Gong, J. Graham, V. Taupin, L. Capolungo, The effects of stress, temperature and facet structure on growth of {10-12} twins in Mg: A molecular dynamics and phase field study, Acta Materialia. 208 (2021) 116603. https://doi.org/10.1016/j.actamat.2020.116603.
[45] M. Lentz, M. Risse, N. Schaefer, W. Reimers, I.J. Beyerlein, Strength and ductility with {10-11} — {10-12} double twinning in a magnesium alloy, Nature Communications. 7 (2016) 11068. https://doi.org/10.1038/ncomms11068.

[46] I.J. Beyerlein, J. Wang, M.R. Barnett, C.N. Tome, Double twinning mechanisms in magnesium alloys via dissociation of lattice dislocations, Proceedings of the Royal Society A: Mathematical, Physical and Engineering Sciences. 468 (2012) 1496–1520. https://doi.org/10.1098/rspa.2011.0731.
[47] Q. Yu, J. Wang, Y. Jiang, R.J. McCabe, N. Li, C.N. Tomé, Twin–twin interactions in magnesium, Acta Materialia. 77 (2014) 28–42. https://doi.org/10.1016/j.actamat.2014.05.030.
[48] R. Xin, C. Guo, J.J. Jonas, G. Chen, Q. Liu, Variant selection of {10-12}-{10-12} double twins during the tensile deformation of an AZ31 Mg alloy, Materials Science and Engineering: A. 700 (2017) 226–233. https://doi.org/10.1016/j.msea.2017.05.105.
[49] S.M. Yin, F. Yang, X.M. Yang, S.D. Wu, S.X. Li, G.Y. Li, The role of twinning–detwinning on fatigue fracture morphology of Mg–3%Al–1%Zn alloy, Materials Science and Engineering: A. 494 (2008) 397–400. https://doi.org/10.1016/j.msea.2008.04.056.
[50] J.I. Goldstein, D.E. Newbury, J.R. Michael, N.W.M. Ritchie, J.H.J. Scott, D.C. Joy, Scanning Electron Microscopy and X-Ray Microanalysis, Springer New York, New York, NY, 2018. https://doi.org/10.1007/978-1-4939-6676-9.
[51] R.O. Duda, P.E. Hart, Use of the Hough transformation to detect lines and curves in pictures, Commun. ACM. 15 (1972) 11–15. https://doi.org/10.1145/361237.361242.
[52] C. Pradalier, P.-A. Juan, R.J. McCabe, L. Capolungo, A Graph Theory-Based Automated Twin Recognition Technique for Electron Backscatter Diffraction Analysis, Integrating Materials and Manufacturing Innovation. 7 (2018) 12–27. https://doi.org/10.1007/s40192-018-0106-y.
[53] D.B. Williams, C.B. Carter, Transmission electron microscopy: a textbook for materials science, 2nd ed, Springer, New York, 2008.
[54] S.G. Wolf, M. Elbaum, Chapter 10 - CryoSTEM tomography in biology, in: T. Müller-Reichert, G. Pigino (Eds.), Methods in Cell Biology, Academic Press, 2019: pp. 197–215. https://doi.org/10.1016/bs.mcb.2019.04.001.
[55] S. Plimpton, Fast Parallel Algorithms for Short-Range Molecular Dynamics, Journal of Computational Physics. 117 (1995) 1–19. https://doi.org/10.1006/jcph.1995.1039.
[56] W. Tao, P. Cao, H.S. Park, Atomistic Simulation of the Rate-Dependent Ductile-to-Brittle Failure Transition in Bicrystalline Metal Nanowires, Nano Lett. 18 (2018) 1296–1304. https://doi.org/10.1021/acs.nanolett.7b04972.
[57] Y. Hu, Probing Solute-Grain Boundary Interactions in Alloys, Ph.D., University of California, Irvine, n.d. https://www.proquest.com/docview/2476153187/abstract/55A0F801EDF548E9PQ/1 (accessed July 9, 2022).
[58] Z. Wu, R. Ahmad, B. Yin, S. Sandlöbes, W.A. Curtin, Mechanistic origin and prediction of enhanced ductility in magnesium alloys, Science. 359 (2018) 447–452. https://doi.org/10.1126/science.aap8716.
[59] A.C. Vaucher, M. Reiher, Minimum Energy Paths and Transition States by Curve Optimization, J. Chem. Theory Comput. 14 (2018) 3091–3099. https://doi.org/10.1021/acs.jctc.8b00169.
[60] G. Henkelman, B.P. Uberuaga, H. Jónsson, A climbing image nudged elastic band method for finding saddle points and minimum energy paths, J. Chem. Phys. 113 (2000) 9901–9904. https://doi.org/10.1063/1.1329672.

[61] T. Zhu, J. Li, A. Samanta, A. Leach, K. Gall, Temperature and Strain-Rate Dependence of Surface Dislocation Nucleation, Phys. Rev. Lett. 100 (2008) 025502. https://doi.org/10.1103/PhysRevLett.100.025502.
[62] A. Ishii, J. Li, S. Ogata, Shuffling-controlled versus strain-controlled deformation twinning: The case for HCP Mg twin nucleation, International Journal of Plasticity. 82 (2016) 32–43. https://doi.org/10.1016/j.ijplas.2016.01.019.
[63] N. Combe, F. Mompiou, M. Legros, Shear-coupled grain-boundary migration dependence on normal strain/stress, Phys. Rev. Materials. 1 (2017) 033605. https://doi.org/10.1103/PhysRevMaterials.1.033605.
[64] N. Combe, F. Mompiou, M. Legros, Heterogeneous disconnection nucleation mechanisms during grain boundary migration, Phys. Rev. Materials. 3 (2019) 060601. https://doi.org/10.1103/PhysRevMaterials.3.060601.
[65] D. Giri, H. ElKadiri, K.R. Limmer, C.D. Barrett, An atomistic gateway into capturing twin nucleation in crystal plasticity, Philosophical Magazine Letters. (2020) 1–11. https://doi.org/10.1080/09500839.2020.1774932.
[66] NSF Award Search: Award#1631873 - DMREF: Engineering Strength and Toughness into Metals, (n.d.). https://www.nsf.gov/awardsearch/showAward?AWD_ID=1631873&HistoricalAwards=false (accessed April 24, 2018).
[67] K. Lu, L. Lu, S. Suresh, Strengthening Materials by Engineering Coherent Internal Boundaries at the Nanoscale, Science. 324 (2009) 349–352. https://doi.org/10.1126/science.1159610.
[68] L. Lu, Ultrahigh Strength and High Electrical Conductivity in Copper, Science. 304 (2004) 422–426. https://doi.org/10.1126/science.1092905.
[69] A. Khosravani, D.T. Fullwood, B.L. Adams, T.M. Rampton, M.P. Miles, R.K. Mishra, Nucleation and propagation of {10-12} twins in AZ31 magnesium alloy, Acta Materialia. 100 (2015) 202–214. https://doi.org/10.1016/j.actamat.2015.08.024.
[70] S.K. Sahoo, L.S. Toth, S. Biswas, An analytical model to predict strain-hardening behaviour and twin volume fraction in a profoundly twinning magnesium alloy, International Journal of Plasticity. 119 (2019) 273–290. https://doi.org/10.1016/j.ijplas.2019.04.007.
[71] X. Wang, L. Jiang, C. Cooper, K. Yu, D. Zhang, T.J. Rupert, S. Mahajan, I.J. Beyerlein, E.J. Lavernia, J.M. Schoenung, Toughening magnesium with gradient twin meshes, Acta Materialia. 195 (2020) 468–481. https://doi.org/10.1016/j.actamat.2020.05.021.
[72] H. Fu, B. Ge, Y. Xin, R. Wu, C. Fernandez, J. Huang, Q. Peng, Achieving High Strength and Ductility in Magnesium Alloys via Densely Hierarchical Double Contraction Nanotwins, Nano Letters. 17 (2017) 6117–6124. https://doi.org/10.1021/acs.nanolett.7b02641.
[73] L. Capolungo, P.E. Marshall, R.J. McCabe, I.J. Beyerlein, C.N. Tomé, Nucleation and growth of twins in Zr: A statistical study, Acta Materialia. 57 (2009) 6047–6056. https://doi.org/10.1016/j.actamat.2009.08.030.
[74] M. Arul Kumar, L. Capolungo, R.J. McCabe, C.N. Tomé, Characterizing the role of adjoining twins at grain boundaries in hexagonal close packed materials, Scientific Reports. 9 (2019). https://doi.org/10.1038/s41598-019-40615-5.
[75] H. El Kadiri, J. Kapil, A.L. Oppedal, L.G. Hector, S.R. Agnew, M. Cherkaoui, S.C. Vogel, The effect of twin–twin interactions on the nucleation and propagation of {10-12} twinning in magnesium, Acta Materialia. 61 (2013) 3549–3563. https://doi.org/10.1016/j.actamat.2013.02.030.

[76] J.J. Jonas, S. Mu, T. Al-Samman, G. Gottstein, L. Jiang, Ė. Martin, The role of strain accommodation during the variant selection of primary twins in magnesium, Acta Materialia. 59 (2011) 2046–2056. https://doi.org/10.1016/j.actamat.2010.12.005.
[77] D. Zhang, L. Jiang, X. Wang, I.J. Beyerlein, A.M. Minor, J.M. Schoenung, S. Mahajan, E.J. Lavernia, Revealing deformation mechanisms in Mg–Y alloy by in situ deformation of nano-pillars with mediated lateral stiffness, Journal of Materials Research. 34 (2019) 1542–1554. https://doi.org/10.1557/jmr.2019.124.
[78] E. Underwood, The Mathematical Foundations of Quantitative Stereology, ASTM International, 1972.
[79] M.R. Barnett, O. Bouaziz, L.S. Toth, A microstructure based analytical model for tensile twinning in a rod textured Mg alloy, International Journal of Plasticity. 72 (2015) 151–167. https://doi.org/10.1016/j.ijplas.2015.05.003.
[80] J. Bohlen, S. Yi, D. Letzig, K.U. Kainer, Effect of rare earth elements on the microstructure and texture development in magnesium–manganese alloys during extrusion, Materials Science and Engineering: A. 527 (2010) 7092–7098. https://doi.org/10.1016/j.msea.2010.07.081.
[81] H. Somekawa, T. Mukai, Hall–Petch relation for deformation twinning in solid solution magnesium alloys, Materials Science and Engineering: A. 561 (2013) 378–385. https://doi.org/10.1016/j.msea.2012.10.040.
[82] J. Tang, H. Fan, D. Wei, W. Jiang, Q. Wang, X. Tian, X. Zhang, Interaction between a {10-12} twin boundary and grain boundaries in magnesium, International Journal of Plasticity. 126 (2020) 102613. https://doi.org/10.1016/j.ijplas.2019.10.001.
[83] H. Yu, C. Li, Y. Xin, A. Chapuis, X. Huang, Q. Liu, The mechanism for the high dependence of the Hall-Petch slope for twinning/slip on texture in Mg alloys, Acta Materialia. 128 (2017) 313–326. https://doi.org/10.1016/j.actamat.2017.02.044.
[84] J. Wang, I.J. Beyerlein, C.N. Tomé, An atomic and probabilistic perspective on twin nucleation in Mg, Scripta Materialia. 63 (2010) 741–746. https://doi.org/10.1016/j.scriptamat.2010.01.047.
[85] F. Wang, S.R. Agnew, Dislocation transmutation by tension twinning in magnesium alloy AZ31, International Journal of Plasticity. 81 (2016) 63–86. https://doi.org/10.1016/j.ijplas.2016.01.012.
[86] F. Wang, Y. Gu, R.J. McCabe, L. Capolungo, J.A. El-Awady, S.R. Agnew, < c + a > dislocations in {10-12} twins in Mg: A kinematic and energetic requirement, Acta Materialia. 195 (2020) 13–24. https://doi.org/10.1016/j.actamat.2020.04.033.
[87] P.G. Partridge, The crystallography and deformation modes of hexagonal close-packed metals, Metallurgical Reviews. 12 (1967) 169–194. https://doi.org/10.1179/mtlr.1967.12.1.169.
[88] S.R. Agnew, Ö. Duygulu, Plastic anisotropy and the role of non-basal slip in magnesium alloy AZ31B, International Journal of Plasticity. 21 (2005) 1161–1193. https://doi.org/10.1016/j.ijplas.2004.05.018.
[89] W.B. Hutchinson, M.R. Barnett, Effective values of critical resolved shear stress for slip in polycrystalline magnesium and other hcp metals, Scripta Materialia. 63 (2010) 737–740. https://doi.org/10.1016/j.scriptamat.2010.05.047.
[90] S. Ando, M. Tsushida, H. Kitahara, Plastic deformation behavior in magnesium alloy single crystals, Materials Science Forum. 706–709 (2012) 1122–1127. https://doi.org/10.4028/www.scientific.net/MSF.706-709.1122.

[91] Z. Wu, W.A. Curtin, The origins of high hardening and low ductility in magnesium, Nature. 526 (2015) 62–67. https://doi.org/10.1038/nature15364.
[92] M.R. Barnett, Twinning and the ductility of magnesium alloys: Part I: “Tension” twins, Materials Science and Engineering: A. 464 (2007) 1–7. https://doi.org/10.1016/j.msea.2006.12.037.
[93] M.R. Barnett, Twinning and the ductility of magnesium alloys: Part II. “Contraction” twins, Materials Science and Engineering: A. 464 (2007) 8–16. https://doi.org/10.1016/j.msea.2007.02.109.
[94] Y. Cui, Y. Li, Z. Wang, Q. Lei, Y. Koizumi, A. Chiba, Regulating twin boundary mobility by annealing in magnesium and its alloys, International Journal of Plasticity. 99 (2017) 1–18. https://doi.org/10.1016/j.ijplas.2017.08.002.
[95] S.R. Agnew, M.H. Yoo, C.N. Tomé, Application of texture simulation to understanding mechanical behavior of Mg and solid solution alloys containing Li or Y, Acta Materialia. 49 (2001) 4277–4289. https://doi.org/10.1016/S1359-6454(01)00297-X.
[96] S. Miura, S. Imagawa, T. Toyoda, K. Ohkubo, T. Mohri, Effect of rare-earth elements Y and Dy on the deformation behavior of Mg alloy single crystals, Materials Transactions. 49 (2008) 952–956. https://doi.org/10.2320/matertrans.MC2007109.
[97] Y. Chino, K. Sassa, M. Mabuchi, Texture and stretch formability of a rolled Mg–Zn alloy containing dilute content of Y, Materials Science and Engineering: A. 513–514 (2009) 394–400. https://doi.org/10.1016/j.msea.2009.01.074.
[98] S. Sandlöbes, M. Friák, J. Neugebauer, D. Raabe, Basal and non-basal dislocation slip in Mg–Y, Materials Science and Engineering: A. 576 (2013) 61–68. https://doi.org/10.1016/j.msea.2013.03.006.
[99] D. Zhang, H. Wen, M.A. Kumar, F. Chen, L. Zhang, I.J. Beyerlein, J.M. Schoenung, S. Mahajan, E.J. Lavernia, Yield symmetry and reduced strength differential in Mg-2.5Y alloy, Acta Materialia. 120 (2016) 75–85. https://doi.org/10.1016/j.actamat.2016.08.037.
[100] Y. Chino, M. Kado, M. Mabuchi, Compressive deformation behavior at room temperature – 773K in Mg–0.2mass%(0.035at.%)Ce alloy, Acta Materialia. 56 (2008) 387–394. https://doi.org/10.1016/j.actamat.2007.09.036.
[101] Y. Chino, M. Kado, M. Mabuchi, Enhancement of tensile ductility and stretch formability of magnesium by addition of 0.2wt%(0.035at%)Ce, Materials Science and Engineering: A. 494 (2008) 343–349. https://doi.org/10.1016/j.msea.2008.04.059.
[102] J.A. Yasi, L.G. Hector, D.R. Trinkle, First-principles data for solid-solution strengthening of magnesium: From geometry and chemistry to properties, Acta Materialia. 58 (2010) 5704–5713. https://doi.org/10.1016/j.actamat.2010.06.045.
[103] A. Tehranchi, B. Yin, W.A. Curtin, Solute strengthening of basal slip in Mg alloys, Acta Materialia. 151 (2018) 56–66. https://doi.org/10.1016/j.actamat.2018.02.056.
[104] M. Ghazisaeidi, L.G. Hector, W.A. Curtin, Solute strengthening of twinning dislocations in Mg alloys, Acta Materialia. 80 (2014) 278–287. https://doi.org/10.1016/j.actamat.2014.07.045.
[105] A.H. Cottrell, B.A. Bilby, Dislocation Theory of Yielding and Strain Ageing of Iron, Proc. Phys. Soc. A. 62 (1949) 49–62. https://doi.org/10.1088/0370-1298/62/1/308.
[106] S.M. Zhu, J.F. Nie, Serrated flow and tensile properties of a Mg–Y–Nd alloy, Scripta Materialia. 50 (2004) 51–55. https://doi.org/10.1016/j.scriptamat.2003.09.039.
[107] H. Aboulfadl, J. Deges, P. Choi, D. Raabe, Dynamic strain aging studied at the atomic scale, Acta Materialia. 86 (2015) 34–42. https://doi.org/10.1016/j.actamat.2014.12.028.

[108] Y. Xin, X. Zhou, H. Chen, J.-F. Nie, H. Zhang, Y. Zhang, Q. Liu, Annealing hardening in detwinning deformation of Mg–3Al–1Zn alloy, Materials Science and Engineering: A. 594 (2014) 287–291. https://doi.org/10.1016/j.msea.2013.11.080.
[109] Y.M. Zhu, S.W. Xu, J.F. Nie, {10-11} Twin boundary structures in a Mg–Gd alloy, Acta Materialia. 143 (2018) 1–12. https://doi.org/10.1016/j.actamat.2017.09.067.
[110] X.F. Chen, L.R. Xiao, Z.G. Ding, W. Liu, Y.T. Zhu, X.L. Wu, Atomic segregation at twin boundaries in a Mg-Ag alloy, Scripta Materialia. 178 (2020) 193–197. https://doi.org/10.1016/j.scriptamat.2019.11.025.
[111] X.Y. Zhang, B. Li, X.L. Wu, Y.T. Zhu, Q. Ma, Q. Liu, P.T. Wang, M.F. Horstemeyer, Twin boundaries showing very large deviations from the twinning plane, Scripta Materialia. 67 (2012) 862–865. https://doi.org/10.1016/j.scriptamat.2012.08.012.
[112] J. Wang, L. Liu, C.N. Tomé, S.X. Mao, S.K. Gong, Twinning and De-twinning via Glide and Climb of Twinning Dislocations along Serrated Coherent Twin Boundaries in Hexagonal-close-packed Metals, Materials Research Letters. 1 (2013) 81–88. https://doi.org/10.1080/21663831.2013.779601.
[113] K. Dang, S. Wang, M. Gong, R.J. McCabe, J. Wang, L. Capolungo, Formation and stability of long basal-prismatic facets in Mg, Acta Materialia. 185 (2020) 119–128. https://doi.org/10.1016/j.actamat.2019.11.070.
[114] A. Ostapovets, R. Gröger, Twinning disconnections and basal–prismatic twin boundary in magnesium, Modelling and Simulation in Materials Science and Engineering. 22 (2014) 025015. https://doi.org/10.1088/0965-0393/22/2/025015.
[115] B. Xu, L. Capolungo, D. Rodney, On the importance of prismatic/basal interfaces in the growth of ($1\bar{0}12$) twins in hexagonal close packed crystals, Scripta Materialia. 68 (2013) 901–904. https://doi.org/10.1016/j.scriptamat.2013.02.023.
[116] K. Hantzsche, J. Bohlen, J. Wendt, K.U. Kainer, S.B. Yi, D. Letzig, Effect of rare earth additions on microstructure and texture development of magnesium alloy sheets, Scripta Materialia. 63 (2010) 725–730. https://doi.org/10.1016/j.scriptamat.2009.12.033.
[117] S. Sandlöbes, S. Zaefferer, I. Schestakow, S. Yi, R. Gonzalez-Martinez, On the role of non-basal deformation mechanisms for the ductility of Mg and Mg–Y alloys, Acta Materialia. 59 (2011) 429–439. https://doi.org/10.1016/j.actamat.2010.08.031.
[118] L. Pauling, Atomic Radii and Interatomic Distances in Metals, J. Am. Chem. Soc. 69 (1947) 542–553. https://doi.org/10.1021/ja01195a024.
[119] X. Wang, Y. Hu, K. Yu, S. Mahajan, I.J. Beyerlein, E.J. Lavernia, T.J. Rupert, J.M. Schoenung, Room Temperature Deformation-induced Solute Segregation and its Impact on Twin Boundary Mobility in a Mg-Y Alloy, Scripta Materialia. 209 (2022) 114375. https://doi.org/10.1016/j.scriptamat.2021.114375.
[120] J. Han, S.L. Thomas, D.J. Srolovitz, Grain-boundary kinetics: A unified approach, Progress in Materials Science. 98 (2018) 386–476. https://doi.org/10.1016/j.pmatsci.2018.05.004.
[121] C.D. Barrett, H. El Kadiri, Impact of deformation faceting on {10-12}, {10-11} and {10-13} embryonic twin nucleation in hexagonal close-packed metals, Acta Materialia. 70 (2014) 137–161. https://doi.org/10.1016/j.actamat.2014.02.018.
[122] A. Ostapovets, R. Gröger, Twinning disconnections and basal–prismatic twin boundary in magnesium, Modelling Simul. Mater. Sci. Eng. 22 (2014) 025015. https://doi.org/10.1088/0965-0393/22/2/025015.

[123] M.A. Kumar, I.J. Beyerlein, Local microstructure and micromechanical stress evolution during deformation twinning in hexagonal polycrystals, Journal of Materials Research. 35 (2020) 217–241. https://doi.org/10.1557/jmr.2020.14.
[124] A. Fernández, A. Jérusalem, I. Gutiérrez-Urrutia, M.T. Pérez-Prado, Three-dimensional investigation of grain boundary–twin interactions in a Mg AZ31 alloy by electron backscatter diffraction and continuum modeling, Acta Materialia. 61 (2013) 7679–7692. https://doi.org/10.1016/j.actamat.2013.09.005.
[125] M.R. Barnett, Z. Keshavarz, A.G. Beer, X. Ma, Non-Schmid behaviour during secondary twinning in a polycrystalline magnesium alloy, Acta Materialia. 56 (2008) 5–15. https://doi.org/10.1016/j.actamat.2007.08.034.
[126] C. Lou, X. Zhang, Y. Ren, Non-Schmid-based {10-12} twinning behavior in polycrystalline magnesium alloy, Materials Characterization. 107 (2015) 249–254. https://doi.org/10.1016/j.matchar.2015.07.022.
[127] S. Xu, L.S. Toth, C. Schuman, J.-S. Lecomte, M.R. Barnett, Dislocation mediated variant selection for secondary twinning in compression of pure titanium, Acta Materialia. 124 (2017) 59–70. https://doi.org/10.1016/j.actamat.2016.10.063.
[128] Q. Qin, J.L. Bassani, Non-schmid yield behavior in single crystals, Journal of the Mechanics and Physics of Solids. 40 (1992) 813–833. https://doi.org/10.1016/0022-5096(92)90005-M.
[129] R.A. Lebensohn, C.N. Tomé, A study of the stress state associated with twin nucleation and propagation in anisotropic materials, Philosophical Magazine A. 67 (1993) 187–206. https://doi.org/10.1080/01418619308207151.
[130] C.D. Barrett, H. El Kadiri, M.A. Tschopp, Breakdown of the Schmid law in homogeneous and heterogeneous nucleation events of slip and twinning in magnesium, Journal of the Mechanics and Physics of Solids. 60 (2012) 2084–2099. https://doi.org/10.1016/j.jmps.2012.06.015.
[131] K. Ito, V. Vitek, Atomistic study of non-Schmid effects in the plastic yielding of bcc metals, Philosophical Magazine A. 81 (2001) 1387–1407. https://doi.org/10.1080/01418610108214447.
[132] Z. Wu, M.F. Francis, W.A. Curtin, Magnesium interatomic potential for simulating plasticity and fracture phenomena, Modelling Simul. Mater. Sci. Eng. 23 (2014) 015004. https://doi.org/10.1088/0965-0393/23/1/015004.
[133] A. Stukowski, Visualization and analysis of atomistic simulation data with OVITO–the Open Visualization Tool, Modelling Simul. Mater. Sci. Eng. 18 (2010) 015012. https://doi.org/10.1088/0965-0393/18/1/015012.
[134] J.W. Hutchinson, R. Hill, Bounds and self-consistent estimates for creep of polycrystalline materials, Proceedings of the Royal Society of London. A. Mathematical and Physical Sciences. 348 (1976) 101–127. https://doi.org/10.1098/rspa.1976.0027.
[135] F. Roters, P. Eisenlohr, L. Hantcherli, D.D. Tjahjanto, T.R. Bieler, D. Raabe, Overview of constitutive laws, kinematics, homogenization and multiscale methods in crystal plasticity finite-element modeling: Theory, experiments, applications, Acta Materialia. 58 (2010) 1152–1211. https://doi.org/10.1016/j.actamat.2009.10.058.
[136] R.A. Lebensohn, C.N. Tomé, A self-consistent anisotropic approach for the simulation of plastic deformation and texture development of polycrystals: Application to zirconium alloys, Acta Metallurgica et Materialia. 41 (1993) 2611–2624. https://doi.org/10.1016/0956-7151(93)90130-K.

[137] P.M. Larsen, S. Schmidt, J. Schiøtz, Robust structural identification via polyhedral template matching, Modelling Simul. Mater. Sci. Eng. 24 (2016) 055007. https://doi.org/10.1088/0965-0393/24/5/055007.
[138] N. Thompson, D.J. Millard, XXXVIII. Twin formation, in cadmium, The London, Edinburgh, and Dublin Philosophical Magazine and Journal of Science. 43 (1952) 422–440. https://doi.org/10.1080/14786440408520175.
[139] H. El Kadiri, C.D. Barrett, M.A. Tschopp, The candidacy of shuffle and shear during compound twinning in hexagonal close-packed structures, Acta Materialia. 61 (2013) 7646–7659. https://doi.org/10.1016/j.actamat.2013.09.002.
[140] F. Sansoz, Atomistic processes controlling flow stress scaling during compression of nanoscale face-centered-cubic crystals, Acta Materialia. 59 (2011) 3364–3372. https://doi.org/10.1016/j.actamat.2011.02.011.
[141] D.Y. Sun, M.I. Mendelev, C.A. Becker, K. Kudin, T. Haxhimali, M. Asta, J.J. Hoyt, A. Karma, D.J. Srolovitz, Crystal-melt interfacial free energies in hcp metals: A molecular dynamics study of Mg, Phys. Rev. B. 73 (2006) 024116. https://doi.org/10.1103/PhysRevB.73.024116.
[142] D. Hull, D.J. Bacon, Introduction to dislocations, 5. ed, Butterworth Heinemann, Elsevier, Amsterdam Heidelberg, 2011.
[143] Y. Tang, J.A. El-Awady, Formation and slip of pyramidal dislocations in hexagonal close-packed magnesium single crystals, Acta Materialia. 71 (2014) 319–332. https://doi.org/10.1016/j.actamat.2014.03.022.
[144] G. Agarwal, A.M. Dongare, Deformation Twinning in Polycrystalline Mg Microstructures at High Strain Rates at the Atomic Scales, Sci Rep. 9 (2019) 3550. https://doi.org/10.1038/s41598-019-39958-w.
[145] A. Stukowski, V.V. Bulatov, A. Arsenlis, Automated identification and indexing of dislocations in crystal interfaces, Modelling Simul. Mater. Sci. Eng. 20 (2012) 085007. https://doi.org/10.1088/0965-0393/20/8/085007.
[146] C. He, Y. Zhang, C.Q. Liu, Y. Yue, H.W. Chen, J.F. Nie, Unexpected partial dislocations within stacking faults in a cold deformed Mg−Bi alloy, Acta Materialia. 188 (2020) 328–343. https://doi.org/10.1016/j.actamat.2020.02.010.
[147] G.R. Schleder, A.C.M. Padilha, C.M. Acosta, M. Costa, A. Fazzio, From DFT to machine learning: recent approaches to materials science–a review, J. Phys. Mater. 2 (2019) 032001. https://doi.org/10.1088/2515-7639/ab084b.
[148] L. Yao, Z. Ou, B. Luo, C. Xu, Q. Chen, Machine Learning to Reveal Nanoparticle Dynamics from Liquid-Phase TEM Videos, ACS Cent. Sci. 6 (2020) 1421–1430. https://doi.org/10.1021/acscentsci.0c00430.
[149] W. Jia, H. Wang, M. Chen, D. Lu, L. Lin, R. Car, W. E, L. Zhang, Pushing the limit of molecular dynamics with *ab initio* accuracy to 100 million atoms with machine learning, in: Proceedings of the International Conference for High Performance Computing, Networking, Storage and Analysis, IEEE Press, Atlanta, Georgia, 2020: pp. 1–14.